Study of Circulating Tumor Cells using Microfluidic Technology: From Isolation to Analysis

by

Tae Hyun Kim

A dissertation submitted in partial fulfillment
of the requirements for the degree of
Doctorate of Philosophy
(Electrical Engineering)
in the University of Michigan
2017

Doctoral Committee:

Professor Yogesh B. Gianchandani, Co-chair
Associate Professor Sunitha Nagrath, Co-Chair
Assistant Professor Somin Eunice Lee
Associate Professor Gary D. Luker

Tae Hyun Kim

tztaebo@umich.edu

ORCID iD: 0000-0003-3856-5325

To God and my parents

ACKNOWLEDGEMENTS

I would like to thank a multitude of people, who made this research possible. First and foremost, my advisor, Dr. Sunitha Nagrath who provided me with opportunities that have enabled me to not only increase the depth of my scientific knowledge, but also ingrained in me the skill-set and attitude necessary for research. Her patience and trust in my capabilities has been a constant source of motivation and excitement in every step of my graduate life. I would also like to thank my committee members Dr. Yogesh Gianchandani, Dr. Gary Luker, and Dr. Somin Lee for their constructive criticism and suggestions for this research and the dissertation.

Over the course of my studies at the University of Michigan, I had pleasure of having great friends and colleagues. I would like to extend my gratitude to the members of the Nagrath lab especially to the CTC project team – Dr. Hyeunjoong Yoon, Yang Wang, Molly Kozminsky, Eric Lin, and Kaylee Smith. I would also like to express my sincere thanks to all my former undergraduate researchers – Courtney Riley, Philip Stella, David Altschul, Thomas Plegue, and Ryan Delaney for their support. I have had the pleasure of forming great friendships with Venkatram Pepakayala, Yutao Qin, Po-Chia Lai, Jihyun Cho, and Inyong Kwon and hope to keep it alive for years to come. I leave with fond memories of the time that I have spent with them.

I would also like to express my heartfelt gratitude to all my collaborators and clinical coordinators – Dr. Max S. Wicha, Dr. Daniel F. Hayes, Dr. Diane M. Simeone, Dr. Nithya Ramnath, Dr. Ebrahim Azizi, Dr. Costanza Paoletti, Dr. Monika Burness, Dr. Douglas Thamm,

Dr. Theodore Welling, Dr. Diane Simeone, Dr. ShanShan Wan for their valuable feedback and guidance who made many of my experiments possible.

The unconditional love and endless sacrifices from my family has been the driving force behind my quest for knowledge. My father has been the guiding light throughout my education and my mother has been the continuous source of inspiration throughout the years. I am grateful to my sister Laura Kim and my brother-in-law Dennis Kim for their support and encouragement. I am thankful for the giggles and smiles of my beautiful niece Audrey Hyuna Kim for the cheerfulness, which keeps me going.

Additionally, I am grateful for the Jeongsong International Student Fellowship and the Rackham Conference Travel grants, which helped me greatly in my research. I would also like to acknowledge the Lurie Nanofabrication Facility (LNF) and the Microscopy and Image Analysis Lab (MIL) at University of Michigan. And most importantly, I am very grateful to all the patients who participated in our study, and kindly provided blood samples for our research.

TABLE OF CONTENTS

LIST OF FIGURES

LIST OF TABLES

ABSTRACT

An intimidating aspect of cancer is its ability to spread out to distant organs causing 90% of cancer-associated deaths. This metastatic progression is driven by circulating tumor cells (CTCs) shed from the primary tumor into bloodstream of carcinoma patients. As a result, CTCs hold great promise as a potential biomarker in areas of cancer diagnosis, monitoring, and evaluation of therapeutic efficacy for personalized medicine, which can serve as surrogate for invasive tissue biopsy. However, theses cells are extremely rare with a frequency of only 1-10 cells surrounded by billions of normal blood cells in 1mL of blood. This thesis delineates the shortcomings of existing CTC isolation methods followed by development and implementation of new microfluidic-based platforms to improve the sensitivity, specificity, and throughput for CTC enrichment.

First, an affinity-based CTC isolation chip is introduced incorporating functional graphene oxide for high-density tumor specific antibody presentation. The two-dimensional surface-capture approach shows an overall CTC capture efficiency of >82.3% for flow rates up to 3mL/hr, while maintaining high viability (>90%) from low shear stress generated during sample processing. The extremely low blood cell contamination rate in the order of 100 cells/mL enables subsequent downstream analysis of CTCs. The clinical validity of the chip is demonstrated in a cohort of 47 metastatic breast cancer patients. Second, a size based CTC isolation chip is presented utilizing the inertial force effects to isolate CTCs by differentially focusing. Channel design parameters including the height, width, and radius of curvature and

flow conditions are investigated to observe their effect on particle/cell focusing and streak migration. Optimal flow regimes to achieve maximum separation of 10/20 μm particles, representing leukocytes and CTCs respectively, in various channel configurations are identified. Based on these results, a cascaded spiral chip is designed for label-free CTC isolation achieving 87.76% recovery rate with 97.91% leukocyte depletion. Finally, a catheter based *in-vivo* CTC isolation system is implemented for large blood volume CTC screening. The system includes a dual lumen catheter to connect the patient blood veins, a peristaltic pump for continuous blood sampling, heparin injector to prevent blood clogging and clotting, and a CTC capture module.

CHAPTER 1

1 Introduction

1.1 Circulating Tumor Cells as 'Liquid Biopsy'

The most common cause of cancer related deaths is from the ability of cancer to spread to various distant organs through metastasis, causing 90% of cancer-related deaths[1]. Metastasis is a multistep process in which tumor cells escape from the primary tumor site, enter the bloodstream, arrest at a secondary site, extravasate, and proliferate to form secondary tumor colonies (Figure 1.1). To migrate through the primary tissue and intravasate into the blood, the cell experiences several changes. An aggressive tumor cell is able to fight impediments to intravasation posed by the microenvironment. Only a small percentage of these tumor cells will ultimately grow into micrometastases, and of those micrometastases few still will proceed into full blown macrometastatic lesions. This process occurs in parallel to the development of the primary tumor, and often before that tumor is initially detected. Less than 0.00004% of initially disseminated cells complete the metastatic process, and yet it is these few cells lead that charge of cancer mortality. To be able to isolate and identify these cells is a clear direction of interest in cancer research.

The detection and quantification of these cells known as, circulating tumor cells (CTCs), found in peripheral blood of carcinoma patients have emerged as potential biomarker that can complement traditional tissue biopsy[2]. CTCs that shed from the primary or metastatic tumor deposits are thought to be enriched for metastatic precursors[3,4]. CTCs as a surrogate diagnostic tissue could constitute a 'liquid biopsy' which are easily accessible with minimal risk from routine blood draw, enabling continuous real-time monitoring patients' disease state and therapeutic responses[5,6]. Previously, blood testing with CTC counts in cancer patients have shown to be an independent prognostic factor for progression-free and overall survival[7] and multiple interventional trials are under study to further address different but complementary aspects of the CTC's clinical utility[8]. In addition, it have been confirmed that CTCs could be detected weeks before the primary tumor becomes overtly invasive in mice[9] and patients with pre-invasive lesions, such as ductal carcinoma *in situ,* in breast cancer[10,11]. Although these early disseminating cells needs to be clinically assessed for its capability of forming manifest metastases, CTC are indeed promising biomaterials to understand the metastatic process and to improve the quality of life of cancer patients[3].

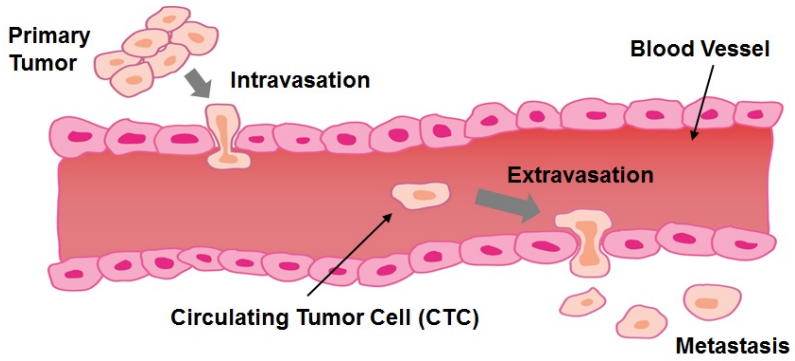

Figure 1.1 Tumor metastasis and circulating tumor cells.

1.2 Challenges of Circulating Tumor Cell Isolation

Although, isolation and analysis of CTCs is becoming important for many clinical applications, including but not limited to serving as a surrogate for invasive biopsy as an emerging biomarker for early cancer diagnosis, progression, and evaluation of drug's therapeutic efficacy for personalized treatment[12-14], due to their extremely rare frequency in patient blood samples (~1-100 CTCs per 10^9 hematologic cells), this remains a challenge.

Figure 1.2 CELLSEARCH® System from Veridex (which is now Janssen Diagnostics).

Currently, the CELLSEARCH® System is the only FDA-cleared system for identification, isolation, and enumeration of circulating tumor cells (CTCs). The machine requires 7.5-mL blood sample and utilizes ferrofluid nanoparticles with antibodies targeting epithelial cell adhesion marker, EpCAM, to magnetically separate CTCs from the bulk of normal blood cells. Using fluorescence imaging technology, the machine then detects and enumerates CTCs of epithelial origin (CD45-, EpCAM+, and cytokeratins 8, 18+, and/or 19+). Over the past years, considerable attention has been made to the CELLSEARCH® System for its high clinical relevance such as in establishing disease-free or overall survival in cancer patients. Clinical trials have shown that in patients with metastatic breast, prostate, or colorectal cancer, CTCs were consistently and markedly more prevalent while they were rarely found in healthy people or in

people with nonmalignant tumors. Other platforms developed for CTC isolation, although not approved by FDA for its use in clinical practice, includes bulk filtration and centrifugation. A different strategy exploits the interaction of specific antibodies and cell surface markers, similar to the CELLSEARCH® System, but present on blood cells for its depletion. However, the limited sensitivity and specificity of current approaches prevent the realization of the full promise of CTCs as a biomarker.

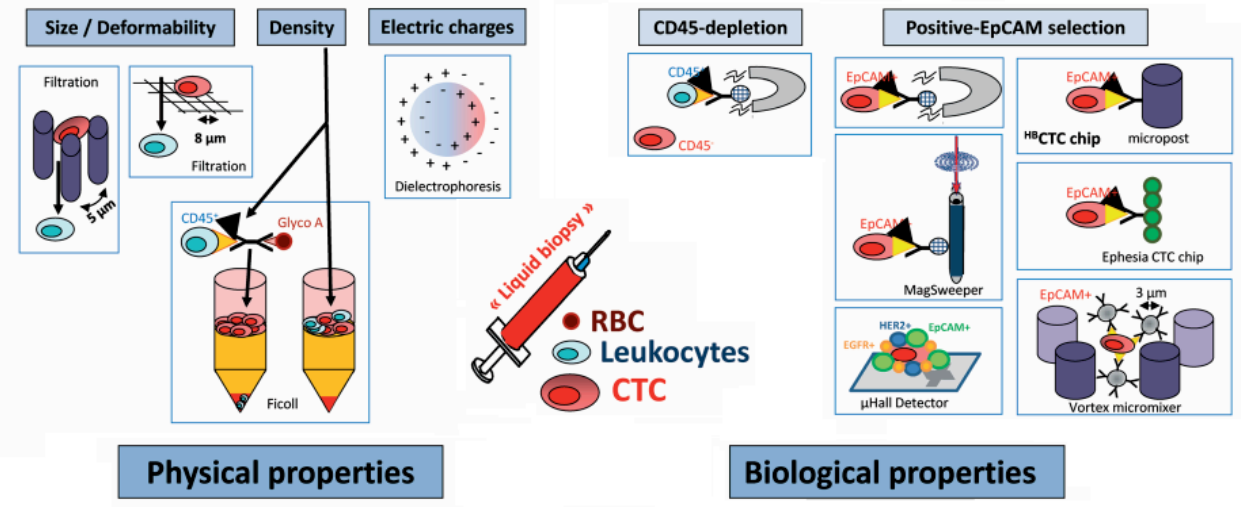

Figure 1.3 CTC isolation techniques using its physical and biological properties. [15]

1.3 Scope of the Thesis

This dissertation discusses the development of microfluidic platforms to isolate CTCs based on their physical and/or biological characteristics. Followed by isolation, CTCs are analyzed in its protein or mRNA level to understand and discover signatures related to metastasis. The remainder of the thesis is outlined below.

In Chapter 2, a sensitive microfluidic device using functionalized graphene oxide (GO) nanosheets to identify and isolate CTCs is discussed. This chapter presents the development and characterization of the next generation immunoaffinity based CTC capture device utilizing the advantage of favorable properties afforded by nanomaterials. GO serves the purpose of packaging the CTC capture antibody with high density on the chip surface allowing sensitive capture with strong bonding strength upon contact. This also reduces the required chip surface area for sufficient CTC capture resulting in a decreased non-specific binding of contaminating blood cells, which is desirable in further downstream analysis. Given the high sensitivity and specificity of this technology, in Chapter 3, CTCs are characterized in its protein and molecular level to begin answering questions regarding the genotypes and phenotypes of these rare cells. To this end, isolation of CTCs from 47 breast cancer patients and their subsequent examination is presented.

Chapter 4 outlines the development of a label-free, cascaded spiral microfluidic platform to isolate CTCs with high purity based on its size difference compared to normal blood cells using inertial focusing effects. This chapter presents methods on defining design parameters and flow conditions for optimal operation for inertial microfluidic devices, particularly in low aspect ratio curvilinear microchannels, which remained nondeterministic due to incomplete understanding of the mechanics and has led to challenges in designing efficient systems. By systematically varying parameters including the channel height, width, and radius of curvature over a wide range of flow velocities, its effect on size dependent differential focusing and migration behaviors of binary (10 μm and 20 μm) particles are analyzed. These results are used to identify optimal flow regimes to achieve maximum separation in various channel configurations tailored to potentially arbitrary flow conditions for size based CTC separation. To

this end, a fully integrated, sheath-less cascaded spiral microfluidic device is described to continuously separate human breast cancer epithelial cell-lines, MCF-7, from leukocytes, with high purity and sustaining high viability upon collection.

In Chapter 5, an indwelling catheter system for *in-vivo* CTC collection is proposed. This allows enrichment of CTCs in larger quantities from directly connecting this portable system to blood veins of cancer patients using dual lumen catheter. Since the event of detecting CTCs are rare, hampering problems of the Poisson statistics, the analysis of a larger blood volume is envisioned to aid clinical analysis and decisions, particularly for early-stage cancer patients. This chapter presents the development of the indwelling catheter system with preliminary results including antibody selection, CTC capture efficiency, sterilization test, and future experimental plans using canine models.

CHAPTER 2

2 Immunoaffinity Based Isolation and Analysis of Circulating Tumor Cells Using Functionalized Graphene Oxide Nanosheets

2.1 Motivation

In early stage cancers, CTCs are present in the blood stream at a low concentration and epithelial cell adhesion molecule (EpCAM) expression, along with other cancer related biomarkers, may be heterogeneous[16,17]. Hence, methods for detecting CTC in early stage cancer patients need to be more sensitive, reliable and specific[12]. Existing microfluidic-based technologies have improved the recovery of CTC from cancer patients[14,18]; however, these technologies rely on micro-structures, trapping arrays[18] or microfilters[19], limiting downstream analysis and further culture. The development of a novel platform that enhances CTC isolation, is sensitive, allows imaging of captured CTCs and enables cell culture would dramatically increase the use of CTCs in diagnostics and prognostics.

Nanomaterials offer excellent opportunities to improve the sensitivity of biomolecule detection due to their high surface area to volume ratio and similar size to biomolecules[20,21]. Recently, silicon-nanopillars[22], quartz-nanowires[23] and TiO_2 nanofibers[24] have been used to trap

CTCs, with enhanced capture efficiency for nanomaterials with higher aspect ratios; however, capture yields were found to be lower than those observed for microfluidic-based CTC chips. Graphene oxide (GO) is a promising nanomaterial in application such as drug delivery[25], biosensing[26] and nanocomposites[27]. Its ease of surface modification using PEG-based chemistry[28], control over the size of its sheets using sonication and filtration[29] and its unique optical properties[30] make GO an attractive material for use in biomolecule detection. This chapter presents and demonstrates an effective approach to isolate CTCs from blood samples of pancreatic, breast and lung cancer patients, by using functionalized graphene oxide nanosheets on a patterned gold surface.

2.2 Material and Methods

2.2.1 Preparation of PEG functionalized GO suspension

10 mg of single layer graphene oxide (SLGO) powder was prepared by a modified Hummer's method (Cheap Tubes Inc.). 10 mL of N,N-dimethylformamide (DMF) and 300 µL of tetrabutylammonium (TBA) hydroxide (40% in water) were added to form a graphene oxide suspension (Figure 2.1 A). Using a tip sonicator, the graphene oxide suspension was ultrasonicated for 30 minutes (Figure 2.1 B). To avoid the temperature increase during sonication, a temperature sensor was monitored and the suspension tube was immersed in an ice bath. The suspension was reserved for 3 days at room temperature. 4 mL of the supernatant was extracted and 15 mg of phospholipids-polyethylene-glyco-amine (PL-PEG-NH2, NOF Co.) was dissolved (Figure 2.1 C), bath sonicated for 1 hour (Figure 2.1 D), and subsequently centrifuged

at 12,000 rpm for 3 minutes (Figure 2.1 E). The supernatant was collected and stored at 4 °C (Figure 2.1 F). The supernatant included PEG functionalized GO.

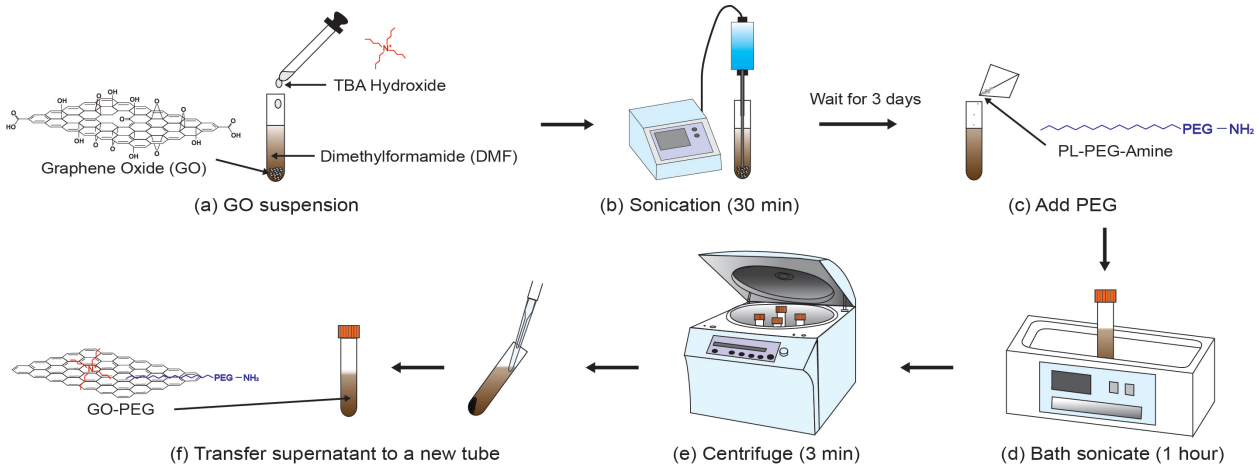

Figure 2.1 Preparation process of PEG functionalized GO suspension.

2.2.2 Microfabrication and Device Assembly

Figure 2.2 shows the fabrication process of the GO chip. 4 inch N-type silicon wafers are cleaned by RCA cleaning. A 3000 Å thermal oxide is grown by wet oxidation process. Cr and Au (100 Å/1000 Å) layers are deposited by e-beam evaporation. Photoresist is coated by automatic spinner (ACS-200, Karl Suss) and patterned by mask aligner (MA-6, Karl Suss). To pattern Au and Cr layers, wafers are put into Au/Cr etch solution. Finally, photoresist is removed by acetone and rinsed by isopropyl alcohol (IPA).

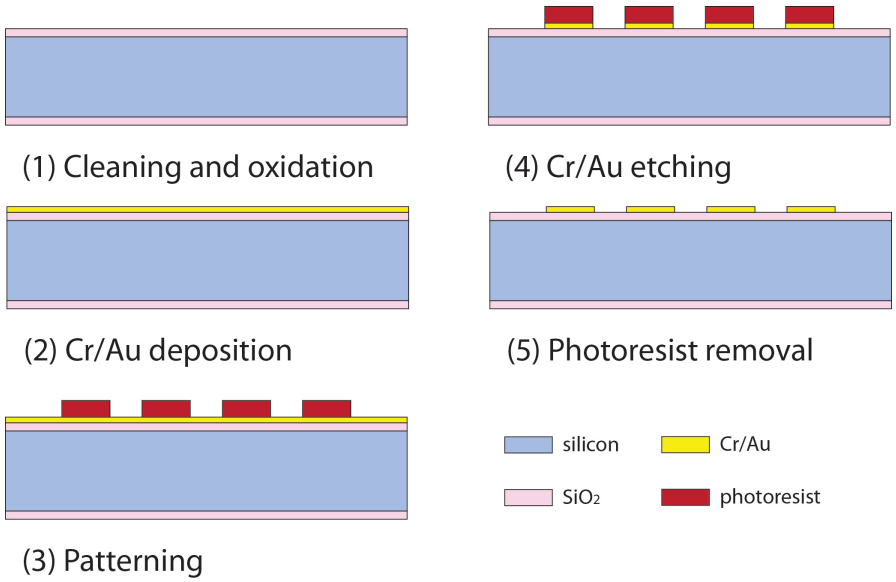

Figure 2.2 Fabrication process of the GO chip.

To self-assemble GO sheets before bonding, a silicon substrate with gold patterns (Figure 2.3 A) was dipped into a functionalized GO suspension for 10 minutes (Figure 2.3 B) and washed with DI water and IPA. A PDMS layer with a chamber was bonded onto the silicon substrate by corona discharge treatment (Figure 2.3 C).

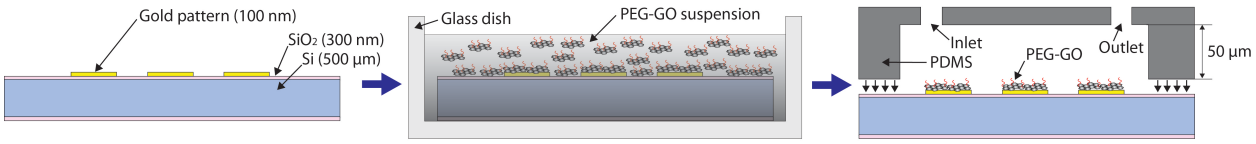

Figure 2.3 Preparation process of GO chip.
(A) Cross-sectional view of the silicon substrate with gold patterns. (B) Dipping the silicon substrate into the functionalized GO suspension. (C) Bonding a PDMS layer to the silicon substrate.

2.2.3 Surface Modification

GMBS solution was flowed through the PEG functionalised GO chip at a 20 μL/min flow rate using a syringe pump (Harvard Apparatus). After 30 minutes of incubation, the device was washed with ethanol at 100 μL/min. 50 μg/mL NeutrAvidin was prepared and flowed through the device at 20 μL/min. After 1 hour incubation, the device was flushed with phosphate buffered saline (PBS) at 100 μL/min to remove the excessive NeutrAvidin. Finally, biotinylated EpCAM antibody at a concentration of 20 μg/mL in PBS with 1% (w/v) BSA was flowed through the device for 10 minutes at 20 μL/min. After 1 hour incubation, PBS was flowed to wash then, 1% or 3% BSA solution in PBS was flowed at 100 μL/min for 5 minutes. After flowing BSA solution, the device was allowed to incubate for 30 minutes.

2.2.4 Cell Culture and Labeling

Tissue culture reagents were purchased from GIBCO Invitrogen Corporation/Life Technologies Life Sciences unless otherwise specified. MCF-7/Hs-578T and PC-3 cells were cultured in DMEM and DMEM/F12 medium containing 10% fetal bovine serum and 1% penicillin-streptomycin solution. When cells reached more than 70-80% confluence, they were harvested and labeled with a green cell tracking dye (Invitrogen, CellTracker Green CMFDA, C7025). Subsequently, these fluorescence tracked cells were used to perform the capture efficiency experiments. For a low number cell spiking (3-20), cells were diluted in serum-free medium starting at an initial concentration of 1×10^5 cells/mL. 1 μL of the concentrated cell suspension was transferred to a low-attachment 96-well plate. The transferred cells were counted under the microscope, then immediately pipetted into a 1 mL of whole blood. After removing the cells

from the 96-well plate, we counted the remaining cells at the same position. By subtracting these cells left behind from the original spot, the total number of cells spiked into blood was estimated.

2.2.5 Cytokeratin and CD45 Staining

After flowing blood samples with low number of non-labeled cells, the captured cells were washed with PBS, fixed with 4% paraformaldehyde (PFA), permeabilized with 0.2% Triton-X and incubated for 30 minutes followed by PBS wash. The device was incubated for 30 minutes with 1 mL of blocking buffer containing 2% normal goat serum and 3% BSA. Anti-cytokeratin 7/8 (BD Biosciences) and anti-CD45 (BD Biosciences) were diluted to 5 μg/mL in 1% BSA. These antibodies were flowed through the GO chip for 20 minutes at 50 μL/min and incubated for 1 hour. After absorption of the primary antibody, the GO chip was washed with PBS. Anti-cytokeratin was probed with Alexa Fluor 488 IgG2a FITC (Invitrogen) and the anti-CD45 was probed with Alexa Fluor 546 IgG1 (Invitrogen). The secondary antibodies were diluted in 1% BSA at a 1:200 ratio, flowed through the GO chip for 20 minutes at 50 μL/min, incubated for 1 hour and followed by washing with PBS. To stain nuclei of the captured cells, DAPI (1:1000 dilution in PBS) was flowed for 20 minutes at 50 μL/min and the device was incubated for 15 minutes and washed with PBS.

2.2.6 Blood Specimen Collection

Blood samples were drawn from patients with tumours and healthy donors after obtaining informed consent under an IRB-approved protocol. All specimens were collected into EDTA tubes and were processed within 3 hours.

2.2.7 Cell Treatment with EdU

To measure cells' ability to proliferate, Click-iT EdU Imaging Kit (Invitrogen, C10340) was used. After capturing cells, the GO chip was washed with PBS, and 10 μM EdU solution was added to the chip. The chip was incubated overnight, washed with PBS and followed by cell fixation with 4% PFA. After 15 minutes of incubation, the chip was washed with 3% BSA twice, followed by cell permeabilization with 0.5% Triton X-100 in PBS and incubated for 20 minutes. The chip was washed with 3% BSA twice and 0.5 mL of Click-iT reaction cocktail was added, followed by 30 minutes incubation and washing once with 3% BSA. For nucleus staining, 1 mL of 1X Hoechst 33342 solution was added and cells in the chip were incubated for 30 minutes and washed with 1 mL of PBS.

2.2.8 RT-qPCR Analysis of Captured CTCs

The RNA from captured CTCs either from spike samples or from patient's blood samples was extracted from the GO chip using Arcturus Picopure RNA isolation kit according to the manufacturer's instruction (ABI, Life Technologies). Then concentrated preparation of total RNA for each sample was used in RT reaction followed by pre-amplification of cDNAs using

the pooled TaqMan Gene Expression assays of target genes and Cell-to-CT Kit according to the manufacturer's instruction (Ambion, Life Technologies) on the Eppendorf mastercycler pro S instrument. Finally, gene expression experiments for each pre-amplified sample were performed using TaqMan Gene Expression Assays for GAPDH and HER2 (Life Technologies) in a multiplex qPCR setting on the ABI 7900HT instrument. Data were presented as mean Ct for mRNA expression level of studied genes.

2.3 Graphene Oxide Device Design

The previously developed 'CTC-Chip' has shown the promise of MEMS (microelectro-mechanical systems) based approach for efficient isolation of CTCs from cancer patients. However the platform was not amenable to traditional imaging or study, as the CTCs were captured around EpCAM coated three-dimensional post structures of 100 µm in height. It was also difficult to release these cells for evaluation (Figure 2.4 A). A second generation of microchip technology to isolate CTCs used EpCAM immobilized herringbone structures to create microvortices to enhance the capture without the aid of microposts (Figure 2.4 B), but this device still had 45 µm tall structures to create passive mixing, occupying 40% of the depth of the device. Moreover, the herringbone structures were functionalized, hence the capture occurred around these structures along with the flat surface, providing some of the same constraints of the original CTC chip. To address these challenges, we have developed a truly 2D planar capture system using a novel nanomaterial graphene oxide (Figure 2.4 C).

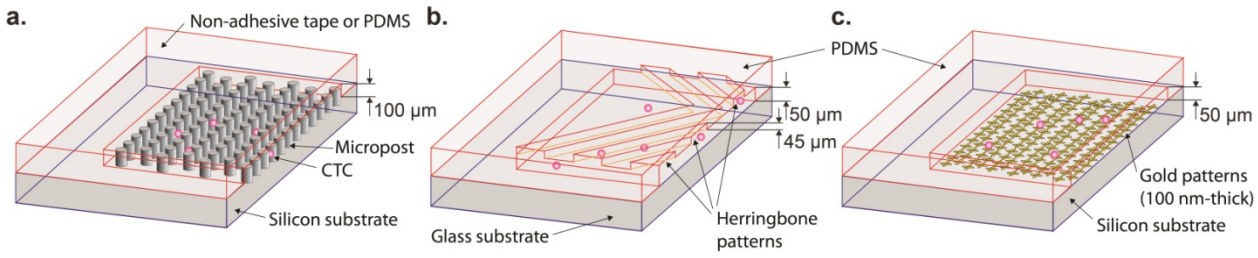

Figure 2.4 Schematic view of microfluidic devices for CTC capture.
(A) Three-dimensional post structures. (B) Herringbone structures. (C) Planar structure with gold patterns.

The GO chip present here takes advantage of this novel nanomaterial for sensitive capture of CTCs using functionalized GO nanosheets on a flat substrate (Figure 2.5 A, B). The silicon substrate has 58,957 flower-shaped gold patterns with a dimension of 100 μm × 100 μm. The distance between each structure in a column is 150 μm and the overall size of the microfluidic device is 24.5 mm × 60 mm × 3 mm. The PDMS (polydimethylsiloxane) layer forms a microfluidic chamber with a 50 μm height and a total volume of 45 μL. Unlike other CTC capture devices with microposts (50~100 μm-thick)[18], the effective functionalized surface created here enables the device to be a simple, flat and chamber-like structure (Figure 2.4).

GO nanosheets are adsorbed onto the patterned gold surface, and then chemically functionalized with EpCAM antibodies. The GO functionalization in this study uses a method described by Li et al. with some modifications (Figure 2.5 C)[31]. GO nanosheets are non-covalently functionalized by phospholipid-polyethylene-glyco-amine (PL-PEG-NH_2) and the hydrophobic lipid chains of PL-PEG-NH_2 are strongly immobilized onto the GO surface. Tetrabutylammonium (TBA) hydroxide is added for intercalation and complete exfoliation of GO. TBA cations and the amino group of PL-PEG-NH_2 interact with the patterned gold surface by electrostatic attraction[32]. N-γ-maleimidobutyryloxy succinimide ester (GMBS) is introduced, which has *N*-hydroxysuccinimide (NHS) esters that react with amine groups of GO-PEG to form amide bonds. The CTCs are then captured using the following NeutrAvidin and biotinylated EpCAM antibody interactions. SEM images reveal that gold patterns were covered with functionalised GO nanosheets (Figure 2.5 D). This shows the high selectivity of GO adsorbed onto the gold patterns rather than silicon dioxide substrate as well as the uniform assembly and saturation density of GO on the gold pattern.

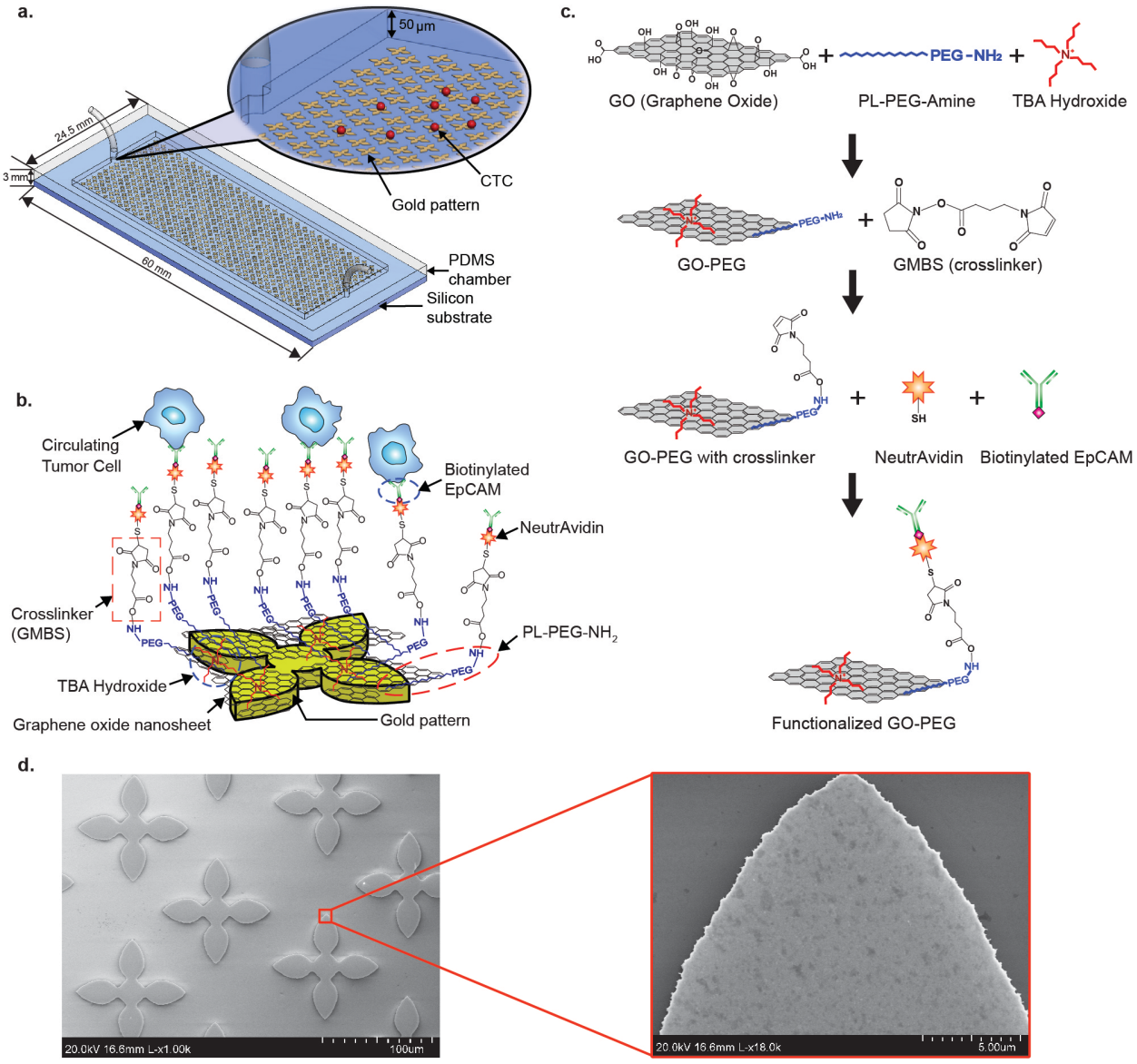

Figure 2.5 GO chip and functionalisation/characterisation of GO.
(A) Schematic diagram of the GO chip. (B) Schematic showing the conjugation chemistry between functionalized GO nanosheets and EpCAM antibodies. GO nanosheets are adsorbed onto the gold pattern. The GMBS cross linker binds to PL-PEG-NH2 onto the GO nanosheets. The NeutrAvidin is connected to the GMBS and biotinylated EpCAM. (C) Preparation procedures of the functionalized GO. (D) SEM image of gold patterns. Inset: magnified SEM image of adsorbed GO nanosheets on gold patterns.

AFM images demonstrated that the GO nanosheets were on the gold patterns (Figure 2.6 A). The thickness of the GO in the assembly was 1-3 nm. SEM images of cell spike capture reveal a captured MCF-7 cell on the functionalized gold pattern (Figure 2.6 B, C).

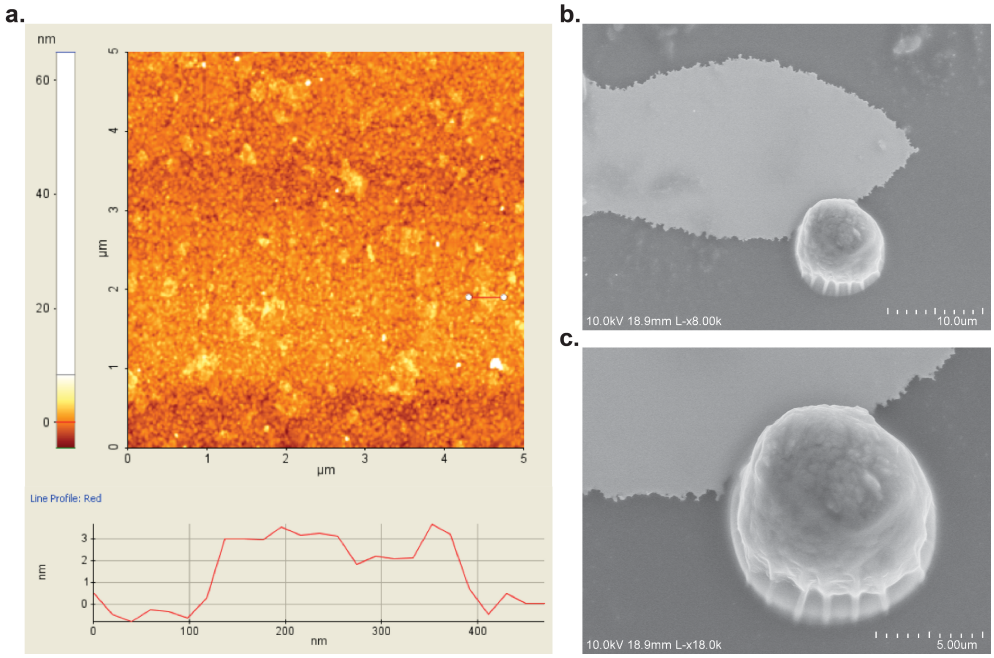

Figure 2.6 AFM image and SEM images.
(A) AFM image of GO nanosheets on the gold surface. (B, C) SEM images of the captured MCF-7 cell.

2.4 Circulating Tumor Cells Capture Efficiency

Human breast cancer cell lines (MCF-7, Hs-578T originally from ATCC) and a human prostate cancer cell line (PC-3, originally from ATCC) were labeled with a fluorescent cell tracker dye, spiked into buffer at varying concentrations, and flowed through the GO chip. The captured cells in the GO chip and the non-captured cells collected in the waste were then counted. Different flow rates were applied to find the optimal flow rate (Figure 2.7 A), and at the 1-3 mL/hr rate range, the capture yield was over 82.3% (n=3). 100-1000 MCF-7 cells per milliliter were then spiked into buffer solution and captured at a flow rate of 1 mL/hr (Figure 2.7 B). There was little difference in capture yield between MCF-7 cells (high EpCAM expression cells) and PC3 cells (relatively low EpCAM expression cells), whereas the capture yield was less than 10% for a non-EpCAM expressing cell line Hs-578T[33] (Figure 2.7 C). Next, the functionalized GO chip and a functionalized flat silicon device without micro posts were compared to examine how GO might increase the capture yield (Figure 2.7 D). The results from spiked cells in buffer solution clearly showed that the GO chip increased capture efficiency. Furthermore, it can be seen that cells were specifically captured on the flower-shaped gold surfaces functionalized with GO. (Figure 2.7 E, F, Figure 2.6 B, C).

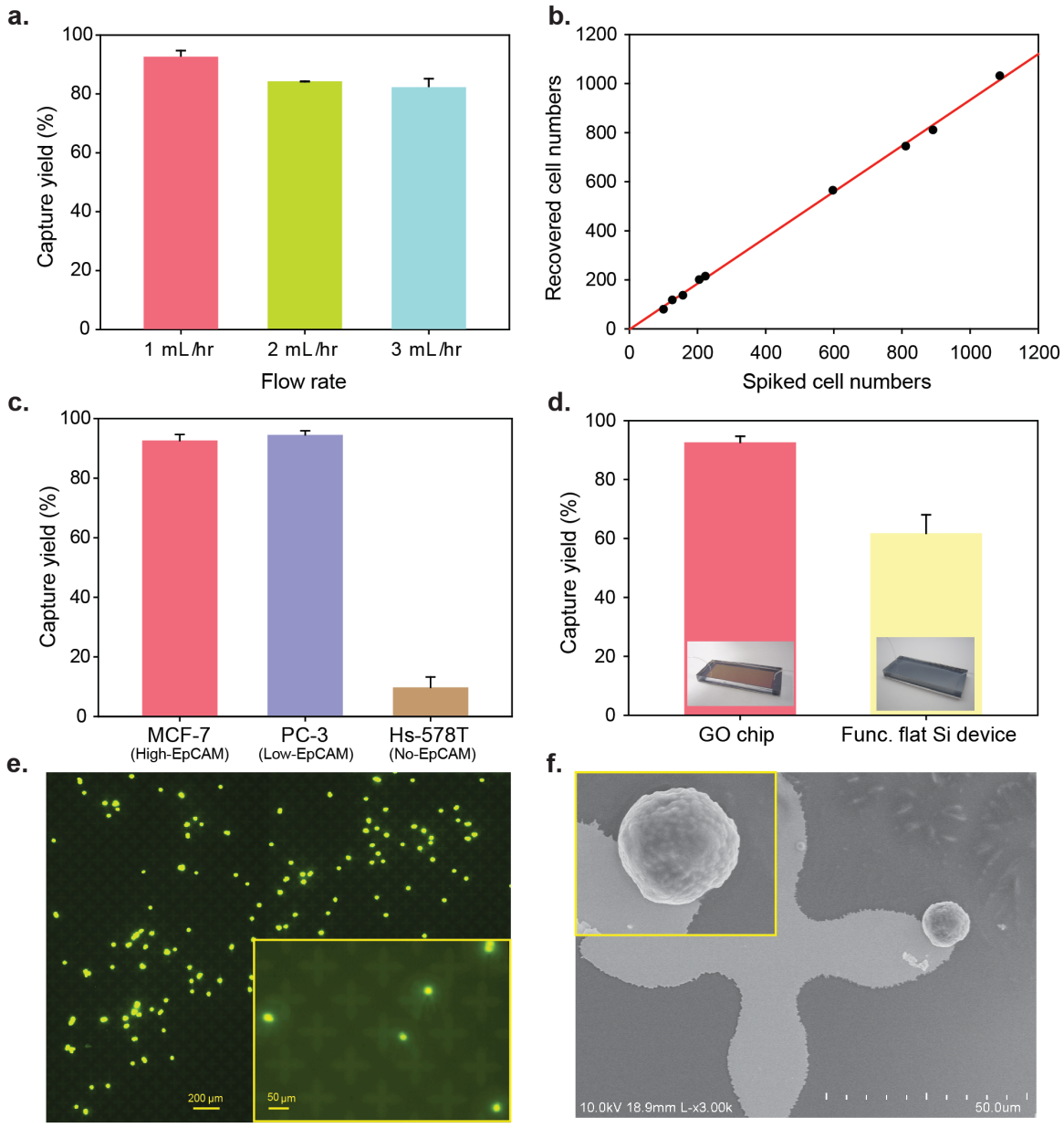

Figure 2.7 Characterization of the GO-chip with cells in buffer solution.
(A) Flow rate dependency on capture efficiency of MCF-7 cells. Error bars represent the standard deviation of three replicates. (B) Capture efficiency of MCF-7 cells at the 1 mL/hr. The red solid line is a fit to the result expected. (C) Comparison of different cell lines; MCF-7 cells (high EpCAM expression), PC-3 cells (low EpCAM expression), and Hs-578T cells (no EpCAM expression). Error bars represent the standard deviation of three replicates. (D) Cell recovery of MCF-7 cells compared to functionalized flat silicon device. Error bars represent the standard deviation of three replicates. Inset: photograph of GO chip (left) and photograph of functionalized flat silicon device (right). (E) Fluorescence image of the captured MCF-7 cells. Inset: magnified (10x) fluorescence image of the captured MCF-7 cells. (F) SEM image of the captured MCF-7 cell on the gold pattern. Inset: magnified SEM image of the captured MCF-7 cell.

To further investigate capture efficiency in human blood samples, varying numbers of MCF-7 cells (3-5 cells, 10-20 cells, 100 cells) were spiked into 1 mL of whole blood and run through the GO chip and the functionalized flat silicon device (Figure 2.8 A, Figure 2.9).

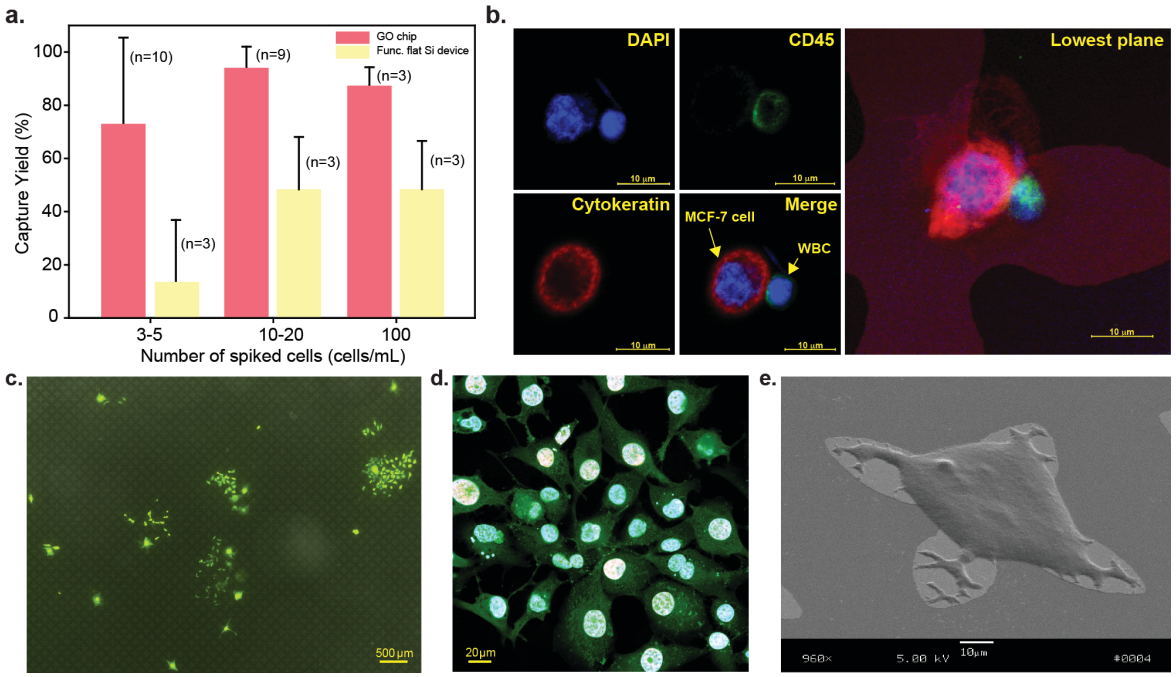

Figure 2.8 Characterization of the GO-chip with MCF-7 cells spiked into whole blood. (A) Cell recovery MCF-7 cells spiked into 1 mL of whole blood at varying spike concentration from 3 to 100 cells/mL. Error bars represent the standard deviation of replicates. (B) Fluorescence microscope image of MCF-7 and white blood cells stained with DAPI (blue), cytokeratin (red), and CD 45 (green). (C) Fluorescence microscope image of 6-day-cultured MCF-7 cells. (D) Fluorescence microscope image depicting proliferation of cells. (E) SEM image of a captured and 6-day-cultured MCF-7 cell.

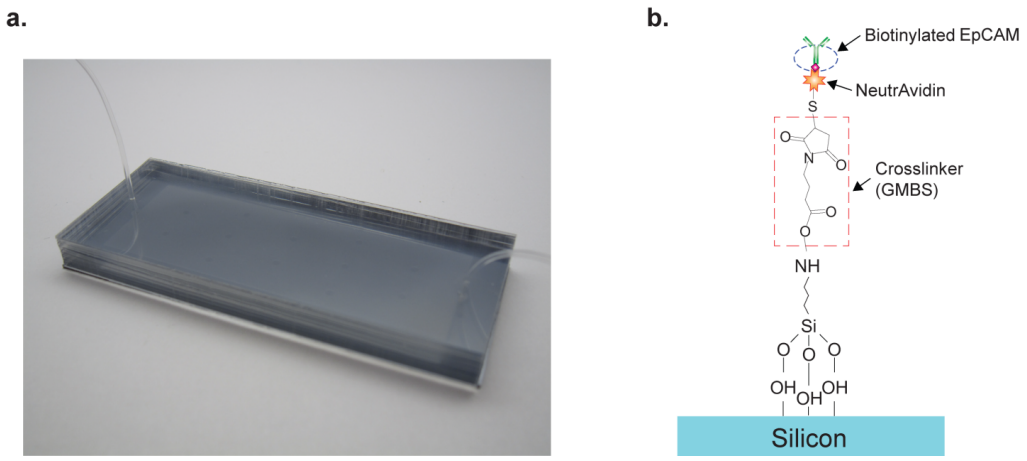

Figure 2.9 Functionalized flat silicon device.
(A) Photograph of the functionalized flat silicon device as a control device. (B) Chemistry structure of the functionalized flat silicon device.

To differentiate captured CTCs and white blood cells, immunostaining was performed by using anti-cytokeratin and anti-CD45, where white blood cells were identified as positive for 4', 6-diamidino-2-phenylindole (DAPI) and cluster of differentiation 45 (CD45, a common leucocyte antigen), while CTCs were identified as positive for DAPI and cytokeratin (CK), but negative for CD45 (Figure 2.8 B). The average recovery rates of 10-20 and 100 spiked cells per 1 mL were 94.2% (n=9) and 87.3% (n=3), respectively (Figure 2.8 A). In the case of 3-5 spiked cells per 1 mL, the average recovery rate was 73% (n=10) and five of the samples had 100% recovery rate (Table 2.1). The higher standard deviation in the 3-5 spiked cell group may be explained by the inherent limitations in capture with cell numbers at low levels. The control functionalized flat silicon device had around 48% capture for both 10-20 and 100 spiked cells and only 13.3% capture for 3-5 spiked cells (Figure 2.8 A). Similar cell spike experiments were performed with the low EpCAM expressing PC-3 cell line and the recoveries were greater than 65% for both 3-5 and 10-20 spiked cells (Figure 2.10 A). Furthermore, we compared the

recovery of MCF-7 and PC-3 cells across the GO chip, the GO chip without gold patterns and the functionalized flat silicon device and found that the GO chip with gold patterns has higher sensitivity for low frequency (3-5 cells) cell recovery (Figure 2.10 B).

Table 2.1 Cell recovery of few number of MCF-7 cells spiked into 1 mL of whole blood.

Number of cells	Device number	Spiked MCF-7 cells	Captured MCF-7 cells	Recovery rate
3~5 cells	D11	5	1	20 %
	D12	5	3	60 %
	D13	4	1	25 %
	D14	3	3	100 %
	D15	5	5	100 %
	D16	4	2	50 %
	D17	4	4	100 %
	D18	5	5	100 %
	D19	4	3	75 %
	D20	5	5	100 %
	Average recovery rate			73 %
10~20 cells	D21	15	15	100 %
	D22	15	15	100 %
	D23	10	8	80 %
	D24	13	11	84.6 %
	D25	18	16	88.9 %
	D26	17	16	94.1 %
	D27	11	11	100 %
	D28	12	12	100 %
	D29	17	17	100 %
	Average recovery rate			94.2 %
100 cells	D31	102	81	79.4 %
	D32	101	91	90.1 %
	D33	107	99	92.5 %
	Average recovery rate			87.3 %

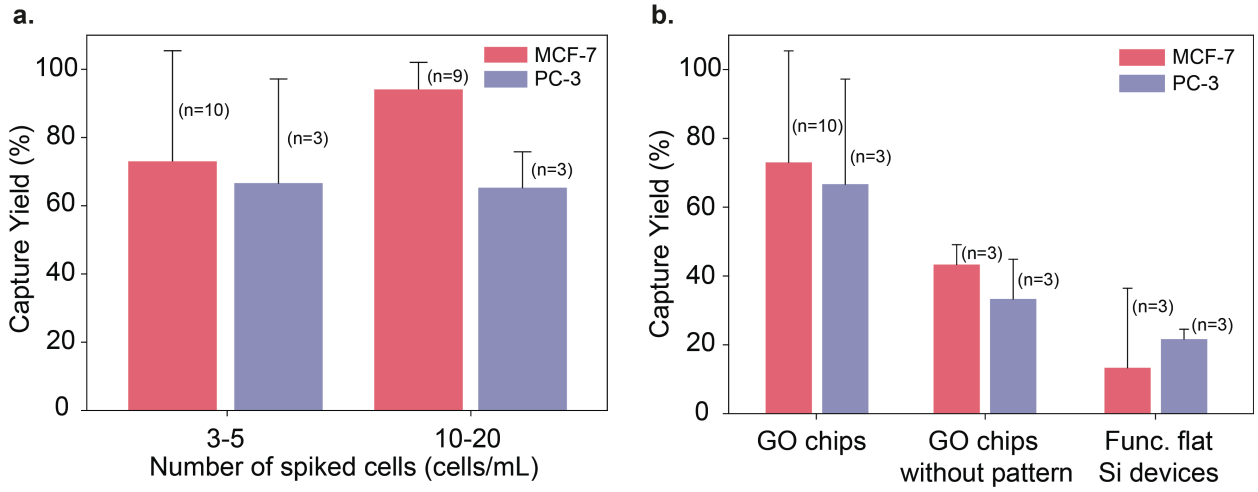

Figure 2.10 Capture efficiency of MCF-7 and PC-3 cells spiked into whole blood.
(A) Comparison of different cell lines (MCF-7 and PC-3) upon 3-5 and 10-20 cells spiked into 1 mL whole blood. Error bars represent the standard deviation of replicates. (B) Comparison of GO-Chips with control devices (GO-Chips without pattern, functionalized flat silicon devices) upon 3-5 cells spiked into 1 mL whole blood. Error bars represent the standard deviation of replicates.

2.5 Circulating Tumor Cell Culture and Expansion

After MCF-7 cells were captured on the GO chip, they were cultured in the device for 6 days (Figure 2.8 C, Figure 2.11 A-F). The captured cells spread on the surface of the substrate and showed evidence of active proliferation, measured by 5-Ethynyl-2'-deoxyuridine (EdU) staining shown in red fluorescence (Alexa Fluor 647)[34] (Figure 2.8 D, Figure 2.11 G-I). Scanning electron microscopy (SEM) images showed the cultured MCF-7 cells spread nicely onto the surface of the GO chip (Figure 2.8 E). The cultured cells were released from the chip by trypsinization and further re-cultured in a 96 well plate (Figure 2.12).

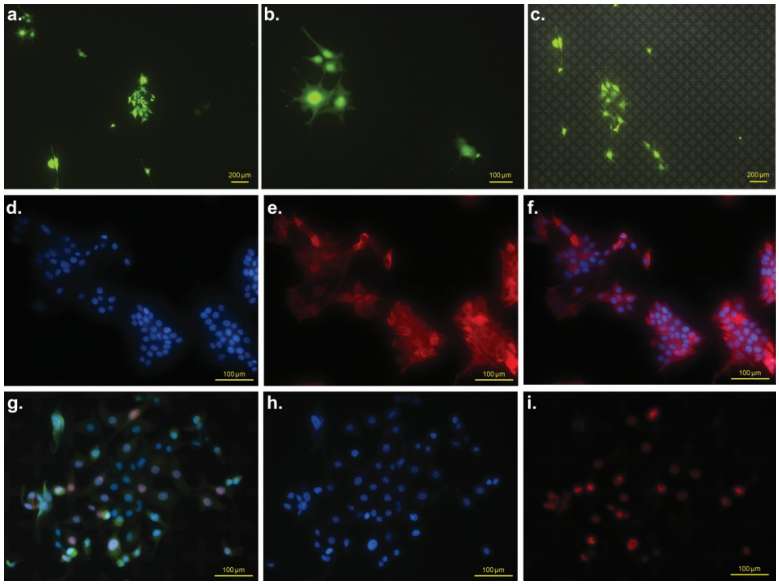

Figure 2.11 Fluorescence microscope images of captured and cultured MCF-7 cells. Fluorescence microscope images of 6-day-cultured MCF-7 cells after capture experiment. (A) 4x magnification. (B) 10x magnification. (C) Merged image with a bright field image (4x). 20x magnification fluorescence microscope images of 6-day-cultured MCF-7 cells with DAPI/cytokeratin staining after capture experiment. (D) DAPI channel (Blue) only for nucleus. (E) Cytokeratin channel (Red) only. (F) Merged channel. Fluorescence microscope images to identify proliferation of MCF-7 cells after capture experiment. Captured cells were stained by Hoechst and Alexa Fluor 647 (Click-iT EdU Imaging Kit). (G) Merged image. (H) Blue fluorescence represents nuclei of MCF-7 cells. (I) Red fluorescence represents proliferating cells.

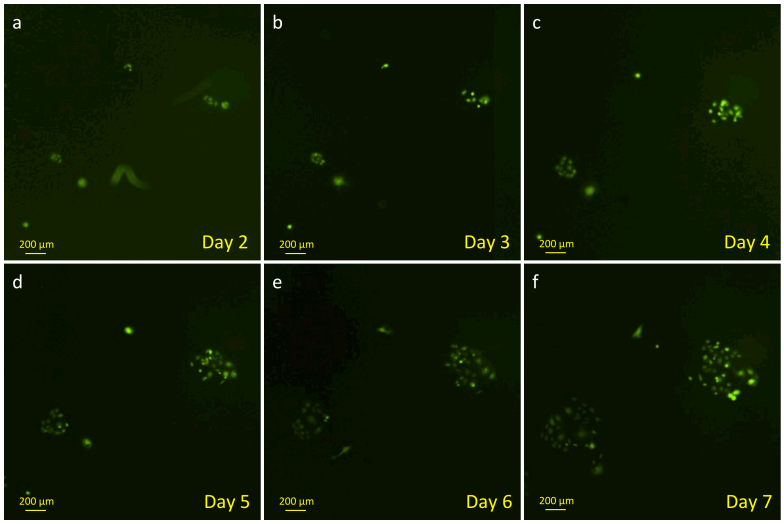

Figure 2.12 Fluorescence microscope images of MCF-7 cells re-cultured on a 96 well plate. These cells were collected and transferred into the well plate after culturing captured cells in the device for 7 days.

2.6 CTC Isolation from Patients with Various Tumor Types

Fresh blood samples obtained from patients with metastatic breast cancer (n=7), early stage lung cancer (n=4) and metastatic pancreatic cancer (n=9) along with 6 age matched healthy individuals (Figure 2.13, Figure 2.14) were processed on GO chips. Clinical data on these patients are available in Table 2.2. CTCs in these samples were identified as DAPI positive nucleated cells staining positive for CK 7, 8 and negative for CD45 (Figure 2.13 A, D, G). Up to 23 CTCs/mL were captured from patient samples (n=39), with all patients analyzed (n=20) having ≥ 2 CTCs/mL (see Table 2.2). We were unable to measure any CTCs in healthy controls (n=6, Figure 2.13 H, Table 2.2). A small number of double positive cells (both CD45+ and CK+) were found in some patient samples. Given, very little has been known about the origin and significance of these cells[35,36], we excluded these from CTC enumeration.

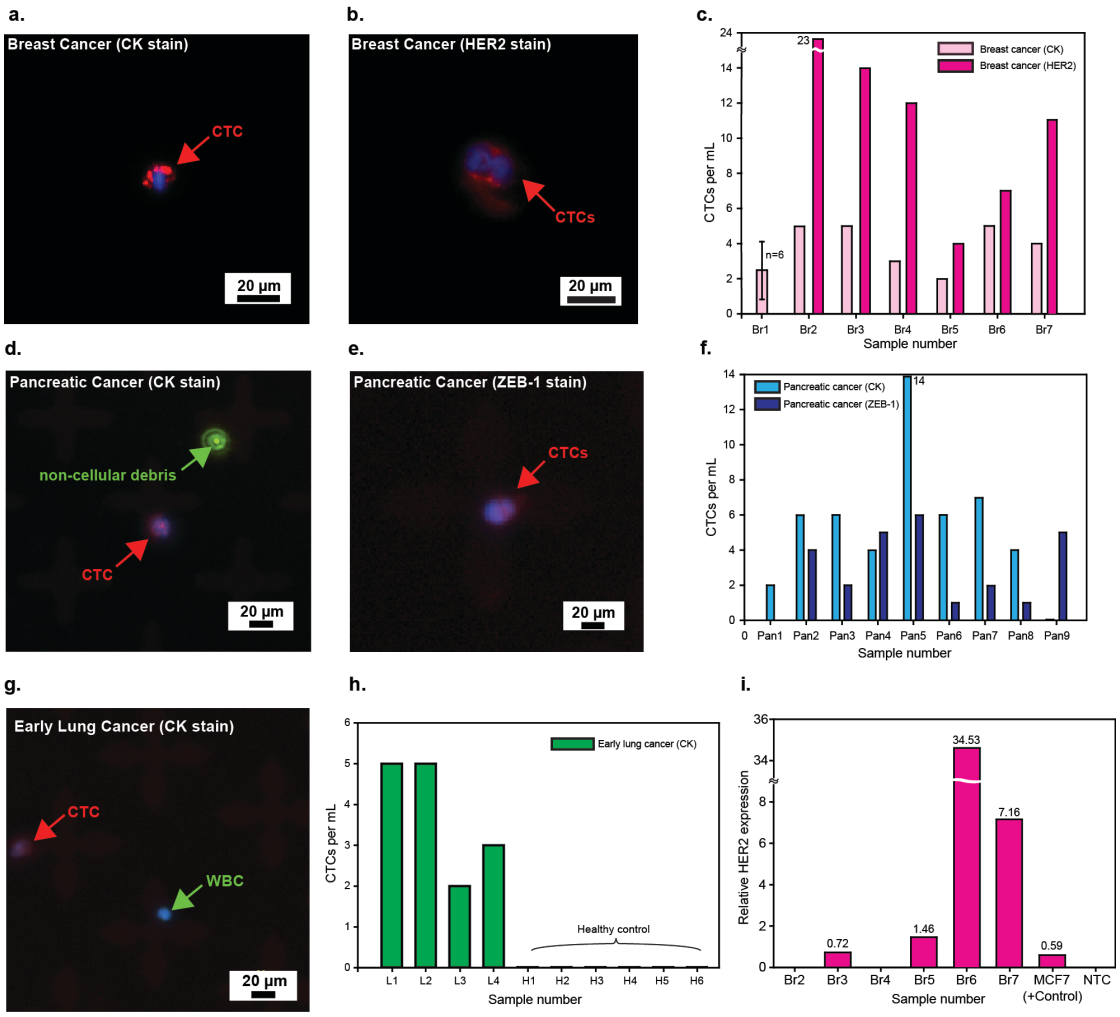

Figure 2.13 Fluorescence microscope images and quantification of CTCs captured from cancer patient samples.

(A) CTC captured from breast cancer patient #6 (Br6). (B) CTCs captured from breast cancer patient #2 (Br2). (C) Quantification of CTCs captured from breast cancer patients. (D) CTC captured from pancreatic cancer patient #2 (Pan2); Fluorescence particle from Alexa Fluor 488 dye shows that CTC has no FITC (green). (E) Two CTCs captured from pancreatic cancer patient #9 (Pan9). (F) Quantification of CTCs captured from pancreatic cancer patients. (G) CTC captured from early lung cancer patient #3 (L3). (H) Quantification of CTCs captured from lung cancer patients and 6 healthy donors. (I) HER2 gene expression (normalized to GAPDH) of captured CTCs by RT-qPCR. Four out of six patients showed expression higher than the gene expression of MCF-7 cells (100 cells)

Table 2.2 Quantification of CTCs from cancer patients and healthy donors.

Sample number	Cancer type	Age	Gender	Cancer stage at the diagnosis	Staining	CTC/mL
Br1	Breast	65	F	IIB	CK	2
					CK	1
					CK	2
					CK	4
					CK	5
					CK	1
Br2	Breast	54	F	IIIA	CK	5
					HER2	23
Br3	Breast	38	F	IIB	CK	5
					HER2	14
Br4	Breast	60	F	IIB	CK	3
					HER2	12
Br5	Breast	81	F	IIB	CK	2
					HER2	4
Br6	Breast	61	F	IIIB	CK	5
					HER2	7
Br7	Breast	80	F	IIB	CK	4
					HER2	11
Pan1	Pancreatic	73	F	IV	CK	2
Pan2	Pancreatic	N/A	N/A	N/A	CK	6
					Zeb-1	4
Pan3	Pancreatic	N/A	N/A	N/A	CK	6
					Zeb-1	2
Pan4	Pancreatic	69	M	N/A	CK	4
					Zeb-1	5
Pan5	Pancreatic	75	M	N/A	CK	14
					Zeb-1	6
Pan6	Pancreatic	74	F	N/A	CK	6
					Zeb-1	1
Pan7	Pancreatic	53	F	N/A	CK	7
					Zeb-1	2
Pan8	Pancreatic	53	F	N/A	CK	4
					Zeb-1	1
Pan9	Pancreatic	50	M	N/A	CK	0
					Zeb-1	5
L1	Lung	75	M	IB	CK	5
L2	Lung	71	M	IA	CK	5
L3	Lung	53	M	IIA	CK	2
L4	Lung	79	F	N/A	CK	3
H1	None	64	F	N/A	CK	0
H2	None	62	F	N/A	CK	0
H3	None	34	M	N/A	CK	0
H4	None	20	F	N/A	CK	0
H5	None	36	F	N/A	CK	0
H6	None	36	F	N/A	CK	0

Two capture experiments were run in parallel for blood samples from breast cancer patients (n=6): one to collect the number of CK+ CTCs and another to stain cells with Human Epidermal Growth Factor Receptor 2 (HER2) along with CD45 to exclude the white blood cells (Figure 2.13 B). Almost all patients had a greater number of EpCAM+, HER2+ and CD45- cells (11 ± 6 CTCs/mL) than EpCAM+, CK+ and CD45- cells (3 ± 1 CTCs/mL) (Figure 2.13 C). Although both HER2-positive and HER2-negative primary breast tumour tissues were analyzed, CTCs from the respective blood samples showed a higher percentage of HER2-positive cells. It has been previously reported that the Veridex CellSearch platform is unable to capture CTCs in 30 to 35% of metastatic breast cancer patients[7,37,38] and detected less than 5 CTCs per 7.5 mL in 70% of the samples with greater than 1 CTC per 7.5 mL. In a study comparing microfluidic approaches to CellSearch, the reported number of CTCs in metastatic breast cancer patients was ≤ 5 per 7.5 mL from 9 analyzed breast cancer patients[39]. For a similar cohort size, we detected 22 CTCs per 7.5 mL in metastatic breast cancer patients.

Table 2.3 Clinical features of breast cancer patients with the HER2 expression in CTCs.

Sample Number	Cancer Stage	HER2 Primary		HER2 Metastatic lesion		CTC		
		IHC	FISH	IHC	FISH	CK+	HER2+	RT-PCR
Br2	IIIA	3+	N/A	3+	N/A	5	23	Negative
Br3	IIB	0	N/A	2+	1.81	5	14	0.72
Br4	IIB	0	N/A	N/A	N/A	3	12	Negative
Br5	N/A	N/A	N/A	0	N/A	2	4	1.46
Br6	IIIB	N/A	4.5	3+	N/A	5	7	34.53
Br7	IIB	1+	N/A	N/A	N/A	4	11	7.16

Nine total pancreatic cancer patients were also analyzed, among which 7 were stage IV metastatic cancer patients, and 2 were patients with stage III disease. All patients had ≥ 2 CTCs/mL, with a mean of 5 ± 4 CTCs/mL. In addition to staining for CK, we analyzed samples in parallel for the epithelial to mesenchymal transition (EMT) marker, Zinc finger E-box-binding homeobox 1 (ZEB-1) along with CD45 to distinguish the white blood cells. Figure 2.13 E presents a cluster of two CTCs expressing ZEB-1 which co-localized with the DAPI-stained nucleus. The average number of ZEB-1+ CTCs isolated was 2 ± 2 CTCs/mL. Among four early stage lung cancer patients analyzed, all of had ≥ 2 CTCs/mL, with a mean of 4 ± 1 CTCs/mL.

To demonstrate downstream molecular assay feasibility, we extracted RNA from CTCs recovered from breast cancer patients. RNA extracted from four out of six breast cancer samples showed HER2 gene expression (Figure 2.13 I), whereas healthy control samples were negative for HER2. The bar chart shows the HER2 gene expression normalized with Glyceraldehyde-3-phosphate dehydrogenase (GAPDH) in pure MCF-7 cells (100 cells), CTCs extracted from breast cancer patients. The negative controls (healthy blood run through the device) did not show the HER2 expression (up to 35 cycles).

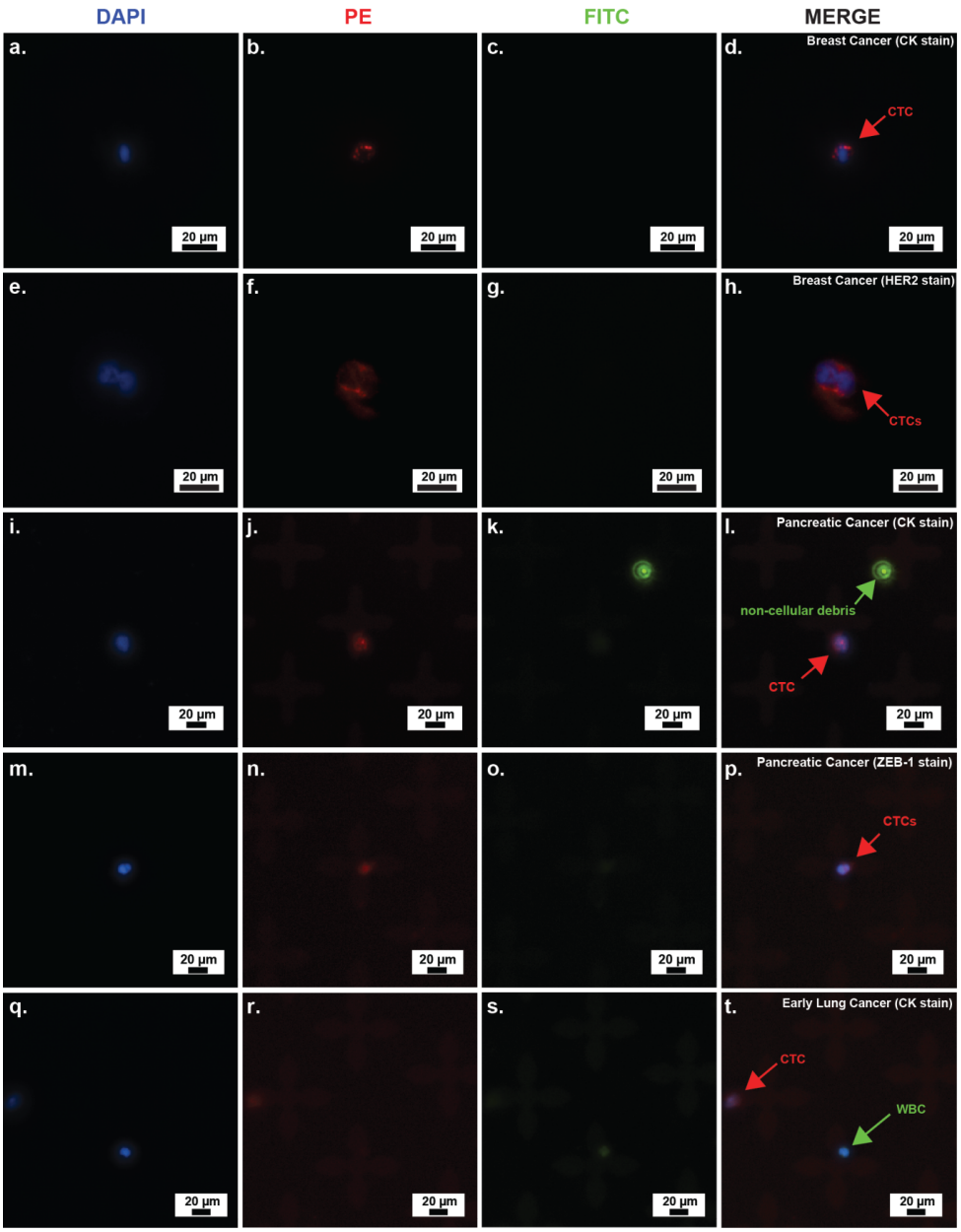

Figure 2.14 Fluorescence microscope images of CTCs captured from breast, pancreatic, and lung cancer patient's blood samples.
(A-D) CTC captured from breast cancer patient #6 (Br6), stained by CK. (E-H) Two CTCs captured from breast cancer patient #2 (Br2), stained by HER2. (I-L) CTC captured from pancreatic cancer patient #2 (Pan2), stained by CK. (M-P) CTCs captured from pancreatic cancer patient #9 (Pan9), stained by ZEB-1. (Q-T) CTC captured from lung cancer patient #3 (L3), stained by CK.

2.7 Purity of CTC Isolation Process

To demonstrate the improved purity afforded by the GO chip, patient samples were processed on the GO chips and blood from healthy control donors was processed on the functionalized flat silicon device. When compared with a control device, GO chips contained fewer non-specifically captured white blood cells (Figure 2.15).

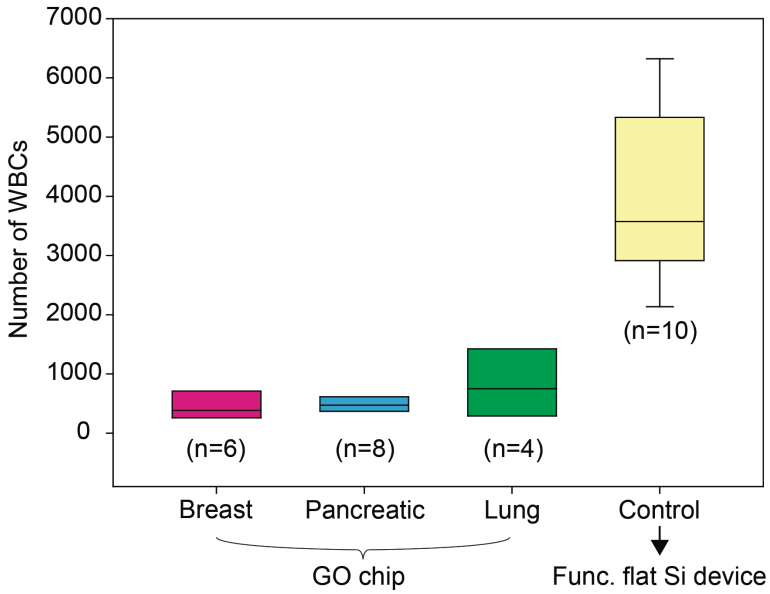

Figure 2.15 Number of captured white blood cells by non-specific binding.

2.8 Conclusion

In summary, we present a novel strategy using GO for sensitive planar CTC capture. Capture yields and detection sensitivities for single digit CTCs spiked into blood were much higher than the reported yields in the literature[22]. With functionalized GO nano-assemblies on the patterned gold surface as an effective tool, we were able to isolate, capture, identify and characterize rare CTCs in the blood of cancer patients for early cancer detection. The GO chip successfully isolates CTCs from early stage lung cancer patients along with advanced metastatic

cancer patients. Recently two approaches were reported that are antibody independent and rely strictly on isolation of CTCs based on cell size[39,40]. However their sensitivity in isolating CTCs in clinical samples was suboptimal compared to the capture efficiencies noted in this study. Furthermore, with filter-based techniques, downstream molecular assays still remain a significant challenge. Although larger clinical studies are warranted to validate our approach, the results demonstrate our ability to isolate CTCs from early stage cancer patients. Of interest, analysis of 6 breast cancer patient samples revealed both HER2-positive and HER2-negative cells primary tumours, but a relatively increased presence of HER2+ cells in the circulation. This warrants further mechanistic investigation, however studies have shown that metastatic lesions vary from the primary tumour in 5-30%[41,42] and that CTCs can be HER2-positive when the primary tumour is HER2-negative[43-45], highlighting the importance of understanding the functional heterogeneity of cancer cells. Although further work is needed to refine the conditions, the extension of the platform to conventional cell culture techniques is a useful advantage. In summary, we demonstrate the efficacy of graphene oxide in a sensitive planar CTC capture device GO chip that provides a platform for functional studies of captured CTCs from blood.

CHAPTER 3

3 Characterizing Circulating Tumor Cells Isolated from Metastatic Breast Cancer Patients Using Graphene Oxide Based Microfluidic Assay

3.1 Motivation

Breast cancer is one of the most frequently occurring malignancies in women. In fact, over 1.3 million new cases are being diagnosed worldwide each year[46]. Advances in early detection and treatments have significantly reduced breast cancer mortality over the past years as the primary tumor often can be controlled by surgical resection. Currently, the survival of patients with breast cancer is closely linked to the incidence of distant metastasis. It has been hypothesized that the development of this metastatic disease is mediated by circulating tumor cells (CTCs) that shed from the primary tumor into blood stream of patients and are emerging as potential biomarker[3,5,6]. The detection and enumeration of CTCs has been shown to be an independent prognostic factor for progression-free survival (PFS) and overall survival (OS) in breast cancer[7,47-49]. In addition, several studies have demonstrated that elevated CTC counts can be an indication of disease progression and be used to monitor and evaluate therapeutic efficacy during treatment[13,50].

Although enumeration of CTC has strong prognostic relevance, little is known about the biology of CTCs and to what degree they may truly represent the actual primary or metastatic tumors. Moreover, prior studies have observed that CTCs can be highly heterogeneous with plastic phenotype[51,52]. Expression of markers including hormone receptors, which are commonly used to guide therapy in breast cancer, has been found to vary remarkably within individual patient's CTCs[43,44,53,54] and their phenotypic transitions between epithelial-like and mesenchymal-like states seem to occur frequently[55-58]. These findings indicate that each CTC may possess diverse functional and malignant properties. Thus, beyond simple enumeration, there is an urgent need to implement detailed molecular and genomic characterization steps for CTC studies, which may also provide valuable information aiding current treatment selections toward personalized medicine.

Despite these great promises as a prospective tumor biomarker, CTC analysis has been challenging due to their rarity. Approximately 1 to 10 CTCs are surrounded by millions of leukocytes and billions of erythrocytes per 1 mL of patient blood. Early approaches to isolate CTCs include macro-scale separation methods such as bulk filtration[59] and centrifugation[60]. A different strategy exploits the interaction between antibodies and cell surface markers present on CTCs, including the FDA-cleared CellSearch® System (Janssen Diagnostics, LLC)[7,61,62]. However, limited sensitivity and specificity of these technologies, which are essential for downstream CTC analysis, have prevented achieving the full clinical utility of CTCs. The incorporation of microfluidic techniques into the field of CTC isolation[18] stimulated the development of a number of technologies, while the next generation of CTC capture devices are taking advantage of favorable properties afforded by nanomaterials. Several studies have achieved increased yield of isolating CTCs using various nanomaterials[63]. However, many

devices have been tested using spiked samples as a substitute for clinical specimens, which could adversely influence the performance of the assay. In order to evaluate applicability and expedite translation of these technologies into clinical settings, thorough validation with a broader pool of patients needs to be investigated.

Previously, we developed a sensitive microfluidic device using functionalized graphene oxide (GO) to isolate CTCs[64]. During whole blood (WB) processing, GO served the purpose of increasing the surface area on which the tumor specific capture antibody was present. In this chapter, we modify the channel geometry to obtain a uniform flow distribution improving the purity from blood cell contamination and develop protocols for multiple downstream analyses to validate the clinical applicability of our assay. Our present investigation includes (i) quantification of CTCs isolated from a large number of metastatic breast cancer (MBC) patients to evaluate capture performance of detecting CTCs from small volumes (1ml) of blood sample; (ii) comparison of human epithelial growth factor receptor 2 (HER2) status in primary and metastatic tumors with HER2 expression on CTCs; (iii) immunofluorescence (IF) analysis using Vimentin and N-cadherin to classify distinct cellular subtypes with epithelial-to-mesenchymal transition (EMT) properties; (iv) transcriptional analysis for CTC characterization using pooled 96 genes selected based on their importance in pathways aberrant in cancer to correlate our findings with clinical and pathological characteristics of MBC.

3.2 Material and Methods

3.2.1 GO Chip Fabrication and Surface Functionalization

The GO chip consists of a gold patterned silicon dioxide substrate bonded to a polydimethylsiloxane (PDMS) top layer to form a microfluidic chamber[64]. In brief, Cr and Au thin films were deposited using evaporation and patterned subsequently using conventional photolithography. Concurrently, PDMS fluidic channels were manufactured using conventional soft lithography. Silicon dioxide substrates with gold patterns were dipped in a GO suspension for 10 minutes and rinsed with DI water and isopropanol. The substrate and a PDMS chamber were bonded via corona discharge. The device was then functionalized via a conjugation chemistry consisting of N-γ-maleimidobutyryl-oxysuccinimide ester (GMBS), NeutrAvidin, and biotinylated anti-epithelial cell adhesion molecule (EpCAM) antibody (Figure 3.1 B) and blocked with 3% bovine serum albumin before use. All steps following the introduction of GMBS were conducted using a syringe pump (Harvard Apparatus).

3.2.2 Metastatic Sample Collection and Processing

Whole blood was drawn from patients diagnosed with MBC and healthy donors after obtaining informed consent under an Institutional Review Board (IRB)-approved protocol at the University of Michigan. All specimens were collected in EDTA vacutainers and processed within 4 hours of blood draw. A detailed summary of all patient data is illustrated in Table S1. Following device functionalization and blocking, 1 mL of WB was processed through individual GO chips at a target flow rate of 1 mL/hr. After a vigorous washing step with PBS at 100 μL/min

for 1 hour, cells were fixed with 4% paraformaldehyde (PFA, Thermo Scientific) and stored at 4°C until staining. Cell fixation step was omitted for chips subjected to RNA isolation.

3.2.3 Multichannel Immunofluorescence Analysis

Captured cells were permeabilized with 0.1% Triton-X and blocked with 3% BSA with 2% goat serum. Immunofluorescence staining was conducted using primary antibodies against a combination of markers including any of the following: cytokeratin 7/8 (CK, BD Biosciences), CD45 (BD Biosciences), HER2 (Santa Cruz Biotechnology), Vimentin (Santa Cruz Biotechnology), N-cadherin (Santa Cruz Biotechnology). Secondary antibodies conjugated with Alexa Fluor 488, 546, or 647 (Invitrogen) were diluted in 1% BSA and used for detection. Cell nuclei were then counterstained with 4',6-diamidino-2-phenylindole (DAPI; Invitrogen). All chips were stored at 4°C until imaging. Cells were observed under 10x magnification using the inverted epifluorescence microscope (Ti Eclipse, Nikon) with an automated motor stage. Images were reviewed manually. Cells positively stained for CK, HER2, or EMT markers (Vimentin, N-cadherin), with DAPI-positive/CD45-negative, were subjected to our analysis.

3.2.4 RT-qPCR Gene Expression Analysis

Total RNA was extracted by lysing the captured cells on-chip using Arcturus Picopure RNA isolation kit (ABI, Life Technologies). After incubating the GO chip at 42 °C for 30 minutes, the lysate was collected and stored at -80 °C until analysis. cDNA was synthesized from the effluent followed by pre-amplification using the corresponding pooled TaqMan gene expression assays (Life technologies) and Cell-to-CT kit (Ambion, Life Technologies) on an

Eppendorf Mastercycler pro S instrument. Finally, the expression patterns of pre-amplified cDNAs for each sample were determined in a quantitative polymerase chain reaction (qPCR) setting using the same TaqMan gene expression assays that were used during the pre-amplification step on the ABI 7900HT or BioMark HD qPCR platform (Fluidigm). A housekeeping-gene, *GAPDH*, was used as internal control and for normalization. Control blood samples from healthy volunteers were processed in the same manner as patients' blood for comparison.

3.2.5 Statistical Analysis

Enumeration of CK-positive CTCs isolated from two replicate sampling of the same patient blood was compared to evaluate sensitivity and reproducibility of the assay. The intra-class correlation coefficient (ICC) was calculated to measure the agreement between two tests. Difference in CTC counts between different primary tumor subtypes and healthy controls were evaluated using Mann-Whitney test. To compare proportion of epithelial or mesenchymal-like CTCs between different primary tumor subtypes, a generalized linear regression model (specifically, logit link) was used. Tukey adjustment was used for multiple comparisons and significance was determined when the adjusted $P < 0.05$. To compare expression levels of target gene signatures between patient and healthy samples, each transcript was normalized to *GAPDH* and reported as $-\Delta C_T$, where $\Delta C_T = C_{T\ gene} - C_{T\ GAPDH}$. Data points were plotted in heat maps with hierarchical clustering. Fold change was defined as $2^{-\Delta\Delta C_T}$, where $-\Delta\Delta C_T$ is the difference in ΔC_T and P-values were calculated using the two-sample t-test to examine statistical significance of individual genes. $P < 0.05$ or $FC > 2$ was considered statistically significant. Cycle threshold (C_T) values above limit of detection (LOD) were treated as off-scale data and in cases where the

amplification was not detected during the qPCR cycle, an arbitrary ΔC_T value was assigned from a pre-specified range for numerical analysis. To determine this range, the maximum ΔC_T value among the observed data was set for the lower bound and the maximum value of LOD – $C_{T\ GAPDH}$ was used for the upper bound. The range based on the above definition potentially covers all possible values that an unobserved data could have leading to a conservative P-value. For each imputed dataset, a final P-value was calculated by averaging the P-values from 100 imputed datasets. All statistical analysis was conducted using R (version 3.2.4) or SAS (version 9.4, SAS Institute, Cary, NC).

3.3 Isolation of CTCs from MBC Patients

A total of 47 female patients with MBC were enrolled in our study (Table 3.1). The medical record was searched for immunohistochemistry (IHC) results of estrogen receptor (ER), progesterone receptor (PR), and HER2 performed on primary and metastatic tumors. Patients were grouped and classified into ER+/PR+ (n = 27), HER2+ (n = 14), and triple negative breast cancer (TNBC, n = 6) to observe correlations with CTC counts as well as proteomic and genomic characteristics. Within our studied population, all patients with available tissues from both primary and metastatic tumor had no discordance in subtypes between primary and metastatic tumors. A schematic overview of the experimental workflow is described in Figure 3.1 A. Peripheral blood from individual patients was drawn and sampled for CTC analysis. One mL of sampled volume was processed through single GO chips in parallel to either analyze the protein or gene expression patterns of CTCs (Figure 3.2).

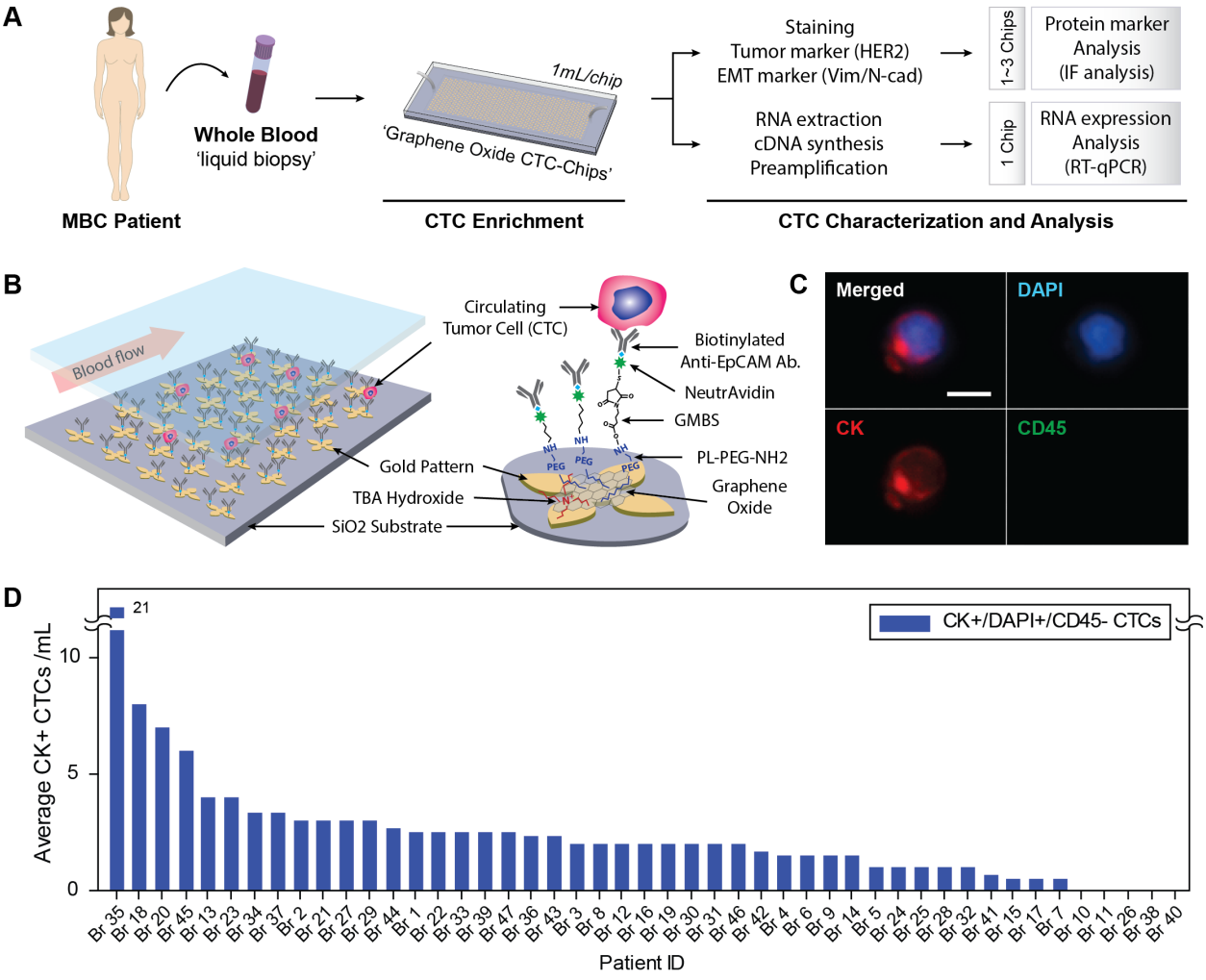

Figure 3.1 CTC isolation and identification.
(A) Study workflow to analyze CTCs isolated from MBC patients using GO assay. WB drawn from MBC patients was sampled and processed through parallel GO chips for enumeration and analysis at both the protein and transcript level. (B) Schematic of antibody conjugation chemistry for device functionalization. (C) Representative image of CK+ CTC showing individual and merged fluorescence channels. (D) Enumeration of isolated CTCs stained for DAPI+/CK+/CD45-. The CTC numbers of samples processed and quantified through multiple GO chips were averaged.

Table 3.1 Cell recovery of few number of MCF-7 cells spiked into 1 mL of whole blood.

Patient ID	Cancer Type	Stage	Tumor Type		Age	Average CK+ CTC/mL
			Primary	Metastatic		
Br 1	Breast Cancer	Metastatic	ER+/HER2-	n/a	53	2.5
Br 2	Breast Cancer	Metastatic	ER-/HER2+	n/a	64	3
Br 3	Breast Cancer	Metastatic	ER+/HER2+	n/a	70	2
Br 4	Breast Cancer	Metastatic	ER+/HER2-	ER+/HER2-	50	1.5
Br 5	Breast Cancer	Metastatic	n/a	ER+/HER2-	n/a	1
Br 6	Breast Cancer	Metastatic	ER+/HER2-	ER+/HER2-	63	1.5
Br 7	Breast Cancer	Metastatic	ER+/HER2+	n/a	39	0.5
Br 8	Breast Cancer	Metastatic	ER+/HER2-	ER+/HER2-	43	2
Br 9	Breast Cancer	Metastatic	ER+/HER2-	ER+/HER2-	n/a	1.5
Br 10	Breast Cancer	Metastatic	ER+/HER2+	ER+	53	0
Br 11	Breast Cancer	Metastatic	ER+/HER2-	n/a	66	0
Br 12	Breast Cancer	Metastatic	ER+/HER2-	ER+/HER2-	53	2
Br 13	Breast Cancer	Metastatic	ER+/HER2-	ER+/HER2-	69	4
Br 14	Breast Cancer	Metastatic	ER-/HER2+	ER-/HER2+	55	1.5
Br 15	Breast Cancer	Metastatic	ER+/HER2+	n/a	40	0.5
Br 16	Breast Cancer	Metastatic	ER+/HER2-	ER+/HER2-	66	2
Br 17	Breast Cancer	Metastatic	ER+/HER2-	ER+/HER2-	74	0.5
Br 18	Breast Cancer	Metastatic	ER+/HER2-	n/a	39	8
Br 19	Breast Cancer	Metastatic	ER+/HER2-	ER+	31	2
Br 20	Breast Cancer	Metastatic	ER+/HER2-	ER+/HER2-	64	7
Br 21	Breast Cancer	Metastatic	ER+/HER2-	ER+/HER2-	67	3
Br 22	Breast Cancer	Metastatic	ER+/HER2-	ER+/HER2-	68	2.5
Br 23	Breast Cancer	Metastatic	ER+/HER2-	ER+/HER2-	45	4
Br 24	Breast Cancer	Metastatic	ER+/HER2-	n/a	64	1
Br 25	Breast Cancer	Metastatic	ER+/HER2-	ER+/HER2-	56	1
Br 26	Breast Cancer	Metastatic	ER-/HER2+	ER-/HER2+	63	0
Br 27	Breast Cancer	Metastatic	ER-/HER2-	ER-/HER2-	55	3
Br 28	Breast Cancer	Metastatic	ER+/HER2+	n/a	58	1
Br 29	Breast Cancer	Metastatic	ER-/HER2-	n/a	54	3
Br 30	Breast Cancer	Metastatic	ER+/HER2-	ER+/HER2-	54	2
Br 31	Breast Cancer	Metastatic	ER-/HER2-	ER-/HER2-	68	2
Br 32	Breast Cancer	Metastatic	ER+/HER2-	ER+	66	1
Br 33	Breast Cancer	Metastatic	ER-/HER2+	ER-/HER2+	55	2.5
Br 34	Breast Cancer	Metastatic	ER+/HER2-	ER+/HER2-	64	3.33
Br 35	Breast Cancer	Metastatic	ER-/HER2-	ER-/HER2-	44	21
Br 36	Breast Cancer	Metastatic	ER+/HER2-	ER+/HER2-	55	2.33
Br 37	Breast Cancer	Metastatic	ER+	ER+/HER2+	50	3.33
Br 38	Breast Cancer	Metastatic	ER-/HER2-	ER-/HER2-	n/a	
Br 39	Breast Cancer	Metastatic	ER+/HER2+	n/a	n/a	2.5
Br 40	Breast Cancer	Metastatic	ER-/HER2+	n/a	50	0
Br 41	Breast Cancer	Metastatic	ER+/HER2-	n/a	67	0.67
Br 42	Breast Cancer	Metastatic	ER+/HER2-	ER+	36	1.67
Br 43	Breast Cancer	Metastatic	ER+/HER2-	ER+	44	2.33
Br 44	Breast Cancer	Metastatic	ER+/HER2-	ER+/HER2-	68	2.67
Br 45	Breast Cancer	Metastatic	ER-/HER2-	n/a	n/a	6
Br 46	Breast Cancer	Metastatic	ER-/HER2+	n/a	n/a	2
Br 47	Breast Cancer	Metastatic	ER+/HER+	n/a	n/a	2.5

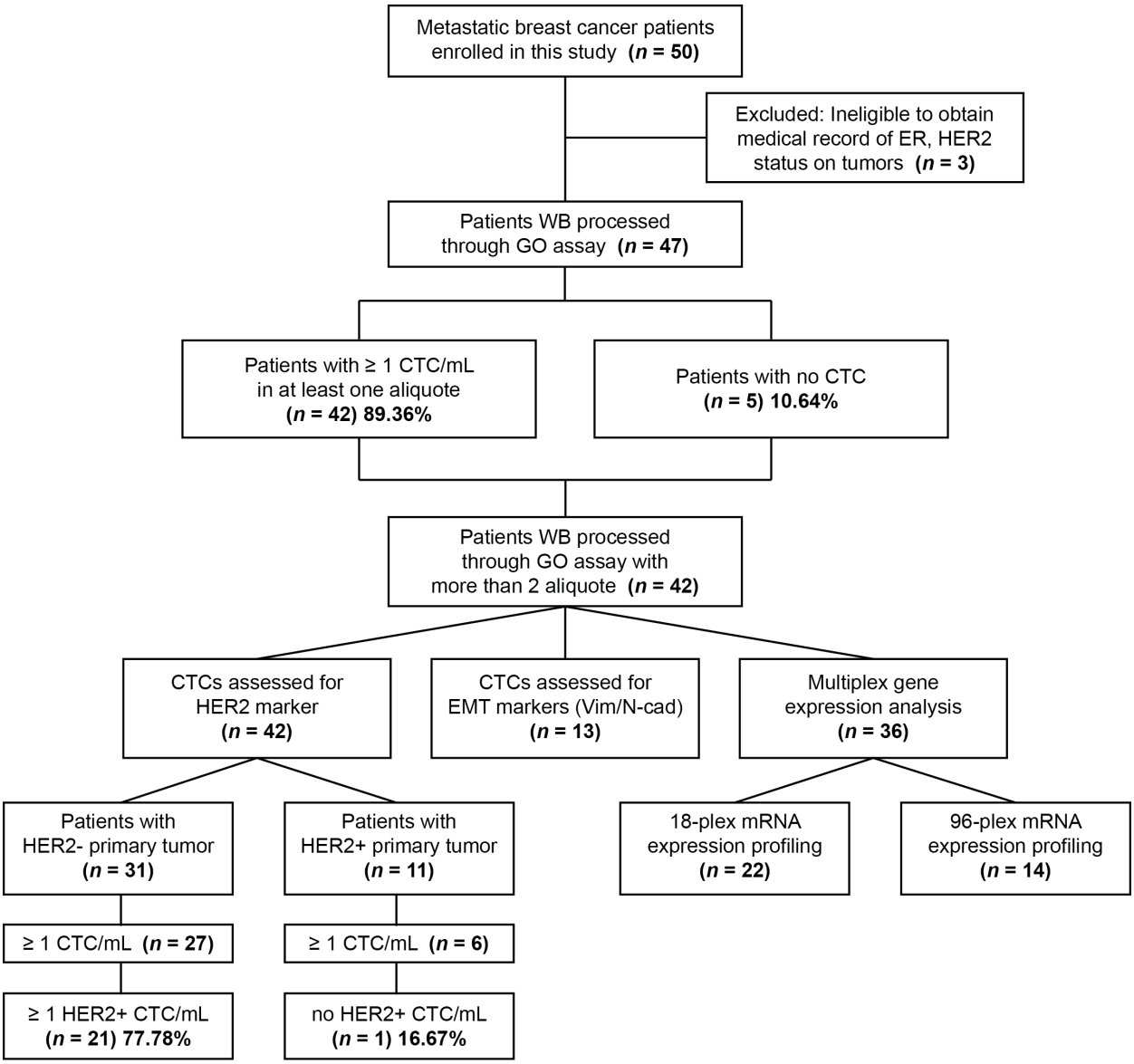

Figure 3.2 REMARK diagram for patient enrollment and distribution.

CTCs have been classically defined as DAPI positive nucleated cells that are stained positive for CK and negative for CD45 (Figure 3.1 C). Based on these criteria, CTC counts were compared for individual cancer patients after processing 1 mL of blood through two separated chips to first evaluate the sensitivity and repeatability of the GO assay. Excluding the one sample with extremely high number of CTCs (Br 35), the average difference of captured CTCs between experiments was less than 1 cell. Overall, a high concordance was observed between the two tests (ICC=0.80 with 95% CI: 0.64,0.89), demonstrating the reproducibility of measurements. In total, 42 out of 47 patients (89.36%) were scored positive for ≥ 1 CTC/mL across the entire MBC patient cohort analyzed showing high sensitivity of CTC isolation (Figure 3.1 D). The number of contaminating white blood cells was consistently less than 500 cells/mL due to the modified channel geometry (Figure 3.3), which minimizes dead volumes, thereby improving the washing process. The range of detected CTCs varied from 0-27 CTCs/mL with an average number of 2.54 CTCs/mL. No CTCs were found in any of the healthy individuals (n = 9). The average number of CTCs found in ER/PR+, HER2+, and TNBC was 2.33, 1.52, and 5.83 cells/mL, respectively (Table 3.2). However, no clear association between the CTC positivity rates or absolute CTC counts among age or immunohistochemical tumor subtypes was observed. Although most cells were detected in single CTCs, clusters comprising two or more CTCs (range, 2-6 CTCs) were also identified in 10 out of 47 (21.28%) cases across all tumor subtypes.

Table 3.2 MBC patient characteristics.

Characteristics	No. Patients (%)	No. Patients w/ CK+ CTC (%)	Average CTCs/mL
Total Patients	47 (100)	42 (89.36)	2.54
Age (31-74)			
< 50	9 (19.15)	9 (100)	4.67
≥ 50	31 (65.96)	27 (87.10)	1.99
Unknown	7 (14.89)	6 (85.71)	2.21
ER status			
Positive	35 (74.47)	33 (94.29)	2.33
Negative	12 (25.53)	9 (75.00)	2.82
HER2 status			
Positive	13 (27.66)	10 (76.92)	1.52
Negative	34 (72.34)	32 (94.12)	2.97
Tumor subtype			
ER+/PR+	27 (57.45)	26 (96.30)	2.33
HER2+	14 (29.79)	11 (78.57)	1.52
TNBC	6 (12.77)	5 (83.33)	5.83

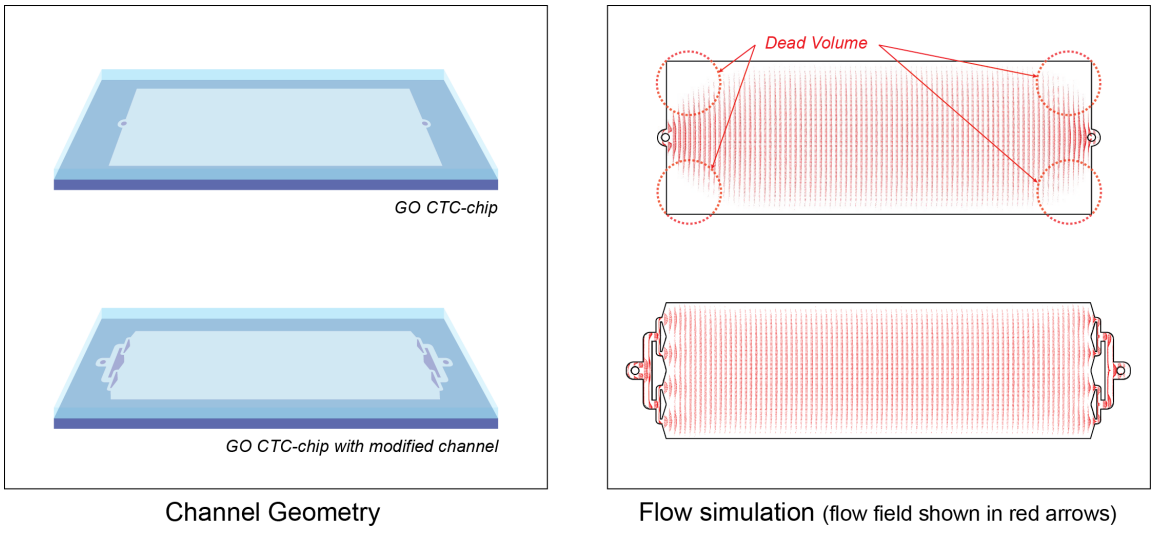

Figure 3.3 Comparison between two fluidic channels used in the GO CTC-chip.
The modified channel geometry minimizes dead volumes within the fluidic channel allowing uniform flow distribution and improved washing performance, which results in an enhanced purity upon CTC isolation. Fluid simulation performed using COMSOL Multiphysics 4.2 to depict overall flow field in the two channel geometries.

3.4 HER2 Expression in CTCs from Metastatic Breast Cancer

HER2 growth factor receptor has been known to play important role in breast cancer development and progression[65] and has become one of most effective therapeutic targets[66]. To examine the distribution of HER2 expressing CTCs and its correlation with HER2 status of the primary tumor, a subset of GO chips was subsequently counterstained with anti-HER2 antibody (Figure 3.4 A). Among 33 samples with detectable CTCs, 26 (78.79%) patients showed positivity in CTC HER2 expression (Figure 3.4 C) with a mean count of 2.13 cells/mL, while more than two HER2+ CTCs were identified in 19 (57.58%) patients regardless of the primary tumor type. 21 out of 27 (77.78%) patients with HER2-negative primary tumor showed at least one CTCs expressing HER2. Discordant HER2 expression was also observed in patients with HER2-positive primary tumor where 1 out of 6 (16.67%) patients had no CTCs with HER2 expression. The overall discrepancy of HER2 status in primary tumor and expression on the corresponding CTCs was 66.67% (22/33).

Interestingly, taking into account all cells presenting HER2 with CD45-/DAPI+ regardless of CK expression in our enumeration, a high number of patients had HER2+ cells (30/34, 88.24%). The average number of CD45- cells assessed by HER2 positivity was also higher (4.45 cells/mL) than CK+ CTCs (3.03 cells/mL). So far, due to the classical definition of CTCs, CK- but HER2+ cells might have been overlooked in clinical assessment. Our finding suggests the need to further investigate these cellular subtypes and evaluate their clinical relevance in screening patients for new therapeutic approaches targeting HER2 in MBC.

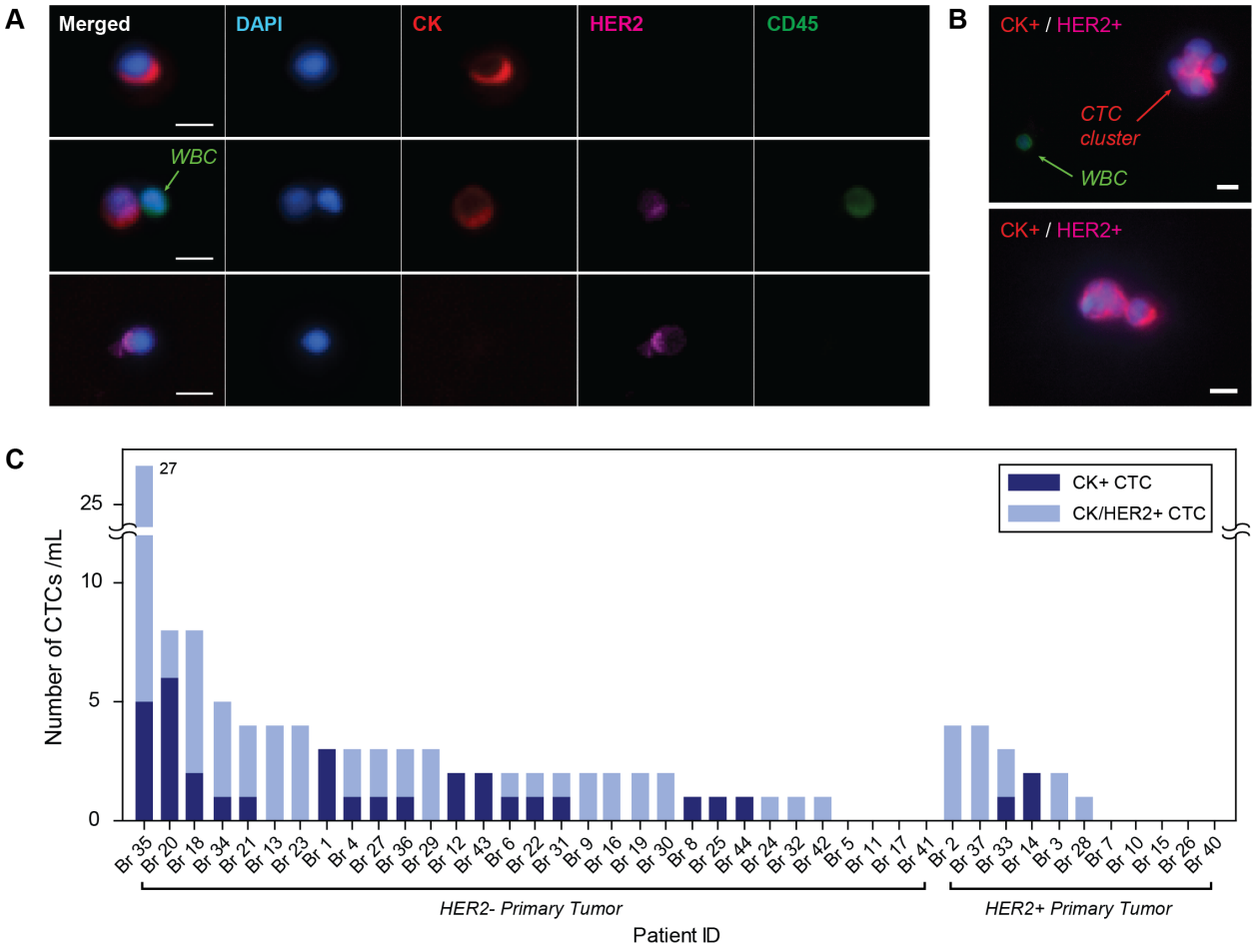

Figure 3.4 Phenotypic characterization of CTCs in HER2 expression.
(A) Characteristic image of CTCs showing differential expression of CK and HER2. (B) Composite image of fluorescently stained CTC clusters. CK, CD45, and the cell nucleus are shown in red, green, and blue while HER2 is shown in pink. (C) Distribution of CK+ and CK+/HER2+ CTCs in MBC patients. All scale bar measures 10 µm.

3.5 EMT Signatures in Metastatic Breast Cancer CTCs

Increasing evidence revealed that epithelial markers including keratins can be downregulated during metastatic spread due to EMT in breast cancer[57,67,68]. This raises questions regarding the common characterization of CTCs as those cells identified by CK positivity, which may be responsible for the high frequency of HER+/CK- cells observed in HER2 staining. To evaluate EMT features present in CTCs isolated from MBC patients, two separate GO chips were additionally stained with antibodies against EMT markers, Vimentin or N-cadherin. Cells presenting at least one epithelial (CK) or mesenchymal (Vimentin/N-cadherin) marker were quantified as candidate CTCs in our analysis. Here, in particular, DAPI+/CD45- was essential for enumeration to confirm that cells characterized as potential CTCs were of non-hematopoietic origin. Out of the 13 samples examined, 9 (69.2%) scored positive for at least one EMT marker in the isolated CTC population (Figure 3.5 E, F). When we further stratified CTCs into epithelial (CK+/EMT-), intermediate/hybrid (CK+/EMT+), and mesenchymal-like (CK-/EMT+) phenotypes (Figure 3.5 A, B), the CTCs isolated from ER+ primary tumor patients were predominantly epithelial compared to HER2+ (P=0.0436) and TNBC (P=0.0003), whereas those from HER2+ and TNBC displayed increased level of EMT marker expressions (Figure 3.5 G). Notably, the occurrence of hybrid state CTCs comprised of both epithelial and mesenchymal phenotype was most frequently identified in TNBC patients, conferring both invasive and proliferative properties that potentially reflect the aggressiveness of the disease. This finding aligns with previous studies showing that downregulation of keratin expression in EpCAM positive CTCs is more likely associated with triple negative histology and shorter OS [69]. All CTC clusters identified expressed CK; some clustered cells expressed Vimentin, while no N-cadherin expression was observed (Figure 3.5 C, D).

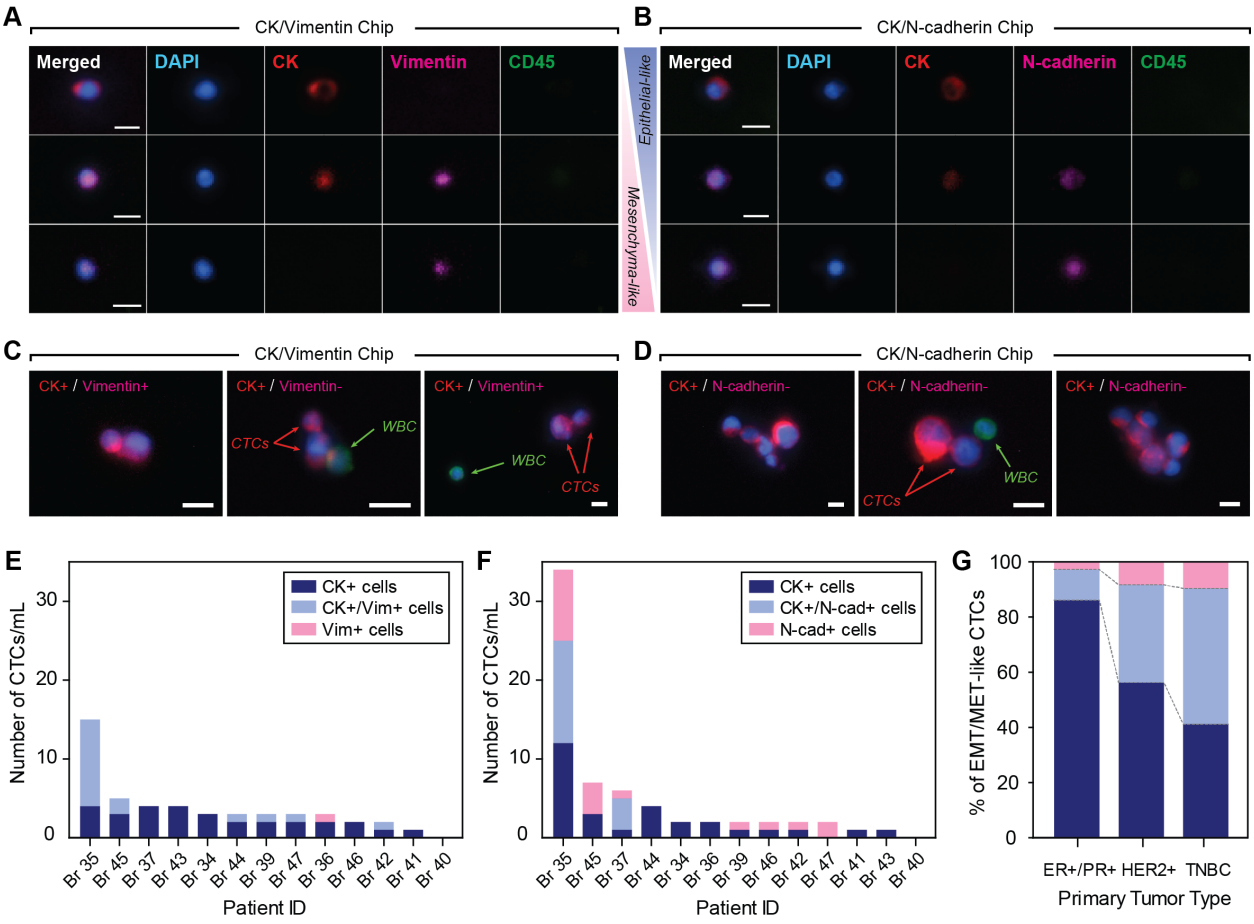

Figure 3.5 Identification of EMT in CTCs.

(A) Representative images of cells classified as epithelial, hybrid/intermediate, and mesenchymal-like CTCs based on their expression of CK, Vimentin, and (B) N-cadherin. (C) Examples of composite image of CTC clusters identified in GO chips stained for CK/Vimentin (D) Examples of composite image of CTC clusters identified in GO chips stained for CK/N-cadherin. (E) CTC enumeration from MBC patients based on CK, Vimentin, and (F) N-cadherin expressions. (G) Average proportion of epithelial, hybrid/intermediate, and mesenchymal-like CTCs by primary tumor subtypes. All scale bar measures 10 μm.

3.6 Multiplex mRNA expression profiling of circulating tumor cells

To explore characteristic markers associated with MBC at the transcription level, mRNA expression patterns were analyzed using multiplex RT-qPCR for 18-selected genes. The quality of RNA from all samples was verified by the internal control, *GAPDH*, which was also used as a reference gene for normalization purposes. Comparison of mRNA expression between MBC patients and healthy controls using unsupervised hierarchical clustering and principal component analysis (PCA) yielded a significant difference between the two groups (Figure 3.6 A, B). The primary discriminating factors included epithelial markers (*EPCAM*, *KRT7*, *KRT8*, or *CDH1*) and the breast cancer-specific marker, *ERBB2 (HER2)*, which were exclusively expressed in patients indicating the presence of CTCs in MBC patients. Genes involved in EMT such as *CDH2* and *TWIST1* were also significantly elevated in the MBC population.

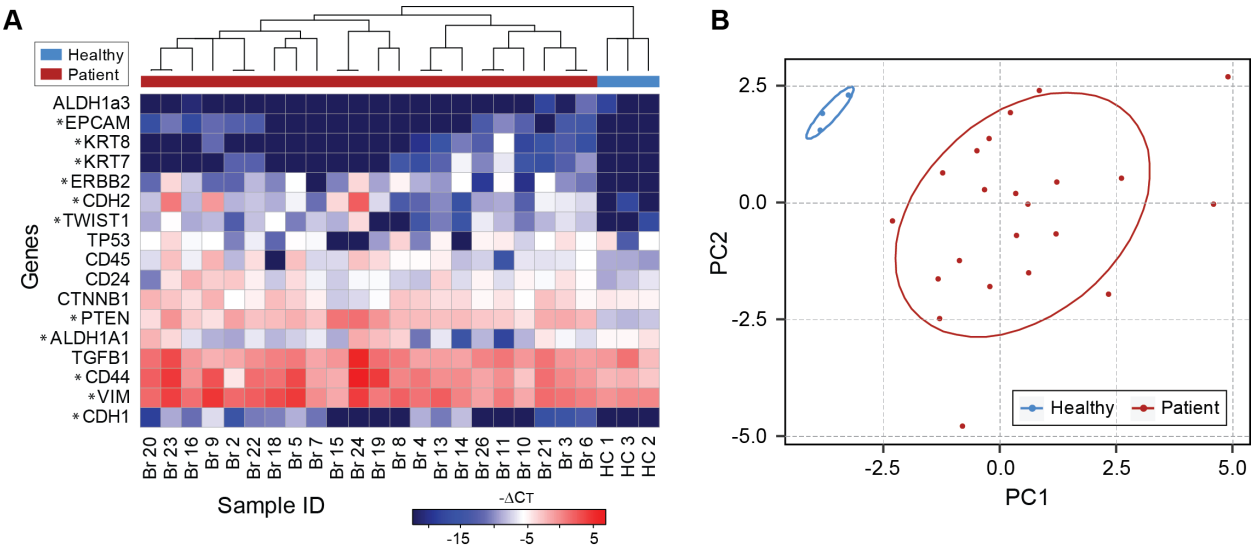

Figure 3.6 Gene expression analysis of CTCs enriched from MBC patients.
(A) Expression heat map of CTC enriched cell population compared with three healthy controls. Data are shown in relative expression to *GAPDH* and plotted as log 2 expression values. P-value < 0.05 (*) (B) Principal component analysis classifying MBC patients and healthy individuals.

We further performed RNA analysis by expanding our gene panel based on pathways aberrant in cancer (Figure 3.7 A). Similar to the previous results, epithelial genes such as, CDH1, EPCAM, KRT7, KRT8, and KRT19 as well as oncogenes including ERBB2 and MET and hormone receptors ESR1 and AR were exclusively expressed in MBC patients. Analyzing the data using the comparative Ct method (2-ΔΔCt) with a log FC cutoff greater than 2, several genes were differentially expressed between patients and healthy groups (Figure 3.7 C). EMT specific transcripts (CDH2, CTNNB1, SNAI1, ZEB1, and ZEB2) and cancer stem cell marker (ALDH1A3) were highly expressed in MBC patients. In addition, genes known to play a role in tumor proliferation (MKI67) and metastasis (MMP9) as well as oncogenes (PI3K and AR) and inflammatory genes (CXCR1, IL6ST, and IL6) displayed increased level of expression in MBC patients. The patients furthermore showed low expression of apoptotic marker, BAX, while exhibiting increased transcription of the anti-apoptotic gene, BCL2, potentially conferring the survival properties of CTCs during transit. Interestingly, upon further analysis, several ECM genes (MGP, LGALS3, and LGALS3BP) which are typically observed in stromal components but not in epithelial tumor, revealed substantially higher expression in MBC patients, suggesting the importance of tumor stromal signaling in priming CTCs for intravasation and metastasis (Figure 3.7 B). No distinct characteristics in gene patterns were observed between tumor subtypes due to the limited sample cohort studied but rather high heterogeneity in overall expression was observed between patients, indicating inter-individual differences.

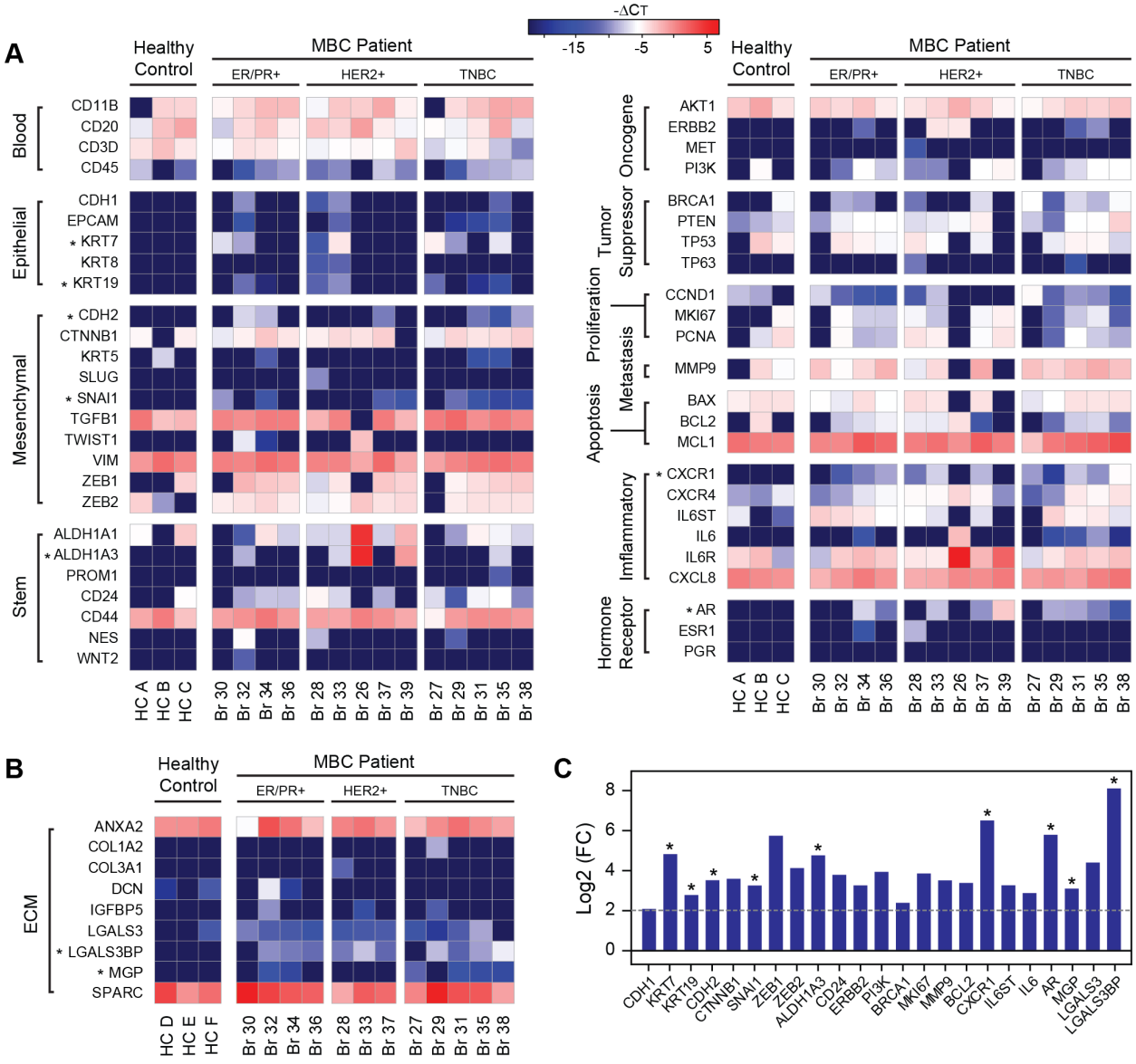

Figure 3.7 Characterizing molecular signatures of CTCs in MBC patients.
(A) Expression heat map of genes represented for epithelial, mesenchymal, stem, oncogenes, tumor suppressor genes, proliferation, metastasis, apoptosis, inflammation, hormone receptors, and (B) ECM genes. Data are plotted as log 2 expressions with MBC patients grouped according to their primary tumor subtypes and 3 healthy donor samples for comparison. P-value < 0.05 (*) (C) Relative expression of differentially expressed genes with log 2 fold change greater than 2. Fold change was calculated using the comparative C_T method ($2^{-\Delta\Delta C_T}$).

Table 3.3 Comprehensive CTC gene panels used for transcriptional analysis.

ALK	ERCC1	MAPK1	TTF-1	KRAS	RB1	AKT1	ALDH1A1
ALDH1A2	ALDH1A3	ANXA2	AR	TRIM29	ATL1	BAX	BCL2
BMI1	BRAF	BRCA1	CCDC80	CCND1	ITGAM	PROM1	CD14
MCAM	MS4A1	CD24	CD3D	CD44	PTPRC	THY1	CDH1
CDH2	MYC	COL1A2	COL3A1	CTNNB1	CXCR1	CXCR4	DCN
EGFR	EMP2	EPCAM	ESR1	GAPDH	GEMIN2	GLI1	IL6ST
ERBB2	HPRT1	IGFBP5	IL6	IL6R	CXCL8	KLF4	KRT18
KRT19	KRT20	KRT5	KRT7	KRT8	LGALS3	LGALS3BP	MCL1
MET	MGP	MKI67	MMP2	MMP9	NANOG	NES	NKX2-1
POU5F1	TP53	TP63	PCNA	PDX1	PGR	PI3K	PON1
PTEN	RAB7A	SHH	SLUG	SNAI1	SPARC	SPON2	TGFB1
TIMP1	TIMP2	TIMP3	TWIST1	VIM	WNT2	ZEB1	ZEB2

3.7 Discussion

In this work, we applied a microfluidic nanomaterial-based chip to isolate CTCs from WB of MBC patients and facilitate the subsequent analysis of those cells. By incorporating GO as the base material of the antibody conjugation chemistry, the GO chip was capable of detecting CTCs from only 1mL of blood with high yield and reproducibility due to the high-density antibody presentation. Also the unique design offering surface capture of CTCs with the modified channel enabled extremely low blood cell contamination rate during sample processing which is essential for multiple downstream analyses. CTC enumeration based on the expression of CK+/DAPI+/CD45- labeled cells revealed increased incidence of detecting CTCs from MBC patients, compared to conventional CTC isolation platforms[7,37]. Correlation of CTC counts or CTC clusters with breast tumor histological subtypes revealed no statistical significance, which aligns with previous observations[70]. However, overall proportion of highly elevated CTC counts (≥ 5 CTCs/mL) were more frequently observed in TNBC subtypes, which may be associated

with its poor clinical outcome[69]. Subsequent analysis using additional markers and multiplex mRNA analysis of the captured CTCs indicated a high level of intra- and inter-patient heterogeneity.

Immunofluorescence staining of captured CTCs with HER2 revealed the presence of both CK+/HER2- and CK+/HER2+ CTCs in MBC patients where oftentimes both phenotypes were detected within the same individual. Overall, a wide discordance over HER2 expression between CTCs and their corresponding primary tumor was noticed. Similar observation has been reported in HER2 protein expression among primary tumor, CTCs, and metastatic lesions[43,44,71,72]. Although this discrepancy maybe caused by the sampling bias during diagnostic biopsy where only a small fraction of tumor is examined, recent study have shown that CTCs can acquire HER2+ subpopulations during tumor progression with a proliferative favor and also interconvert spontaneously in ER+/HER2- primary tumors[73]. In addition, it has been found that HER2 can be selectively expressed in cancer stem cell population and play role in its regulation[74,75]. This may explain in part the association between the presence and high frequency of HER2+ CTCs and shorter disease-free survival and OS seen in previous publication[76]. In this work, we interestingly observed a large number of CK-/HER2+/CD45- cells, which has not been considered in previous correlative studies due to the conventional criteria of defining CTCs as CK+ cells. There is a possibility that these particular cells may have lost their epithelial marker during preparation for intravasation[57,67,68] and may possess potential value for clinical implication. These findings may indicate the need to adjust the standard of defining positivity in HER2 status on CTCs and further re-evaluate method of screening patients that may benefit from HER2 targeted treatments which are currently only administered to patients displaying HER2 gene amplification in their primary tumors.

The plastic properties of CTCs and their ability to alter their expressions of certain epithelial proteins during the metastatic development has led us to further evaluate CTCs using EMT markers. Extensive evidence has shown that CTCs tend to lose their apical-basal polarity, which permits them to effectively detach from the basement membrane and to intravasate into blood streams through adjacent tissues[77]. This process known as EMT is characterized by a loss of cell adhesion, increased migration, and invasion[78,79]. Hence, to compliment the alteration of CK expression, we sought to apply Vimentin or N-cadherin as EMT markers for CTC IF analysis. Heterogeneous expression of EMT markers in CTCs was identified with a spectrum of various phenotypes ranging from epithelial, hybrid/intermediate, and mesenchymal-like cells. Increased levels of EMT specific transcripts such as *CDH2*, *CTNNB1*, *SNAI1, TWIST1*, *ZEB1*, and *ZEB2* in our gene expression analysis further revealed the occurrence of EMT. Notably, we observed higher proportion of Vimentin and N-cadherin expression in CTCs from patients with HER+ or TNBC tumor histology whereas CTCs from ER/PR+ primary tumor were predominantly epithelial. The abundant occurrence of this CTC population in tumor subtypes, which are known to have more aggressive properties, has important implications. In a prior study, serial profiling of EMT transcripts in MBC CTCs using RNA in-situ hybridization showed that decrease in mesenchymal expression during treatment reflects responsive treatment, whereas patients with progressive disease showed increased proportion of CTCs with EMT characteristics[58]. In addition, CTCs presenting EMT markers were more frequently observed in advanced-stage disease[78,79] indicating the association between EMT and cancer progression[58]. Although the captured cells in our study may not be representative for a pure mesenchymal phenotype due to the EpCAM based enrichment method used, studies have indicated that tumor cells with complete mesenchymal characteristics appear to lack the tumor-initiating ability[80,81],

substantiating the use of CK or EpCAM expressing CTCs in indicating the prognosis in MBC patients. It has been assumed that tumor cells co-expressing both epithelial (EpCAM or CK) and mesenchymal marker are suggested to have the highest plasticity and therefore may represent cancer stem cells. This has been supported by recent studies showing that patient derived CTCs with intermediate phenotype have higher metastatic potential after xenotransplantation in mice[82].

Epithelial tumor cells exiting the primary tumor site into the bloodstream are vulnerable to attack by immune effector cells or likely undergo anoikis after losing the adhesion dependent survival signals[83]. For CTCs to survive during transit, a mechanism for these cells to resist the immune attack and prevent apoptotic outcome is essential. Our gene expression data supports this finding by showing an increased level of anti-apoptotic gene, *BCL2,* and decreased expression of its counterpart gene, *BAX*, which have been known to correlate with the severity of malignancy in many types of tumor including breast cancer[84,85]. Furthermore, transcripts involved in cancer inflammation such as *IL-6*, *IL6ST* and *CXCL8* were also highly expressed in our analysis. Certain interleukins such as IL-6 or IL-8 and its receptors acquired in cancer cells have been demonstrated to promote survival signals through autocrine/paracrine signaling that enables them to escape from immune surveillance.

Another interesting observation was the significant increase of stroma-associated transcripts including *MGP*, *LGALS3*, and *LGALS3BP* in MBC patients. These genes are normally expressed in stromal cells, rather than the epithelial cancer, and have been thought to promote the survival of CTCs in circulation[86]. However, recent study has shown that tumor cells at the epithelial-stromal interface appear to express both keratin and ECM genes[87]. Furthermore, abundant expression of ECM genes have been found to be a common feature in majority of CK+ CTCs[87]. Although the functional role of these ECM gene products needs to be further evaluated,

these data supports the possibility that CTCs may express ECM genes to complement the effect of tumor stromal signaling, providing a survival advantage and promote the early growth of metastatic lesion.

One limitation of our GO assay was the false signal presented by contaminating blood cells during the gene expression analysis. To overcome this limitation, we and others have developed a platform which enables CTC collection after antibody enrichment allowing access for single-CTC analysis[88-91]. However, limited yield of releasing CTCs after capture followed by manual manipulation of these cells significantly restricts the use of these platforms for clinical use. Furthermore, due to the difficulty of identifying and selecting CTCs after collection before single cell analysis, the majority of the cells turn out to be leukocytes rather than actual CTCs. Although our analysis relies on the CTC enriched fraction, due to the level of sensitivity and purity inherent in the GO assay, our findings demonstrate the capability to detect and provide transcript level information carried by CTCs relevant to cancer. For future studies, we plan to utilize our GO based CTC assay to analyze CTCs across various cancers and time points and correlate their information to clinical outcomes. The additional advantage of potential inter-changeability of antibodies in our platform will enable us to target markers specifically related to various cancer types improving the isolation performance.

3.8 Conclusion

The GO chip shows high sensitivity with reproducibility in isolating CTCs from MBC patients. The unique surface-capture design enables high cell viability and purity upon blood processing which is amenable to downstream proteomic or molecular analyses. Multi-marker analysis using IF staining and RT-qPCR on the captured CTCs indicated inter-patient

heterogeneity and revealed oncogenetic signatures involved in metastasis including EMT and apoptotic resistant mechanisms which coincide with previous findings. Although clinical significance and implications of these results should be further investigated with a larger cohort of patients, we envision that this current study is the first step towards translating our GO platform into clinical settings, facilitating our understanding of metastasis and helping to identify pathways relevant to potential therapeutic targets for personalized therapy.

CHAPTER 4

4 Size Based Label-free Isolation and Analysis of Circulating Tumor Cells Using Differenential Focusing Using Inertial Forces

4.1 Motivation

Microfluidic technologies for CTC isolation are promising due to their low cost, rapid operation, and the control they offer over the sample processing environments with improved sensitivity. Existing microfluidic CTC separation methods are mainly based on size-based filtration[92], immunoaffinity based capture[18,64], or external force field mediated cell manipulation (i.e. dielectrophoresis[93,94], magnetophoresis [95,96], acoustic wave[97], and optical interference[98,99]). Among various strategies, affinity based CTC binding methods targeting tumor membrane epitopes with antibodies against the epithelial cellular adhesion molecule (EpCAM) provide enhanced recovery rates at a great level of purity. However, non-efficient retrieval of captured CTCs from the chemically functionalized channel surfaces is a major hurdle for these platforms along with their limited sample processing rate[100]. Most importantly, CTCs continuously change their expression level and morphology through the process of epithelial-to-mesenchymal

transition (EMT) during blood circulation[101], and therefore heterogeneously expressed epithelial markers alone cannot adequately identify every subpopulation of CTCs[58,102].

Recently, inertial focusing of finite sized particles using microfluidic systems has emerged as an effective method for continuous CTC isolation[103-105]. Although fluid inertia has historically been neglected in low Reynolds fluid flows, studies show that precise manipulation of particles can be achieved using geometry dependent hydrodynamic forces, which cause size based lateral migration of particles into distinct equilibrium positions[103,106-108]. Such simple passive devices demonstrate the potential for application in biological filtration or purification, as well as blood cell sorting, and may serve as a promising alternative to traditional separation techniques[109]. Since the diameter of epithelial tumor cells is generally larger than that of normal blood cells[110], microfluidic devices exploiting this strong size dependent inertial effect (known as inertial microfluidics) are capable of high throughput, continuous CTC separation without pre-labeling or loss of cell viability. Also, the capability to sort and analyze CTCs without fixation under conditions compatible with downstream molecular and functional characterization steps will allow the utilization of their full clinical potential, beyond simple enumeration[111].

Despite the effectiveness of inertial microfluidic devices, large background contamination associated with normal blood cells in whole blood limits its practical use for CTC specific applications. Since cells are concentrated to a few relatively narrow streamlines during separation, the total volume fraction of suspension is typically required to be below 1% to minimize any cell-to-cell interactions and steric crowding effects that can severely deteriorate the focusing behavior[107,109]. This necessitates a significant dilution of the running sample, which increases the overall processing time or sacrifices the purity of CTCs collected. In addition various channel configurations, diverse flow parameters defined, and the limited flow ranges

tested across previous studies complicate the development of newly designed inertial microfluidic devices due to the lack of continuity between experiments[107,112-114]. This makes them applicable only to particular channel geometries and flow conditions and eventually leads to an unavoidable time-consuming trail-and-error flow optimization process. Currently, due to the lack of controlled information on some structural parameters as well as an incomplete understanding of focusing mechanics, no successful general engineering strategy for design has been proposed and established as of yet. To address these challenges, a systematic channel design strategy for precise control over cell streak equilibriums relative to various flow conditions is necessary. This will allow flexibility and ease of integration with other upstream/downstream lab-on-chip devices to improve critical device performances such as throughput, CTC recovery rate, and purity for clinical cancer research.

In this chapter, spiral microfluidic devices of varying configurations have been investigated to comprehensively study the effect of channel geometry on size based particle migration and separation. We systematically examine the dependence of channel width (W), height (H), and radius of curvature (R) and separately determine their influence on focused particles streak behaviors. By varying each channel parameter, several ordered focusing positions can be achieved at new flow rates, thus allowing application defined flow conditions to be chosen for optimal separation, instead of settling for a fixed flow rate yielding sub-optimal separation and purity. Based on this renewed understanding, we propose an optimal design approach targeting desired flow conditions in a spiral microfluidic device to provide additional flexibility in design with deterministic equilibrium predictions and to enable better integration with other microfluidic technologies. Finally, we introduce a high throughput cascaded spiral CTC separator using our suggested design principles.

4.2 Material and Methods

4.2.1 Sample Preparation

Neutrally buoyant polystyrene microspheres (Polysciences Inc.) with diameters of 10 μm (10.08, σ = 1.3 μm) and 20 μm (18.68, σ = 0.73 μm) were used to examine the size dependent focusing streak behaviors in the spiral channel geometries. Each particle was fluorescently labeled with either DAPI (10 μm particles) or FITC (20 μm particles). Particle suspensions were diluted in deionized water to a final concentration of 2 × 105 particles/mL before running through the device. Mixtures of binary particles were also prepared in solution at a 1:1 ratio (same concentration) mixing to demonstrate the separation quality of these spiral devices.

To further validate its clinical applicability, cells from malignant human breast cancer epithelial cell line, MCF-7 (diameter 16-24 μm), was recovered from a suspension containing leukocytes (diameter 6-15 μm). Leukocytes were extracted from fresh blood specimens drawn from healthy donors using a dextran sedimentation and fractionation method: one part filtered 6% dextran in 0.9% NaCl (Sigma) was added to an EDTA tube containing 10 parts of whole blood[115]. Samples were kept at room temperature for 40 minutes to allow red cells to settle on the bottom of the tube. After collecting the supernatant, the solution was centrifuged at 12000 rpm for 1 min to remove the remaining blood plasma. Cytofix/Cytoperm (BD Biosciences) was then applied to the processed sample and incubated for 30 minutes followed by re-suspension in 1× phosphate buffered saline (PBS, GIBCO, Life Technologies) of pH 7.4. The nuclei of the isolated leukocytes were labeled with DAPI, washed, and again re-suspended to the original blood sample volume. The concentration of this leukocyte suspension averaged around 3-4 ×

106 cells/mL. Subsequently, approximately 1 × 106 cultured MCF-7 cells labeled with green cell tracker dye (Invitrogen, CellTracker Green CMFDA, C7025) were counted and spiked into the leukocyte suspensions, serving as the input sample for the cell separation experiments (Figure 4.1). MCF-7 cells were cultured in DMEM medium containing 10% fetal bovine serum and 1% penicillin-streptomycin solution, and harvested when they reached ~70-80% confluence. A hemacytometer (Reichert bright line, Hausser Scientific) was used to determine the number of particles and cells in suspension during experiments. Cell culture reagents, unless otherwise specified, were purchased from GIBCO Invitrogen Corporation/Life Technologies Life Sciences. Cell samples were processed through the microfluidic chip within 3 hours of preparation.

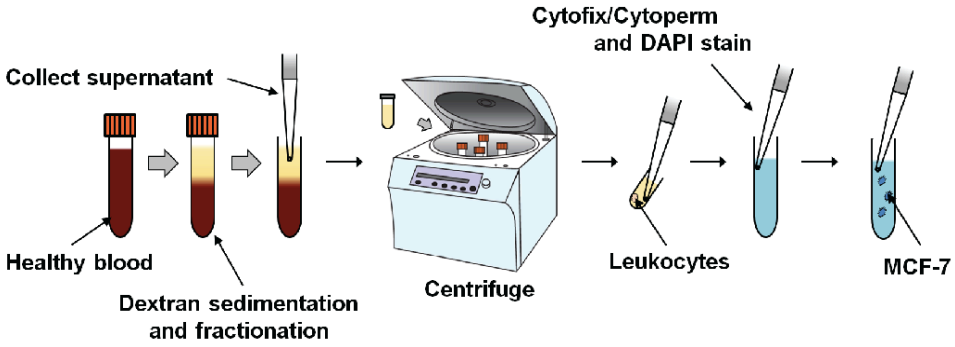

Figure 4.1 Sample preparation procedure for MCF-7 and leukocyte suspensions.

4.2.2 Microfabrication

To fabricate the spiral microfluidic devices, a silicon master mold was produced using a conventional photolithography process. Briefly, a negative photoresist, SU-8 (2025, Microchem Corp.), was spun on a flat 4-inch silicon wafer to a desired thickness, exposed to UV light through a printed photomask (Fineline Imaging), and developed. Microchannel replicas were formed by casting a 10:1 ratio mixture of polydimethylsiloxane (PDMS, Sylgard 184, Dow Corning) elastomer and curing agent onto the patterned silicon/SU-8 master using standard soft lithography methods. After degassing and curing in an oven for 6 hours at 65 °C, the PDMS channels were peeled off and flip bonded to a plasma treated microscope glass slide (Fisher Scientific). To ensure complete bonding, devices were heated on a 65°C hot plate for 10 minutes. Inlet and outlet ports were manually punched with a coring tool (Harris Uni-core). Tygon tubings (Cole-Parmer) were then press fitted into the holes, forming tight connections.

4.2.3 Experimental Setup

Following air plasma exposure and glass bonding, the PDMS microchannels were soaked with 0.1% pluronic (F127, Sigma) and incubated for 30 minutes to block the channel surfaces and prevent adhesion or clogging during sample flow[116]. After washing with deionized water, the device was mounted on an inverted epifluorescence microscope (Ti Eclipse, Nikon) equipped with a 12-bit monochromatic CCD camera (Retiga 200R, Qimaging). Particle or cell suspensions were loaded with a syringe and infused through the channel at varying flow rates using a syringe pump (PHD2000, Harvard Apparatus). For a given channel geometry, streak positional data and width measurements were obtained by averaging five consecutive line scan

images taken with Nikon NIS-Elements AR 4.0 software at each flow rate. For every initial sample flow and changing flow rates, images were captured after waiting 1 minute to ensure a complete flow development and pressure stabilization.

Several low aspect ratio spiral microfluidic devices were designed by varying each geometric parameter to systematically study the effect of channel geometry on particle focusing behaviors (Figure 4.2). The variables considered were the height, width, and radius of curvature. Each device consisted of an inlet with a filter region to prevent debris and particle aggregates from entering the microchannel, multiple 180° sections of curvatures followed by an outlet. Initially, a single turn of a specific radius of interest, ranging from 1250 to 20000 μm, was connected before an outlet where the focusing particle streaks were imaged and analyzed. Additional consecutive turns with a 500 μm increment in radius of curvature were added to provide sufficient channel length to allow particles to reach their equilibrium positions completely. The lengths of each devices were calculated based on the lateral migration velocity of 10 μm diameter particles along the channel width resulting from the inertial forces for the lowest measured flow rate[109]. Samples were run through the device from the largest radius of curvature inward. By modifying the width and height of the channels, from 200 to 400 μm and 50 to 100 μm respectively, streak images for different particle sizes were obtained. The inlet and outlet were large enough to fit the tubing for particle injection and collection.

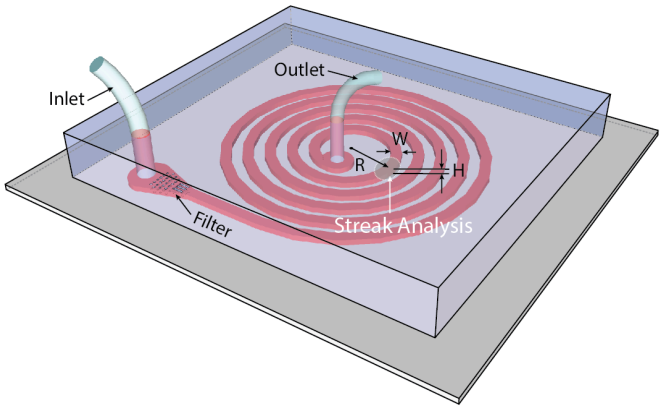

Figure 4.2 Schematic representation of the spiral device design for particle focusing and streak equilibrium characterization.
Each device consists of an inlet, filter, and consecutive channel curvatures to ensure complete focusing of 10 and 20 μm particles, followed by an outlet. Prior to the outlet exists a curved channel structure of particular interest for streak analysis. Channel width, height, and radius of curvature at this analysis region have been systematically varied to observe the channel's geometric effect on streak migration behaviors.

4.3 Theoretical Background of Inertial Forces

After Segré and Silberberg first introduced inertial focusing of particles in cylindrical Poiseuille flow[117], the mechanics of particle train migration across streamlines in finite Reynolds number (*Re*) fluid flow have been well characterized as the balance of two dominant inertial lift forces acting normal to the flow direction[118,119]. A shear induced lift force (F_S) caused by the parabolic velocity gradient drives particles toward the channel wall, while a wall induced lift force (F_W) pushes back particles toward the channel center due to the interaction with adjacent walls. This yields an annulus equilibrium at ~0.2*D* away from wall, where *D* is the diameter of the pipe. However, in straight microfluidic channels, there is a radial asymmetry present from the normally square or rectangular cross-section geometry. In this case, particle streaks similarly migrate and settle at ~0.22*H* (or *W*) near the channel wall[120], but concentrate toward the wall's center from the rotation induced lift force (F_R)[121]. More specifically, for high or low aspect ratio

channels ($H/W >> 1$ or $<< 1$), only two equilibriums centered at the longer sidewalls develop from the added asymmetry rather than four. Using a point-particle assumption, the net inertial lift force (F_L) is known to scale uniformly throughout the channel and is given by

$$F_L = \frac{\rho {U_m}^2 {a_p}^4}{{D_h}^2} C_L$$

where ρ is the density of the fluid medium, U_m is maximum fluid velocity approximated as $U_m \approx 1.5 \times U_{avg}$, and C_L is a non-dimensional lift coefficient that is a function of channel Reynolds number ($R_c = \rho U_m D_h / \mu$) and is dependent on the particle's position[119,122].

Introducing a curvature to the channel structure develops a secondary lateral flow, known as Dean flow, which is characterized by two counter-rotating vortices located above and below the central plane of symmetry of the channel[106,112,120]. The magnitude of this flow is described by a dimensionless Dean number (D_e) given by

$$D_e = \frac{\rho U_m D_h}{\mu} \sqrt{\frac{D_h}{2R}} = R_c \sqrt{\frac{D_h}{2R}}$$

where, μ is the fluid viscosity, and R is the radius of curvature of the channel. According to Stokes' Law, Dean flow leads to a drag force upon particles (Dean force, F_D) expressed as[107]

$$F_D \sim 5.4 \times 10^{-4}\, \pi \mu {D_e}^{1.63} a_p$$

Thus, in curved microfluidic channels, the combination of inertial lift force (F_L) and additional Dean force (F_D) results in a Dean coupled inertial migration of particles, which ultimately determines the final equilibrium.

A visual representation of the Dean coupled inertial focusing profiles of particles in a curved low aspect ratio microchannel is shown in Figure 4.3. Randomly dispersed particles injected from the inlet are first abruptly driven towards the top and bottom wall due to a steep shear gradient along the vertical direction of the channel. These particles constantly settle at 22% and 78% of the channel depth[120] from the counterbalancing wall lift, forming two broad bands. Comparatively, the flat shear gradient in the horizontal direction has less effect at this stage. At a low flow velocity, rotation lift forces slowly concentrate these bands into two focusing streaks near the channel center as particles propagate further through the channel (Figure 4.3 (A). i). Here, particle migration occurs as if in straight channels where Dean flow is mostly negligible from the strong lift as a result of limited fluid flow. However, as the flow velocity is increased, an inner wall migration is induced by the apparent Dean forces oriented toward the inner wall, which become nontrivial at higher channel Reynolds numbers (Figure 4.3 (A). ii). This migration occurs until a particular threshold where single point focusing is achieved along the height of the channel resulting in a tight equilibrium closest to the inner wall (Figure 4.3 (A). iii)[114]. Increasing the flow velocity past this threshold results in an outer wall migration where, again, the two particle equilibrium position near the top and bottom of the channel emerges and shifts back towards the outer wall (Figure 4.3 (A). iv).

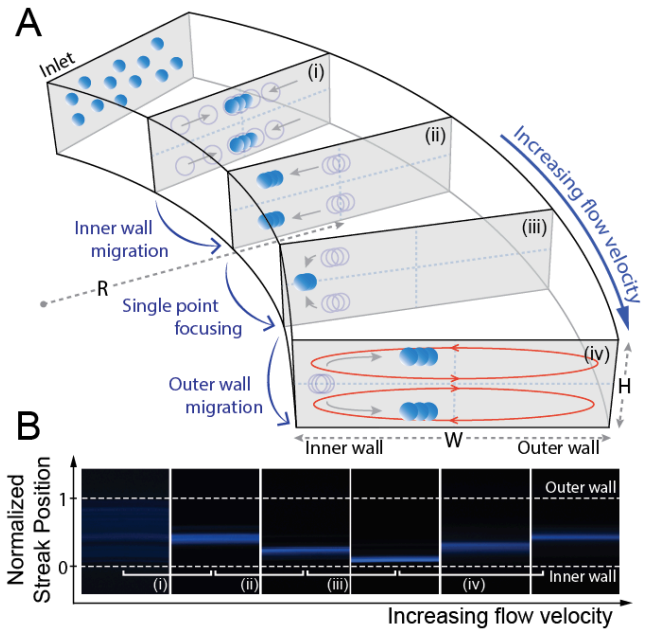

Figure 4.3 Inertial focusing and migration behaviors of particles with increasing fluid flow velocity (U_{avg}) in a curved low aspect ratio microchannel.
(A) Particles injected from the inlet of the channel first abruptly equilibrate into two broad bands near the longer channel wall under the influence of shear lift (F_S) and wall lift forces (F_W) acting vertically with respect to the channel height. (*i*) At a relatively low flow velocity, particles migrate laterally towards the center equilibrium due to a rotation lift force (F_R), forming two focusing streaks. (*ii*) As the flow velocity increase, the two streaks start to migrate towards the inner channel wall, followed by (*iii*) a single point focusing at a particular threshold due to the differential interplay between the net lift force (F_L) and the Dean drag force (F_D). (*iv*) Outer wall migration is induced as the flow velocity is increased above this threshold. (B) Top down view of fluorescent images illustrating the migration pattern of 10 μm diameter particle in a curved microchannel (200 μm × 50 μm cross-section at 20000 μm radius of curvature).

4.4 Parametric Study of Geometric Effect on Particle Focusing

4.4.1 Size based Differential Focusing

Inertial focusing and migration behavior of particles of different sizes were evaluated by analyzing the fluorescent intensity profiles of the particle streak distributions across the channel width (Figure 4.2). 10 μm and 20 μm diameter particles, fluorescently labeled with DAPI and

FITC, were used to model leukocytes and CTCs. For these experiments, a curved channel of 300 μm width, 50 μm height, and 5000 μm radius of curvature was used. Composite images of 10 μm and 20 μm diameter particle streams were captured and arranged (Figure 4.4 (A)). Focused particle streak patterns were plotted as a function of average flow velocity, a parameter included in both non-dimensional channel Reynolds number (R_c) and Dean number (D_e).

Similar migration patterns were observed regardless of size as both 10 and 20 μm particles experienced inner wall migration followed by outer wall migration with increasing flow velocity; however, the size difference caused a relative shift in the overall migration pattern which allows for efficient sized based separation of the particles. Specifically, a 'left shift' in the migration pattern of the 10 μm particles was observed relative to the 20 μm particles. This was produced by two differential size-dependent factors reliant upon the interplay between Dean and lift forces: the initial focused streak position and particle migration rate.

Initial focused streak positions, defined as the first equilibrium positions that arose once a minimum focusing velocity was reached by both particles, was a function of particle size where the initial focused streak position of 10 μm particles was closer to the inner wall in the given channel geometry. For these small particles, the Dean force appeared to be non-negligible relative to the net lift, which scales with the fourth power of the particle diameter, even at the minimum focusing velocities. In contrast, stronger net lift forces experienced by larger particles dominated the Dean force thereby maintaining the 20 μm particles' initial equilibrium position near the channel center for a greater span of velocities. In effect, there was a delayed response for larger particles, which required higher fluid velocities to begin the inner wall migration phase. Furthermore, migration rate with constant flow increment for both inner and outer wall migration differed with particle size. With increasing fluid velocities, 20 μm particle streaks

slowly migrated towards the inner wall while faster migration was observed during the outer wall migration compared to 10 μm particle streaks. Thus, this distinct response, which is highly dependent on the diameter of particles, enables size based differential streak positioning and hence successful separation of binary particles in curved microchannel geometries.

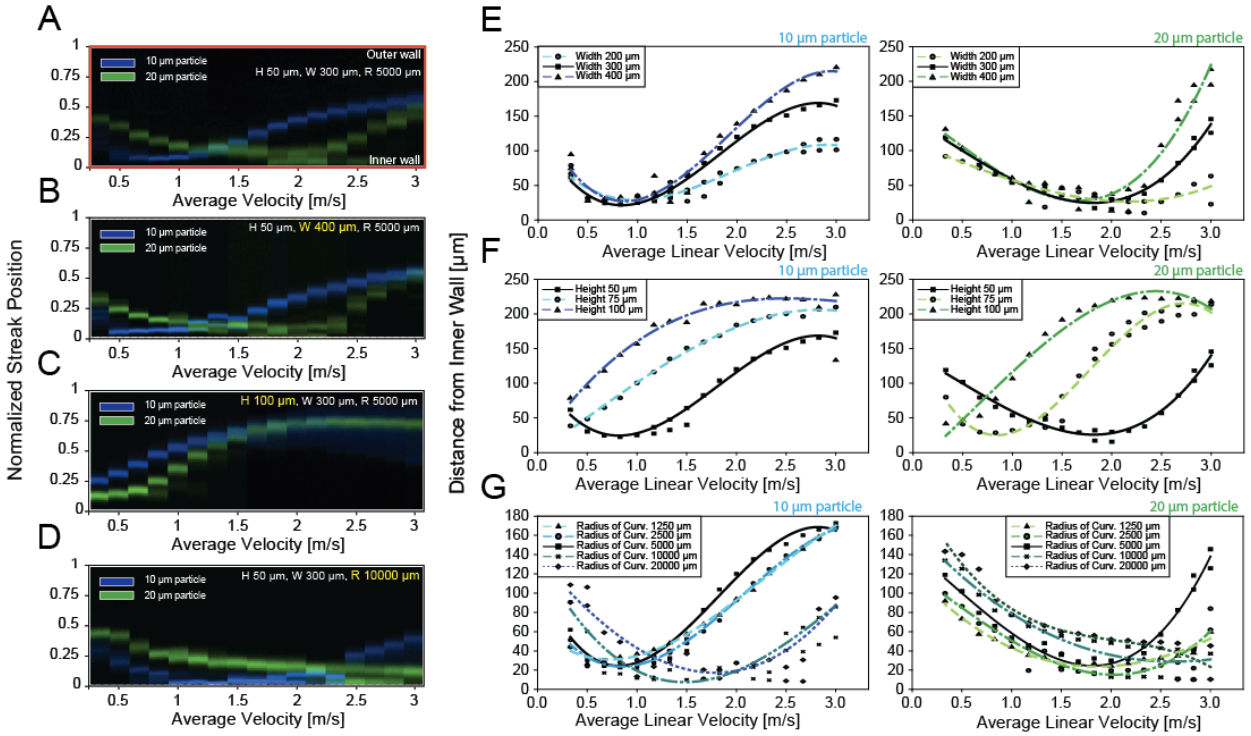

Figure 4.4 Inertial focusing and migration behaviors of different sized particles in varying channel geometries.

(A) Composite fluorescent line-scan images of 10 μm (blue) and 20 μm (green) polystyrene particle streaks are plotted as a function of average flow velocity (U_{avg}) in a curved microchannel with a 300 μm × 50 μm cross-section at 5000 μm radius of curvature. Y-axis represents the normalized streak distance from the inner channel wall. Migration pattern of 10 μm and 20 μm diameter particles are re-constructed at a modified channel (B) width (W = 400 μm), (C) height (H = 100 μm) and (D) curvature of 10000 μm. Positional information where peak intensity of 10 μm and 20 μm particle streaks occurred is measured for varying channel (E) width (W = 200-400 μm), (F) height (H = 50-100 μm), and (G) radius of curvature (R = 1250-20000 μm). Data points represent the raw measurement value and are curve fitted through the averaged peaks.

4.4.2 Geometric Effect on Particle Focusing Patterns

To investigate the effect of channel geometry on the lateral migration of particle trajectories, width, height, and radius of curvature were individually varied from the previous spiral design with initial dimensions of 300 μm width, 50 μm height, and 5000 μm radius of curvature prior to the outlet. Channel Reynolds number and Dean number values corresponding to each channel structures are given in Figure 4.5. Images and experimental data illustrating the channel's geometric dependency of streak motion behaviors are shown in Figure 4.4. With a large span of average velocity, ranging from 0 up to 3 m/s, focusing particle equilibrium positions were measured by calculating the distance from the inner channel wall to the peak fluorescence position for 10 μm and 20 μm diameter particles.

As shown in Figure 4.4 (B), channels of varying width (W = 200 μm - 400 μm) displayed little effect on the normalized streak migration patterns. Regardless of channel width, particle streaks exhibited similar behavior in inner wall migration patterns, reaching a minimum distance to the inner wall at a specific flow velocity around 0.8 m/s and 1.8 m/s for 10 μm and 20 μm diameter particles respectively (Figure 4.4 (E)). In contrast, channels of varying height (H = 50 μm - 100 μm) induced a major shift in the normalized streak migration patterns (Figure 4.4 (C)). With increasing height, streak patterns of both particle sizes tended to shift left (Figure 4.4 (F)). This can be explained by the growing Dean force paired with decreasing inertial lift forces at a given average flow velocity. Interestingly, for channel heights above 75 μm, the inner wall migration patterns were no longer observable. This provides insight as to why only the outer wall migration was observed in certain previous geometries in literature[107,120]. These two results confirm that in a curved low aspect ratio microchannel, the shortest channel dimension in the channel cross-section acts as the critical factor in determining streak equilibration positions[123].

Also, this clearly indicates that a simplistic geometric aspect ratio is insufficient to predict the final focusing positions of particles. Rather than the aspect ratio value itself, each channel parameters that show different effects on migration patterns should be independently considered.

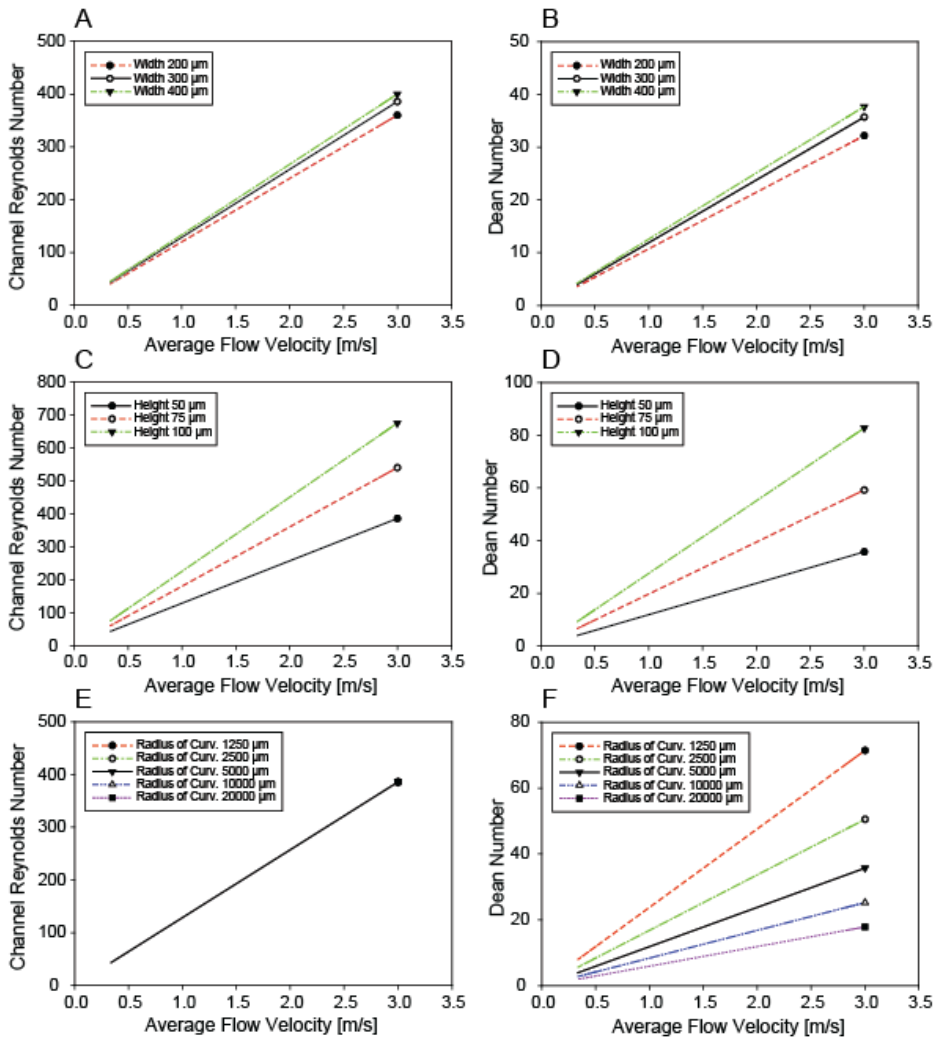

Figure 4.5 Channel Reynolds number and Dean number as a function of average fluid flow velocity for different spiral channel geometries.
(A, B) Channel width, (C, D) height, and (E, F) radius of curvature are modified from an initial channel geometry of 300 µm width, 50 µm height, and 5000 µm radius of curvature spiral channel.

Along with the width and height, the effect of the channel's radius of curvature (R = 1250 μm - 20,000 μm) on particle focusing position is shown in Figure 4.4 (D, G). Differences in channel curvature modify the Dean number ($D_e \propto \frac{1}{\sqrt{R}}$) and therefore the Dean force, although the linear velocity remains constant. This allowed for further investigation into particle streak behavior by imposing a distinct Dean flow field on a constant net lift force. The Dean and lift forces could then be uncoupled and compared so that the curvature could be manipulated in order to achieve maximum separation for a given system. With increasing curvature, the Dean force decreased resulting in a diminished rate of inner wall migration. As a result, particle focusing positions reached a minimum distance from the inner wall at higher linear flow velocities (Figure 4.4 (D)). Additionally, the inner wall migration occurred in order of ascending curvature, where migration in smaller channel curvatures began at lower flow velocities (Figure 4.4 (G)). Beyond a curvature of 20,000 μm, where Dean numbers approached their asymptotic limit, no obvious change in streak behaviors was observed.

Through the quantification of equilibrium positions, migration rates of each particle streak not only differed by particle size but also had distinct slope constants dependent on each channel configuration. However, these slope constants within the presented experimental data set slightly differed from previous classifications[114]. During streak measurements, it was found that at high flow rates, high pressure built up inside the PDMS microchannels and started to distort the cross sectional dimensions, thus altering the equilibrium positions significantly. To examine how the pressure induced geometric deformation affects streak equilibriums, two spiral channels were fabricated with different channel lengths (Figure 4.6(A)). At the overlapping flow ranges tested (900-1000 μL/min) with the two spirals, the device with longer length showed a large channel expansion due to higher pressure (Figure 4.6 (B)). Increase in channel cross

section tended to decrease the average linear flow velocity while increasing the Dean flow, causing a large shift in streak patterns under identical flow conditions and channel geometric parameters (H, W, R). This was similar to increasing the height of the channel, since the deformation mainly occurred in the height direction in low-aspect-ratio microchannels[124]. Thus, to acquire accurate particle response to inertial force effects, streak positions needed to be measured taking into account of the total channel length not only to ensure complete focusing but also to avoid pressure induced geometric deformation of the PDMS microchannels. In our experiments, each data was acquired before the channel had observable deformation.

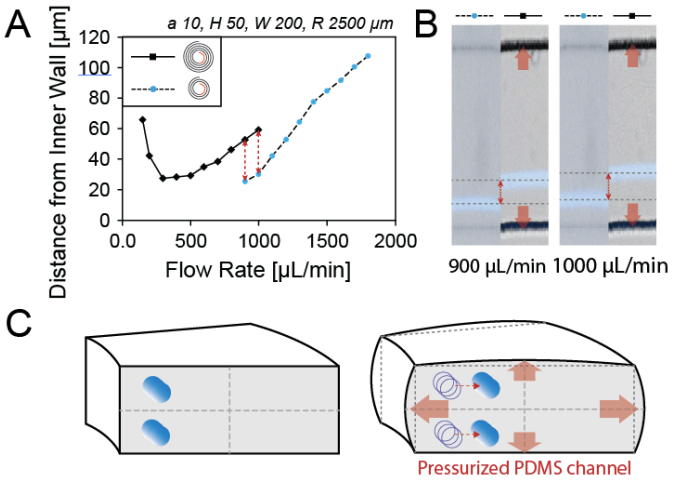

Figure 4.6 Pressure induced deformation of PDMS microchannel and its effect on particle streak equilibrium.
(A) Equilibrium positions of 10 μm focused particle streaks are measured using two spiral devices with identical channel configurations (analysis region (Figure 4.2)) but different channel lengths. (B) Composite image of the channel wall (bright field) and 10 μm particle streaks (fluorescent) imposed are shown at the overlapping flow ranges tested. (C) Schematic illustrating the channel cross section being pressurized and the corresponding streak shift induced during outer wall migration phase.

4.4.3 Optimal Flow Regimes for Efficient Particle Separation

State diagrams for the separation distance between 10 μm and 20 μm particle streaks were acquired by measuring the proximity between the boundaries of the focused streak widths, which was calculated from the full width at half peak maximum of the fluorescent intensity profile from the background noise floor (Figure 4.7). To better apply these parametric data sets in designing spiral devices for separation and estimating the proper flow conditions, state maps were plotted as a function of volumetric flow rates.

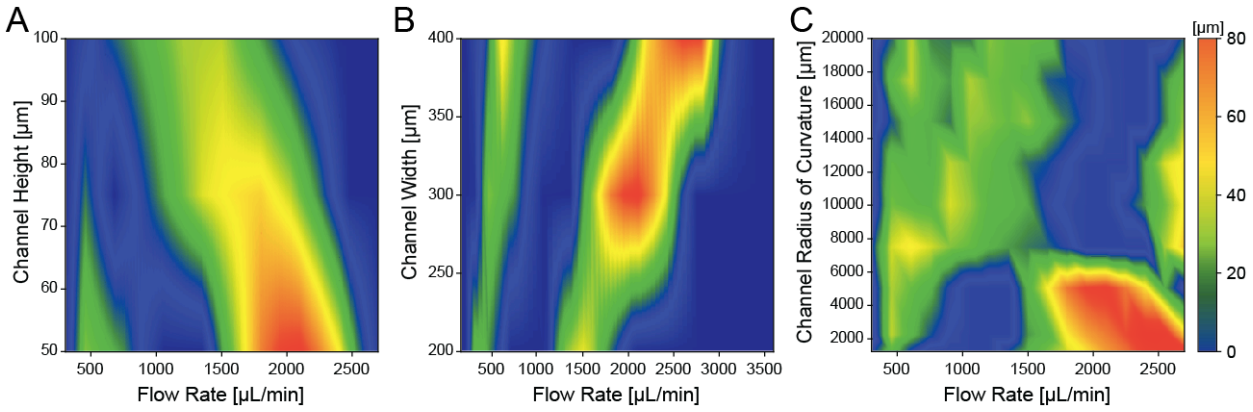

Figure 4.7 State diagrams of separation distances between 10 μm and 20 μm focused particle streaks.
measured by the half-width-peak intensity as a function of volumetric flow rate in a (A) curved channel with rectangular cross section of 300 μm width and varying height, at a 5000 μm radius of curvature; (B) curved channel with rectangular cross section of 50 μm height and varying width, at 5000 μm radius of curvature; (C) curved channel with rectangular cross section of 50 μm × 300 μm ($H \times W$) with varying curvature. State maps are generated using linear interpolation from individual data points obtained experimentally in units of micrometer.

From the difference in equilibrium patterns, two distinct separation regimes existed respectively at low flow and high flow rate ranges. For these two regimes, the ordering of focused particles occurred in a reversed manner; that is, in the low flow separation regime the smaller particle streak was closer to the inner channel wall, whereas the opposite occurred in the

high flow separation regime (Figure 4.8 (A)). Once the focused particles reached the nearest inner channel wall, the finest focusing quality was obtained which was specified by a narrow fluorescent intensity profile with few fluctuations. Better focusing near the inner channel wall indicated that the counterbalance between competing Dean drag and net lift forces was occurring at this point. Additionally, this focusing position for 20 μm particles remained constant for a longer span as the flow velocity increased. In contrast, the 10 μm diameter particle streaks switched their migration direction more abruptly and a slightly higher separation resolution was achieved between the two streaks in the high flow separation regime. However, both regimes offered a high separation rate (> 90%) of binary particles, providing an additional flexibility in flow rate defined designing of inertial based spiral devices.

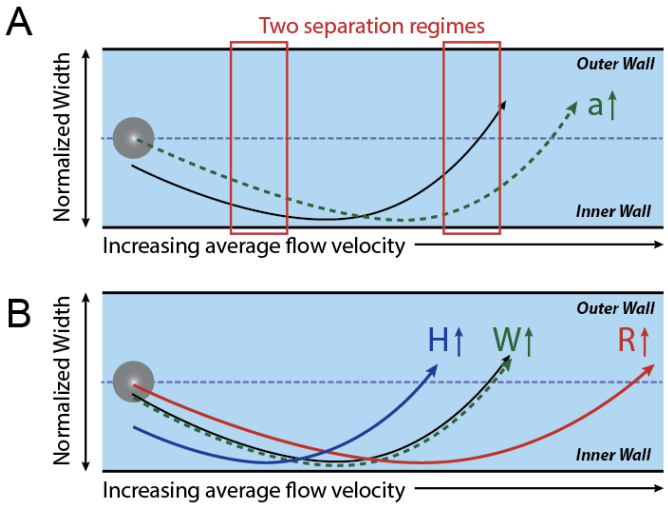

Figure 4.8 Schematic illustration of streak migration patterns.
(A) streak migration patterns of different size particles and (B) the influence of each channel's geometric parameter. Black line represents a reference condition.

4.4.4 Flow defined Design Strategies for Inertial Microfluidic Device

Quantitative characterization of the effect of channel geometry on particle focusing and migration behaviors to better understand their full transient behavior in response to the change in

flow rate in curved microchannels offers a systematic design guideline for efficient inertial separation of particles under various conditions. To efficiently adjust the channel design to a desired optimal flow condition, each of the geometric factors can be independently modified based on predictions of its influence on equilibrium patterns. Since focusing positions of particles are most sensitive to the variation in channel height, it is essential to first accurately define the channel height and the corresponding flow velocity that allows greatest separation. In particular, cases that require specific particle positions and the ordering must operate in the low flow separation regime, consequently the height of the channel needs to be designed below 75 μm for 10 and 20 μm particle separation (Figure 4.7 (A)). The optimal flow rate in the high flow separation regime, on the other hand, can be freely tuned by varying the channel height as long as the particle focusing requirement $a_p/D_h \geq 0.07$ is satisfied[26].

Once the height is determined, the total sample throughput can be subsequently adjusted by modifying channel width. As long as the low aspect ratio condition is preserved, the normalized streak patterns are mostly invariant to the width factor. Increasing the channel width not only offers a simple linear increase in volumetric flow rate but also in separation resolution (Figure 4.7 (B)), since the gap between the two particle streaks as well as the streak dispersion (streak width) scales linearly with the channel width. One tradeoff of this would be an increase in device footprint due to the longer channel length required for complete focusing.

With increasing radius of curvature, both inner wall and outer wall migration phase occurred gradually. This adds tolerance to any flow rate variations during device operation since streak equilibrium position varies less per unit flow increments. Applying precise flow is critical for inertial separation devices yet this is often difficult to control. However, desensitizing a device to flow rate variation through increased channel curvature can offer improved stability

and yield in separation performances. Optimal flow rates for both separation regimes can also be pushed further up to a higher flow rate in a large channel curvature as long as the pressure accumulation does not exceed the device failure condition (Figure 4.7 (C)). Thus, by engineering the channel width, height, and radius of curvature simultaneously, inertial devices tailored to operate at any flow rate conditions within the range of approximately 200 to 3000 μL/min can be easily designed and controlled for optimal particle separation.

4.4.5 Focused particle streak breakdown

Some of the unpredictable phenomena such as dual focusing and streak breakdown hindered the process of designing optimal separation devices. Dual stable equilibria often occurred when the particle streaks reached the nearest inner channel wall. In some cases, during the inner-to-outer wall transition, single point focusing equilibrium showed less dominancy over the pre- and post-state equilibriums resulting in three equilibrium positions. This was more obvious at larger curvatures where the particle migration rates decreased and the migration occurred more gradually (Figure 4.4 (D)). While stable focusing was maintained during streak migration of 20 μm particles across the centerline of the channel width, 10 μm particles showed a complete defocus during the outer wall migration (Figure 4.4 (C)). 10 μm particles with smaller confinement ratio (a_p/H) were subjected to dominant Dean drag force while 20 μm particles maintained focused from the competing lift forces. Thus, defocusing occurred more obviously while the channel height increased. To further elucidate the exact dynamics of streak migration and more accurately estimate its equilibria by theoretical calculations and understand focus breakdowns, a three-dimensional computational model should be developed in future studies.

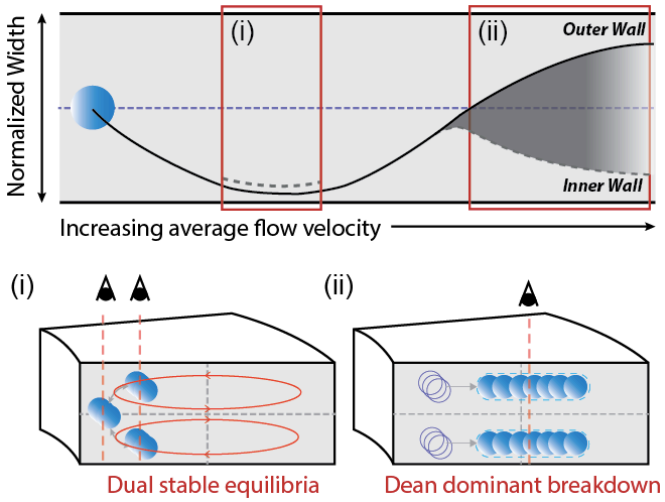

Figure 4.9 Focused particle streak breakdown.

4.5 Cascaded Spiral Device Design and Characterization

Based on these parametric observations, we designed and fabricated a fully integrated cascaded spiral microfluidic chip for CTC isolation. Through these studies we aimed to establish the clinical applicability of the founding principles to design better device for sensitive and specific separation. For a sheath-less, continuous two-stage separation, two consecutive spiral structures were serially connected with bifurcating channel sections located at the end of each spiral channels to isolate CTCs from leukocytes with high purity (Figure 4.12 (A)). Operating flow rate was determined from the low flow separation regimes to specifically position CTCs, which are generally larger than the rest of the blood cells, closer to the channel center during separation. Without any repetitive optimization processes, this cascaded channel structure including the dimension of both bifurcating outlets was designed in a single attempt by precisely predicting cell equilibrium positions at specific flow conditions.

Sample mixtures of MCF-7 and human leukocytes were used which were previously represented by the 20 and 10 μm diameter particles respectively. MCF-7 breast cancer cells were chosen here to model the presence of CTCs in human peripheral blood of metastatic cancer patients. Cells injected at an initial flow rate of 550 μL/min from the inlet started to focus while traveling along the 400 μm width and 50 μm height spiral channel. By the time cells reached the first bifurcating region (R = 5000 μm), the majority of leukocytes were focused near the inner channel wall and filtered out through a 30 μm width sub channel while MCF-7 cells and the remaining leukocytes continued to flow along the main channel which narrows down to a width of 200 μm. Finally, after an additional focusing and second bifurcation (at R = 2200 μm), MCF-7 cells were recovered at an average separation efficiency of 86.76 % with a 97.91% leukocyte depletion rate (Figure 4.12 (B)). These numbers were comparable to complicated current continuous immunoaffinity based depletion techniques[39]. The viability of MCF-7 cells after collection was examined with live/dead cell viability assay (GIBCO, Life Technologies) and remained above > 90% with most cells retaining their initial morphology.

Optimal flow conditions for separation predicted from the particle studies matched well with cell experiments but showed subtle differences in streak positions. In contrast to rigid leukocytes, MCF-7 cell streaks tended to migrate towards the inner channel wall earlier than the estimated flow rate, causing a slight left-shift in its overall streak pattern. The cell elasticity and deformability of MCF-7 cells subject to high shear resulted in a physical shape change, compared to rigid spherical particles. However, this was not significant enough to deteriorate the quality of the separation and with a slight calibration accounting for the streak shift of cells (adjusted within a few ~10's of μL/min), a successful sheath-less, two-step CTC isolation was achieved with high purity using the given geometric design parameters.

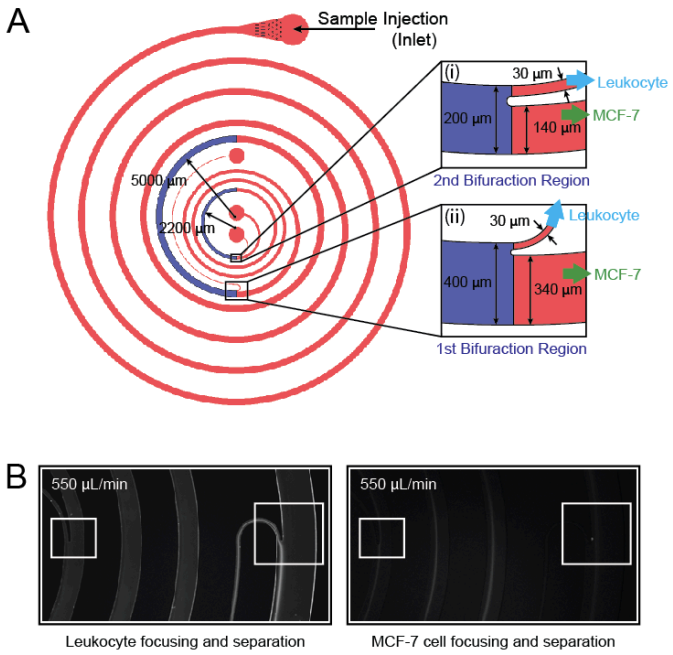

Figure 4.10 Design of the cascaded spiral device.
(A) Schematic and operating principle of the low aspect ratio cascaded spiral separator are shown with its dimensions at each bifurcation regions. Channel height is fixed to 50 µm and the cell mixture is injected through the inlet at a flow rate of 550 µL/min. (B) Top down fluorescent streamline image of focusing streaks of leukocytes (left) and MCF-7 cells (right) near the two bifurcation region in the cascaded spiral separator.

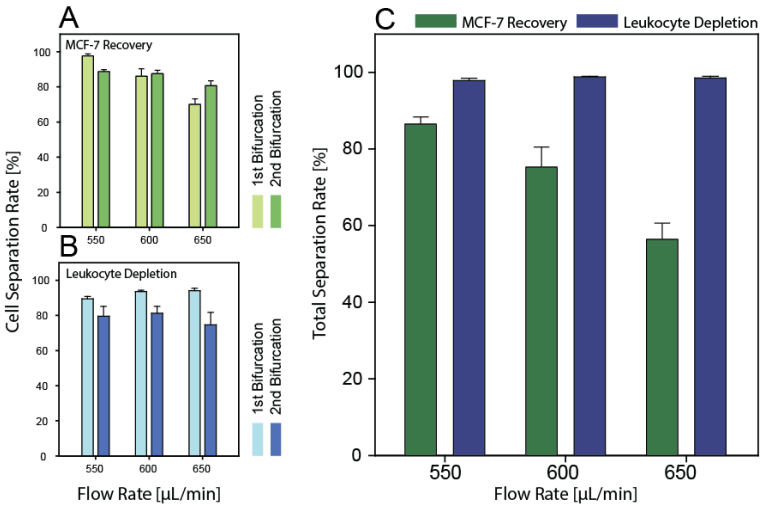

Figure 4.11 Cell separation efficiency in a cascaded spiral microfluidic chip.
(A) Recovery rate of MCF-7 cells and (B) leukocyte depletion rate is shown after processing through the 1st, 2nd separation region at different volumetric flow rates. (C) Total separation efficiency of the cascaded spiral device is calculated after sample collection. Error bars represent the standard deviation of the results from three experiments.

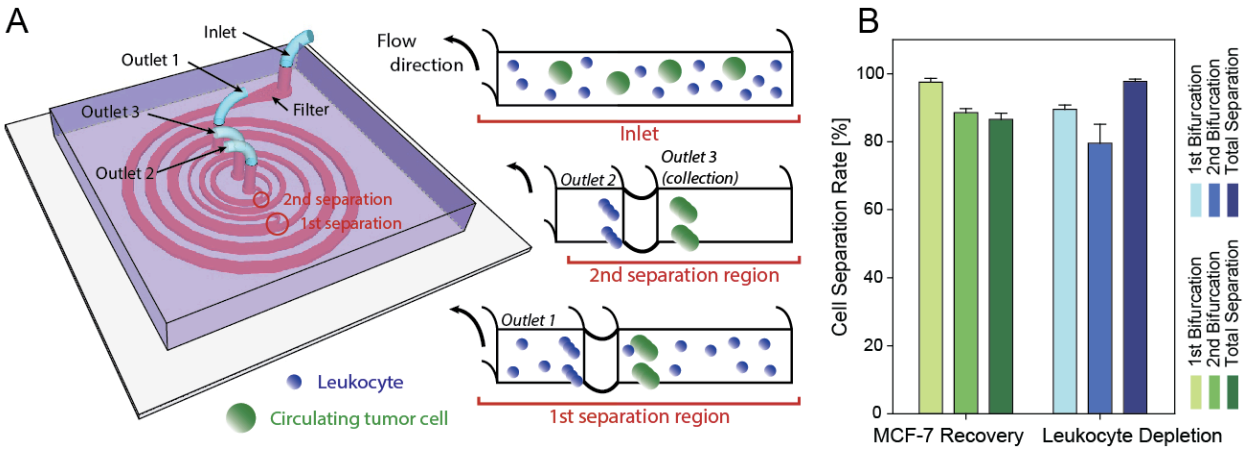

Figure 4.12 Cascaded spiral microfluidic device characterization.
(A) Schematic illustrating the fully integrated cascaded spiral microfluidic device. (B) Characterization of cell separation efficiency.

4.6 Conclusion

In this chapter, the inertial focusing mechanics and streak behaviors in various curved channel configurations over a large parametric space is presented and experimentally examined. The channel height, width, and radius of curvature each independently had distinct effects on particle equilibrium and streak patterns. This complete systematic study of geometric factors would be advantageous in envisioning a base guideline for predicting the equilibrium positions of particles and cells in the device development stage with an improved understanding of the underlying physical mechanisms and their limitations. Channel design strategies for specific flow rates introduced along with the state diagrams would simplify the process and reduce the trials attempted for device optimization as well as permitting additional flexibility that enables integrations with other lab-on-chip systems and microfluidic technologies, which is currently limited. Based on this design principal, we developed a high-throughput, fully integrated

cascaded spiral microfluidic device to isolate MCF-7 cells from leukocytes with high purity in a continuous manner. The device was designed in a single attempt to operate at a pre-determined flow condition without any repetitive channel optimization procedures or complicated sheath flow control, to achieve an overall MCF-7 recovery rate of 86.76% and 97.91% leukocyte depletion rate. By applying and demonstrating the robust ability and performance of a spiral design to enrich cancer cells from leukocyte mixtures, we expect that the deterministic models for channel design suggested in this report will be readily applicable to the further development of low cost, high throughput, continuous CTC separation medical devices.

CHAPTER 5

5 Indwelling Catheter System for Circulating Tumor Cell Isolation and Analysis

5.1 Motivation

The major cause of cancer-associated mortality is closely linked to distant metastases. The metastatic lesions arise from circulating tumor cells (CTCs) that are shed from the primary tumor and circulate through the bloodstream of cancer patients[125]. Consequently, CTCs hold great promise as a biomarker with high clinical relevance in the area of predicting disease prognosis, real-time monitoring of tumor status, and identifying therapeutic targets for personalized medicine[126]. However, CTCs are extremely rare with a frequency of only 1-10 cells in one mL of peripheral blood, which consists of billions of leukocytes and erythrocytes. So far, numerous *ex-vivo* CTC capture devices have been developed for improving the sensitivity and specificity in isolation. However, CTC isolation using these technologies mostly relies on small blood volumes and cannot detect sufficient numbers of CTCs, especially in early staged cancer, which restricts the clinical utility of CTCs as a potential biomarker. Limited sample volume also results in statistical variability associated with rare event detection[127]. Moreover, the stem-like

properties and inherent heterogeneity of CTCs adds complications to the scheme, undermining the reliability and precision of this rare cell analysis.

To increase the likelihood of CTC isolation, alternative sites including the tumor draining vessels have been considered for blood sampling. However, the accessibility to these sources is limited according to the location of the tumor and oftentimes requires intraoperative collection during surgical tumor resection, which may not be applicable for most patients. Furthermore, despite the considerable amount of CTCs detected in samples from the tumor draining vessels, it is not sure whether all of these cells may pose any clinical value. Most cancer cells rapidly undergo apoptosis after being shed from primary tumor, leaving only few to survive in circulation. In order to harvest sufficient number of CTCs in peripheral blood, catheter based CTC enrichment methods have been developed for *in-vivo* CTC isolation. Utilizing leukapheresis, it has been demonstrated that CTCs can be collected together with mononuclear cells using extracorporeal density based separation from several liters of patient blood[128,129]. Although this enabled substantial increase in detecting CTCs, the enrichment process was rather nonspecific. The leukapheresis product was mainly consisted of concentrated peripheral blood mononuclear cells, which required an additional high throughput screening step for CTC identification. Another approach used a stainless steel medical wire covered with gold and a hydrogel layer covalently coupled with antibodies against epithelial cellular adhesion molecule (EpCAM) protein[130,131]. This wire was inserted into the cubital vein for 30 minutes through a 20 gauge peripheral venous catheter. However, physiologic variations between patients affecting blood flow and affinity makes it difficult to standardize quantitative interpretation of CTCs by time of insertion.

To address the shortcomings of current approaches, in this chapter, we present a micro-apheresis CTC isolation system and demonstrate its clinical utility for *in-vivo* CTC capture. The system consists of four major parts: a microcontroller, a CTC capture module, a peristaltic pump for continuous blood sampling from the peripheral vein through a dual-lumen catheter, and a heparin injector to prevent blood clot formation during operation. Whole blood is routed at a defined flow rate through the CTC capture module for several hours, allowing the screening of large blood volumes for improved probability of detection and statistical accuracy of the analysis. The compact design offers portability and wearability, which can decrease the patient's burden during operation. While any chip-based CTC isolation platform would be compatible with the system, for our proof of concept, we designed and tested a high throughput ^{HB}GO-CTC Chip to be used as a CTC capture module. The ^{HB}GO-CTC chip incorporates functional graphene oxide (GO) nanosheets as a conjugation material to present antibodies against EpCAM antigen on a gold plated substrate, which is assembled with a vortex generating fluidic channel optimized for enhanced cell-surface interactions. Finally, we validate the system for in-vivo CTC isolation in canine models.

5.2 Material and Methods

5.2.1 Fabrication of System Manifold and ^{HB}GO-CTC Chip

The design of the system manifold was created by CAD software (Solidworks) and fabricated using a high-resolution 3D printer (Projet 3500 Max). An acrylic based resin, M3 crystal, was used for the printing process for its mechanical integrity and biocompatibility. Each component including the pump, heparin injector, power source, and micro controller were placed

in the designated compartment and enclosed. The production of the ^{HB}GO-CTC Chip involved two separate processes. First, to fabricate the chip substrate, Cr and Au was evaporated onto a 4 inch silicon dioxide wafer and patterned. The wafer was then diced into individual pieces. Next, to fabricate the PDMS (polydimethylsiloxane) structure, a silicon master mold was created by standard photolithography. Negative photoresist (SU-8 2050, MicroChem) was patterned on a 4 inch bare silicon wafer using two separate masks: one for the main fluidic channel (40 μm height) and the other for the herringbone grooves (60 μm). The height of each layer was measured after each process with a surface profilometer (Veeco Dektak 6M). PDMS pre-polymer mixed with cross linkers at a 10:1 weight ratio was poured onto the mold, degassed, and baked in an oven at 65°C for 24 hours. The cured PDMS structure was then carefully peeled off and cut. At last, two through holes were punched at both ends of the channel to feed and connect tubing.

5.2.2 ^{HB}GO-CTC Chip Assembly and Surface Functionalization

To chemically modify the chip surface, tetrabutyl ammonium hydroxide intercalated GO nano sheets grafted with phospholipid-polyethylene glycol-amine were prepared and assembled on the gold patterned silicone dioxide substrate as described previously[64]. The substrates and PDMS replicas were subjected to oxygen plasma treatment and bonded to form the final device. N-γ-maleimidobutyryl-oxysuccinimide ester (GMBS) was flowed through the chip using a syringe pump (Harvard apparatus) and incubated for 30 min. The chip was then flushed with 70% ethanol to pre-sterilize the inner chamber wall. Subsequently, neutravidin and biotinylated anti-EpCAM antibody was introduced followed by 3% bovine serum albumin (BSA) to block the remaining binding surface.

5.2.3 Sterilization Process

To prevent any microbial contamination, all disposable units with in direct contact to the blood including the tubes, lure connectors, and syringes were sterilized using heat or ethylene oxide gas sterilization method and packaged separately. For the CTC capture chip, the substrate was exposed to UV and the PDMS was autoclaved before assembly. All surface modification steps were performed in a germ poor environment. Each reagent was sterilized and tested for endotoxin level using limulus-amebocyte-lysate (LAL) gel clot assay (0.5 EU/mL sensitivity, Lonza) before use. After complete functionalization, the fluid within a subset of chip was sampled, plated on sheep blood agar, and cultured for 2 weeks to observe any presence of bacterial growth.

5.2.4 Cell Culture and Labeling

Human epithelial breast cancer cell line MCF-7 was purchased from the American Type Culture Collection (ATCC, LGC Standards). MCF-7 cells were cultured at 37°C with 5% CO_2 and maintained by regular passage in complete media consisting of Dulbecco's Modified Eagle's Media (DMEM) with 10% fetal bovine serum (FBS) and 1% penicillin-streptomycin solution (GIBCO®, Life Technology). When cells reached a confluency of 70-80%, they were collected and fluorescently labeled with green cell tracker dye (Invitrogen, CellTracker Green CMFDA, C7025) for cell capture experiments.

5.2.5 Cell Viability Assay

To measure cell viability after processing samples through the ^{HB}GO CTC-Chip, a live/dead viability/cytotoxicity assay kit (GIBCO®, Life Technology) was used. The chip was washed with 1× PBS (phosphate bufferd saline, GIBCO®, Life Technology) after capturing the cells. Subsequently, a live/dead reagent consisting of calcein AM and ethidium homodimer-1 was prepared according to the manufacturer's instruction and applied. Following 30 min incubation, cells were imaged and manually counted under a fluorescent microscope for quantification.

5.2.6 Human Blood Specimen Collection

Whole blood was drawn from healthy volunteers after obtaining informed consent under an Institutional Review Board (IRB)-approved protocol. All samples were and collected into an EDTA tube and processed within 4 hours.

5.2.7 Immunofluorescent Staining

Non-labeled cells spiked into blood or injected into canine models were fixed with 4% paraformaldehyde (PFA) on chip after capture. Before staining, the cells were permeabilized with 0.1% Triton-X followed by blocking with a blocking buffer containing 2% normal goat serum and 3% BSA. A cocktail of primary antibodies including anti-pan cytokeratin and anti-human/canine CD45 were diluted in 1% BSA and flowed through the chip. After a quick wash, secondary antibodies conjugated with Alexa Fluor 546 and 488 (Invitrogen) were prepared in 1%

BSA and applied for probing. The cell neclei were stained with 4',6-diamidino-2-phenylindole (DAPI, Invitrogen) as the final step before microscopic imaging.

5.3 System Design

The overall system configuration and strategy for CTC isolation is depicted in Figure 5.1. Each functional component is integrated into a compact 3D printed manifold to permit portability and controlled through a custom built mobile application via Bluetooth communication. For vascular access, a dual lumen catheter is introduced to sample and route the blood flow through the system with minimum inoculation. Each end of the catheter is connected to a silicone tube with luer lock adaptors that threads into a peristaltic pump and CTC capture module forming a closed loop structure. Whole blood is infused into the system by the peristaltic pump with a pre-programmed flow rate and total volume. In between, a flow rate sensor is implemented to monitor and maintain a constant flow through a feedback control. To prevent blood clot formation during operation, heparin is continuously infused through an injection pump. Every unit, in direct contact to the blood during sampling and re-transfusion, are sterilized and individually inspected before use and disposed afterwards.

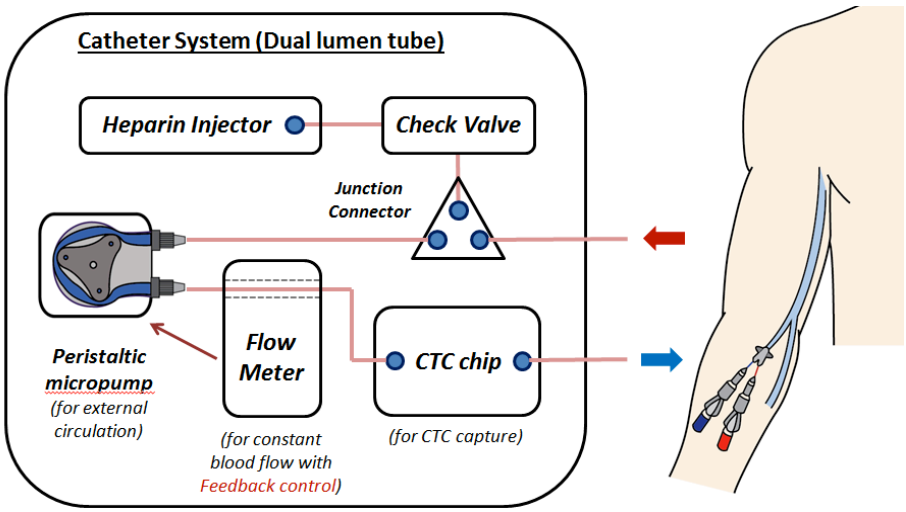

Figure 5.1 Proposed integrated catheter system for whole blood sampling and CTC isolation

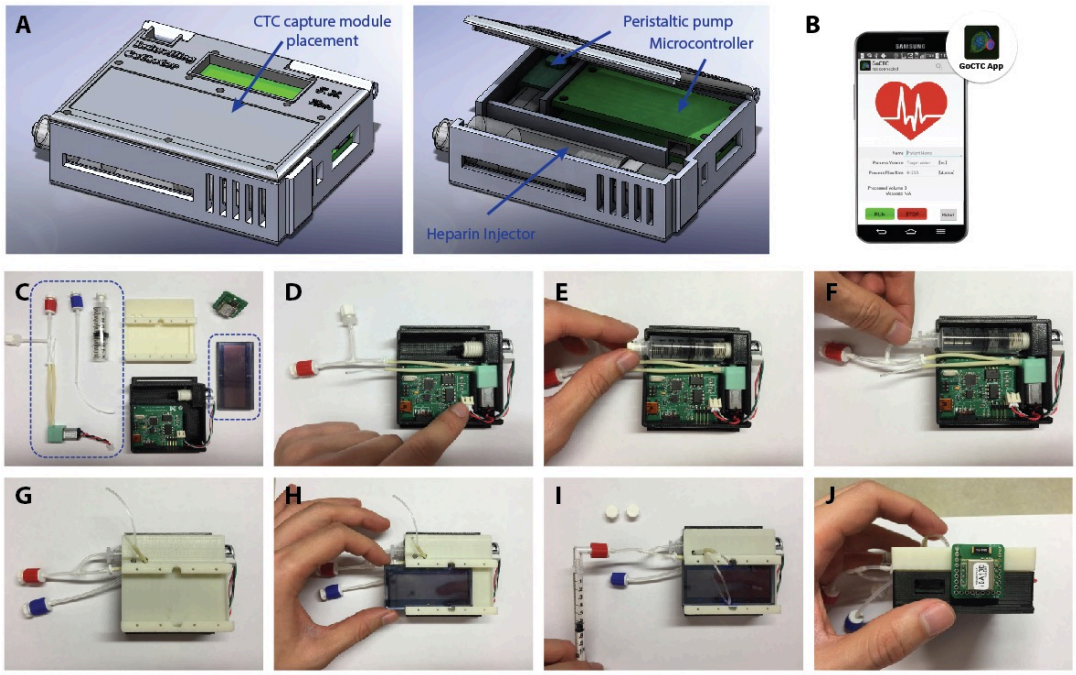

Figure 5.2 Schematic of the integrated catheter system and its operation procedures
(A) Schematic of the system without the CTC capture module. (B) Wireless controller and custom application. (C-J) System operation procedure; connect peristaltic pump with disposable tubing unit, connect syringe filled with heparin, place system cover and mount CTC capture module, prime system and connect to dual lumen catheter (not shown), and attach Bluetooth receiver to start system.

5.4 Design of ^{HB}GO CTC-Chip

The ^{HB}GO-CTC Chip consists of a 24.5 × 60 mm silicon dioxide substrate with patterned gold thin film layer bonded to a polydimethylsiloxane (PDMS) structure containing four bifurcating microchannels with herringbone grooves embedded on their top surface. Functional GO nano sheets are assembled onto the gold layer presenting high-density anti-EpCAM antibodies on the substrate surface through chemical cross-linkers. The geometry of the herringbone structure has been determined based upon previous designs used for chaotic mixing at low *Re* number (laminar flow). However, unlike early devices where the interaction mainly takes place near the grooves, the geometry of the herringbone structure has been modified to maximize the contact frequency of cells to the substrate where the antibodies are tethered.

Twenty-four chevrons, a set of twelve staggered asymmetrically, was defined as a single mixing unit and periodically shifted along the channel axis to place each vertex points with a spacing of 25 μm. The distribution of these points where a vertical drag force is induced by adjacent micro vortexes increased the chance for cells to be directed toward the antibody coated substrate. The dimension of the groove height, width, and pitch was also adjusted to decrease the hydraulic resistance past that of the main fluidic channel. This unbalanced resistance between the channel and grooves increased the overall fluidic circulation by deflecting a significant portion of fluid and cells into the herringbone structure. Cell immersed and guided through the herringbone moved in a zigzag trajectory until captured which increased its traveling time and distance within the chip. The final dimension of the PDMS structure was as followed: overall height of the main fluidic channel was 40 μm, with a groove height set to 60 μm; the groove pitch and width was 200 and 160 μm respectively and the angle between the chevrons was 45°.

5.5 Evaluation of ^{HB}GO-CTC Chip by Capture of Cancer Cell Lines

To validate the performance of the ^{HB}GO-CTC Chip for CTC capture at high flow rates, a flat chamber GO-CTC Chip previously reported was used for comparison (Figure 5.3). Human breast cancer cell-line, MCF-7 cells were labeled with a fluorescent cell-tracker dye and spiked into 5 mL of PBS buffer solution with a concentration of 50-200 cells/mL. Both cells captured on-chip and non-captured cells collected into a waste well were counted after processing the samples to calculate the capture efficiency through mass-balance. As predicted, at a flow rate of 1 mL/hr (≈ 16.67 μL/min), where most affinity based microfluidic devices operate, both chips showed high capture efficiency with a mean yield above 90% (data not shown). However, with an increasing flow rate, the average cell capture efficiency for the GO-CTC Chip dramatically dropped below 70% at 50 and 100 μL/min, and further decreased below 50% at 200 μL/min and above. In contrast, the ^{HB}GO-CTC Chip maintained a target yield of > 80% up to 200 μL/min with no significant decrease in overall capture efficiency indicating the effect of the herringbone mixer for improved cell surface interaction.

The spatial distribution of the cells captured on the chip surface was also analyzed along the channel by dividing the chip surface into ten sections. At a flow rate of 50 μL/min, a wide spread distribution was observed in the GO-CTC Chip, whereas most cells were immobilized near the inlet of the ^{HB}GO-CTC Chip. More than 80% of the cells were captured within the first half of the device, suggesting its capability to isolate cells in higher throughput. The location of these cells became more scattered across the chip at higher flow rates reaching its maximum capacity to achieve a mean yield of > 80% at 200 μL/min.

In addition, cell viability was assessed at different flow rates to determine the effect of shear force induced by increasing flow rates during the isolation process. This was one of the

critical readouts as the viability could adversely affect further downstream analysis performed on the immobilized cells. Up to a flow rate of 200 µL/min, > 90% of cells were found to be viable with no significant reduction compared to the viability at lower flow rates. Moreover, majority of cell aggregates spiked into buffer to mimic CTC clusters preserved their shape and were intact upon isolation. However, at 300 µL/min, the cell viability significantly decreased (< 70%) and cell aggregates began to dissociate being observed mostly in single cells due to high shear stress.

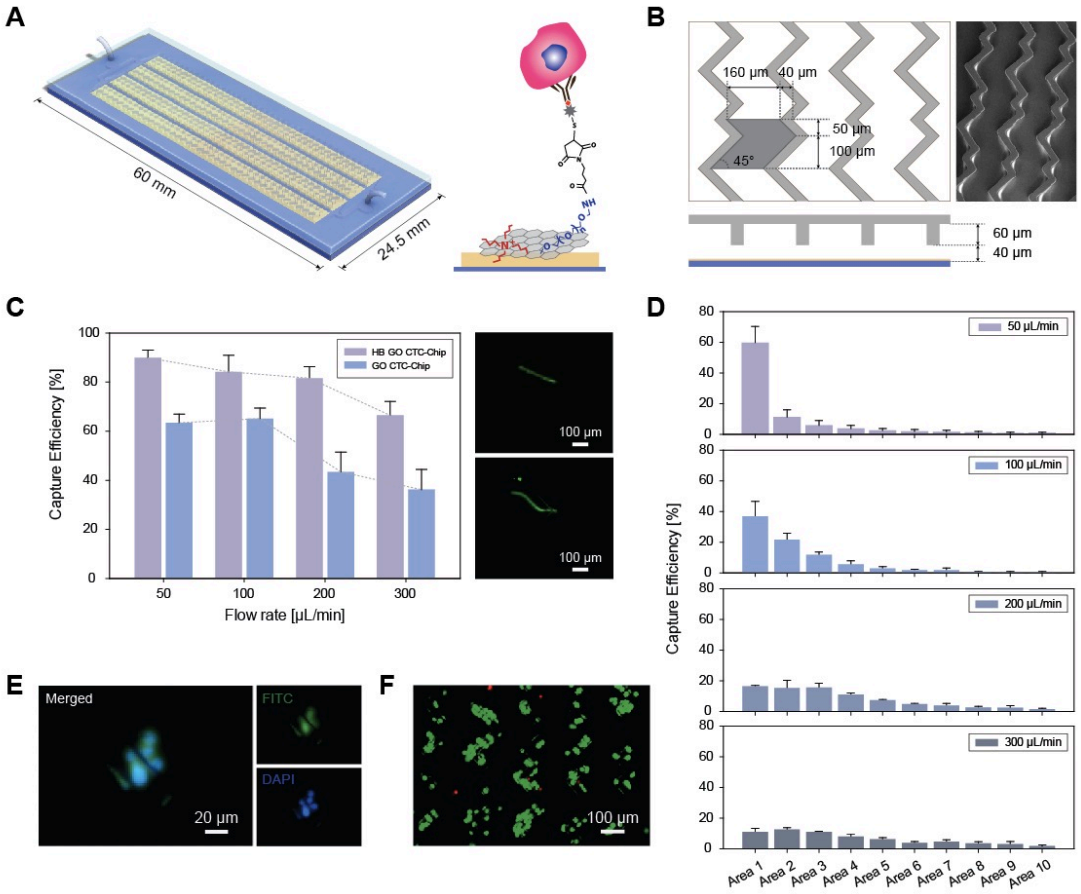

Figure 5.3 Characterization of the ^{HB}GO-CTC Chip
a Schematic of the chip. b, SEM image and micrograph image illustrating the structure of the herringbone grooves. c, Comparison of the CTC capture efficiency using the GO-CTC chip and ^{HB}GO-CTC Chip. Time lapse fluorescent image showing the trajectory of cell with in the two chips. D, Spatial distribution of the immobilized CTC captured on the chip surface. e, Cluster of CTC captured on the chip. f, live dead assay after sample processed through the chip.

5.6 In-vivo Study Design in Canine Model (Future work)

A single young adult male Walker hound will be purchased from a commercial vendor and housed individually in an AALAC-approved facility with standard day/light, watering and feeding schedules. Baseline hematology, clinical chemistry, urinalysis and coagulation profile will be obtained. All studies will be performed under an approved IACUC protocol at Colorado State University.

A series of preclinical studies to establish proof of principal that the device can be worn by a living vertebrate animal (in this case a dog), and to determine if there is an optimal time that establishes both safety and efficacy in capturing circulating tumor cells will be conducted. These studies will be performed in sequence, using a series of canine models. Our first experiments will involve in vivo injection of cultured MDCK canine epithelial cancer cells. Once we have established the success of safe cannulization and handling of the device, as well as successful harvesting of MDCK cells in the device from the circulation, we will embark on a series of studies in dogs bearing spontaneous epithelial cancers.

In the first experiment, 3×10^7 heparinized MDCK cells, suspended in 5 mL sterile pyrogen free NaCl, will be injected intravenously via the cephalic vein. 10 minutes, 30 minutes, and 1, 2, 4, 8 and 24 hours following injection, peripheral blood will be collected into CellSave tubes and evaluated for capture efficacy *in vitro*. Following demonstration of appropriate capture *ex vivo*, the dog will be sedated with butorphanol and dexmedetomidine, the ventral cervical region clipped and aseptically scrubbed and an 8-French double-lumen catheter (Arrow/Teleflex, Morrisville, NC) will be placed in the jugular vein. Extension sets will be attached to both catheters and heparin-locked. The flow-through tumor cell collection device (CTC capture module) will be attached and primed. Ten minutes following injection, the device will be

activated and blood allowed to circulate through the device for up to 120 minutes (circulation time will depend on the results of the *ex vivo* experiment). Following completion of the collection time, the central catheter will be removed and blood collected for coagulation testing. Sedation will be reversed and the dog will be monitored continuously until completely recovered. The following day and 7 days later, blood and urine will be submitted for hematology, clinical chemistry, urinalysis, and coagulation profile.

The dog will undergo daily examination, to include temperature, pulse, respiration, monitoring of food and water intake, and examination of the catheter site. After 1 week, the dog will be off-protocol and eligible for adoption or transfer to other protocols as appropriate. We anticipate no long-term adverse effects from the procedure, as MDCK cells should not be tumorigenic in an allogeneic, Immunocompetent host – they should be eliminated in the same way that any other tissue type-unmatched cells or organs would following transplant.

CHAPTER 6

6 Conclusion

6.1 Limitations and Future Directions

The study of circulating tumor cells (CTC) has enormously improved our understanding of clinical cancer biology and the steps involved in metastasis. Of the efforts, the development of various microfluidic technologies has enabled the realization of sensitive isolation and detailed characterization of CTCs. The platforms introduced in this report show improvement over existing microfluidic technologies with regards to sensitivity, specificity, and throughput of CTC isolation. However, each platform also possesses limitations and opportunities to improve. In this section we focus on these opportunities as well as current challenges that should be addressed to ultimately implement these tools into routine clinical care.

6.1.1 What are the best biological or physical properties to use to isolate CTCs?

CTC enrichment strategies utilize the unique properties of CTCs that differentiate them from normal hematopoietic cells. Methods to isolate CTCs can be broadly categorized as label dependent, using cell specific protein expression (biological properties), or label independent, using size, deformability, density, or electric charge differences (physical properties).

The GO-CTC Chip and the ^{HB}GO-CTC Chip (Chapter 2, 3, 5) are affinity-based approaches targeting the membrane protein, EpCAM, expressed in CTCs for enrichment. The nano material mediated immunological capture procedure offers sensitivity to isolate even CTCs with low level of EpCAM expression. However, due to the strong ionic bonding between EpCAM antigens on the cell surface of CTCs and the antibodies, the release process from the chip after capture has been extremely challenging or requires rigorous steps which tends to significantly reduce the viability of the cells. Although downstream applications including transcriptional profiling of these cell population is feasible (Chapter 3), the confounding signals from the contaminating leukocytes complicate the data analysis. This is mainly due to the fact that many transcripts highly expressed in tumor originating cells are also expressed at low levels in normal blood cells[12]. In addition, bulk cell analysis makes it impractical to frame and examine the heterogeneous characteristics of individual CTCs. To overcome these limitations, a functionality to gently release the immobilized cells needs to be incorporated into the platform. So far, several mechanisms to enable CTC capture and release has been proposed including the GO embedded thermal sensitive polymer chip developed in our group[88]. Despite many approaches, these platforms either exhibit low yield in capture and detachment of viable CTCs or

require excessive lab equipment with complicated material handling which must be addressed in future studies.

Another limitation of the presented GO Chips is the dependence on an EpCAM based CTC capture approach. Emerging evidence suggests that CTCs are highly heterogeneous and a subset of CTCs have been identified with reduced or non-detectable expression of epithelial markers. These cells may represent carcinoma cells undergoing EMT or alternatively, cancer stem cells that have not yet shown epithelial differentiation. This suggests that the use of single antibody fails to recognize all subtypes of CTCs, which may lead to an underestimation of these subpopulations. Recent studies have demonstrated that not only EpCAM positive CTCs but also CTCs negative for EpCAM expression isolated from breast cancer patients were highly enriched for metastasis initiating capability when injected into the tail vein of immune compromised mice, forming lung and brain tumor metastasis[82,132]. Thus, to avoid these incomplete findings, there is a need for a broad-spectrum enrichment method based on the use of tumor specific antibody cocktails for cell surface epithelial and mesenchymal markers. Since the conjugation chemistry of the GO platforms allows any biotinylated antibodies to be used for surface functionalization, in future studies we plan to use a combination of antibodies against various markers that cover the complex heterogeneity of CTCs.

A different way to enrich CTCs from blood is to use their physical properties. Tumor cells have been known to be larger in size and less deformable than hematopoietic cells. The cascaded spiral microfluidic chip (Chapter 4) is a two-step CTC isolation platform utilizing the size dependent differential inertial focusing effect to improve purity upon CTC collection. The chip is designed to separate cells with a cutoff diameter of 17 to 18 μm. Since the sorting procedure is label free and done in a continuous manner, unlike the affinity-based approach, the

device is able to isolate both EpCAM positive or negative cells and produces and effluent that is amenable to any type of downstream analysis. However, CTCs of various size have been identified, some being less than 4 μm in diameter[61], which are likely to be unfocused and filtered out. In addition, all circulating cells isolated by this size selection method may not necessarily be tumor derived. They may represent normal blood vessel or stromal cells, circulating mesenchymal cells or stem cells, or other host cells that normally exist in rare quantities in circulation[133]. Also, the diameter of monocytes, consisting an approximate of 5% of WBCs, can range from 15-30 μm. This size overlap compromises the specificity of the CTC isolation process resulting in an impure CTC collection, therefore requiring further purification steps.

While the inertial chips offer a high sample processing rate, a preprocessing step is required due to the large number of RBC counts in blood, which tends to interfere with the focusing streaks. These steps include RBC lysis, density gradient separation, or a significant dilution of the original whole blood product. As RBC lysis buffers may potentially affect the viability of CTCs, which are relatively fragile, we have incorporated a dextran sedimentation method with 5x dilution using PBS to deplete RBCs before processing. However, this became the rate-limiting factor of the entire protocol comprising a one-hour incubation and multiple manual pipetting steps. Therefore, future work will involve development of a RBC presorting chip employing similar concepts of inertial focusing effect to increase the process throughput.

So far, no single methodology is capable of enriching all types of CTCs with sufficient purity for subsequent analysis. Recently, as an alternative approach, negative selection in which blood samples are depleted of known leukocytes using antibodies against CD45 have been proposed to avoid any bias and loss of CTCs with high phenotypic plasticity[134,135]. However, not all CD45 negative cells in blood are tumor cells and the technology struggles with purity from

blood cell contaminations. The debate over which isolation strategies best reveal the clinical utility of CTCs seems to be meaningless at this point, since it is not yet clear which CTC subtypes are clinically meaningful. Thus along with the development of advanced CTC enrichment protocols, there is a necessity to implement microfluidic based assays that can interrogate certain functional characteristics of CTCs such as tumor initiating capability.

6.1.2 How do we define CTCs?

The major issue in detecting CTCs is the lack of reliable immunochemical markers. An ideal CTC marker would be expressed on all CTCs but not on autochthonous blood cells such as leukocytes, endothelial cells, hematopoietic stem cells, and mesenchymal stem cells. In addition, the expression should not be repressed during invasion and circulation. Currently, epithelial markers such as EpCAM and members of cytokeratin family (CK8, CK18, CK19) have become the gold standard for the detection of CTCs in carcinoma patients. They have been frequently used since these markers are normally expressed in the epithelia or epithelial tumors but are absent on mesenchymal leukocytes and rarely present in blood samples from healthy individuals. However, circulating epithelial cells have been identified in patients with benign colon disease raising concerns with the current detection methods with regards to false positive findings[136]. More recently, cytokeratin negative or EpCAM negative CTCs have been identified, and CTC enumeration analysis using these markers may cause false negative results. This was also apparently observed in our multi-marker study (Chapter 3) from CTCs isolated from metastatic breast cancer patients. To overcome theses limitations, more tumor tissue specific markers should be studied and validated for their clinical value accompanied by the establishment for a standardized optimal cutoff for future CTC enumeration. To this end, our future direction will

involve selecting and examining various tissue markers to test their expression by CTCs and perform correlation studies with patient status. Furthermore, we plan to establish multi channel staining protocols, which currently have been limited to 4 channels, to facilitate our analysis.

6.1.3 How many CTCs are sufficient for clinical assessments?

To date, due to the difficulty of isolating and characterizing CTCs, especially from early cancer patients, only a relatively small number of CTCs out of the entire patient's pool of CTCs has been adequately characterized. Their paucity as well as the plasticity that posits extreme amount of heterogeneity under various selection pressures during circulation or therapeutic treatments has hampered our understanding of their full clinical characteristics. It is not clear how many CTCs is sufficient to make any clinical decisions based on their analysis to account for their heterogeneity and statistical variations. To resolve this issue, techniques capable of isolating CTC in sufficient number are required. Many efforts have been made to expand the number of CTCs after enrichment through sophisticated CTC culture techniques[137-139] and transplantation into xenograft assays[82,140]. However, these assays still require high CTC yield with an order of magnitude of 100s of CTCs/mL, which have so far only been achieved in highly aggressive tumor patients. Moreover, despite potential use for therapeutic testing, *in-vivo* xenograft models may not recapitulate tumor-host interactions that may play role in drug resistance. The catheter based *in-vivo* CTC isolation system (Chapter 5) shows advantages over previous *ex-vivo* CTC enrichment platforms in that it allows direct blood sampling from the patient vein and enables analysis over large blood volumes. The continuous procedure, which re-transfuses the remaining blood products after processing, permits the system to be operated for a long period of time harvesting more CTCs potentially from even early stage cancers without

severe burden on the patient. These CTCs can then be used for multiple characterization steps such as real time drug testing which can provide information about the therapeutic efficacy for future treatment decisions. However, there are a couple of drawbacks and issues that need to be resolved. Compared to recent catheter based CTC collection systems, the overall throughput is limited and must be improved. The operable flow rate of the CTC module needs to be designed to fit flow rate nears the ml/min scale to screen a total blood volume of at least 100s of mL in a few hours. Furthermore, there is a need to reduce the size of the dual lumen catheter to be placed in human peripheral subjects. In order to circumvent these issues, a high throughput CTC chip module should be developed with custom designed catheters suitable for system integration.

6.2 Conclusion

The CTC enrichment platforms introduced in this report utilize various strategies to improve the isolation process, offering versatility for detailed CTC characterization. Although the adoption of these tools into clinical practice will necessitate rigorous demonstration of their clinical validity and utility, the use of microfluidic based CTC assays in research settings will broaden our understanding of basic cancer biology and improve personalized targeted treatment for cancer patients.

BIBLIOGRAPHY

1. Mehlen, P. & Puisieux, A. Metastasis: a question of life or death. *Nature Reviews Cancer* **6,** 449–458 (2006).
2. Krebs, M. G. *et al.* Molecular analysis of circulating tumour cells —biology and biomarkers. *Nature Publishing Group* **11,** 129–144 (2014).
3. Pantel, K. & Speicher, M. R. The biology of circulating tumor cells. *Oncogene* **35,** 1216–1224 (2016).
4. Vanharanta, S. & Massagué, J. Origins of metastatic traits. *Cancer Cell* **24,** 410–421 (2013).
5. Haber, D. A. & Velculescu, V. E. Blood-based analyses of cancer: circulating tumor cells and circulating tumor DNA. *Cancer Discov* **4,** 650–661 (2014).
6. Pantel, K. & Alix-Panabières, C. Real-time liquid biopsy in cancer patients: fact or fiction? *Cancer Research* **73,** 6384–6388 (2013).
7. Cristofanilli, M. *et al.* Circulating tumor cells, disease progression, and survival in metastatic breast cancer. *N Engl J Med* **351,** 781–791 (2004).
8. Bidard, F.-C. *et al.* Clinical application of circulating tumor cells in breast cancer: overview of the current interventional trials. *Cancer Metastasis Rev* **32,** 179–188 (2012).
9. He, W., Wang, H., Hartmann, L. C., Cheng, J.-X. & Low, P. S. In vivo quantitation of rare circulating tumor cells by multiphoton intravital flow cytometry. *Proc Natl Acad Sci USA* **104,** 11760–11765 (2007).
10. Klein, C. A. Parallel progression of primary tumours and metastases. *Nature Reviews Cancer* **9,** 302–312 (2009).
11. Hüsemann, Y. *et al.* Systemic Spread Is an Early Step in Breast Cancer. *Cancer Cell* **13,** 58–68 (2008).
12. Pantel, K., Brakenhoff, R. H. & Brandt, B. Detection, clinical relevance and specific biological properties of disseminating tumour cells. *Nature Reviews Cancer* **8,** 329–340 (2008).
13. Hayes, D. F. *et al.* Circulating tumor cells at each follow-up time point during therapy of metastatic breast cancer patients predict progression-free and overall survival. *Clin. Cancer Res.* **12,** 4218–4224 (2006).
14. Maheswaran, S. *et al.* Detection of mutations in EGFR in circulating lung-cancer cells. *N Engl J Med* **359,** 366–377 (2008).
15. Alix-Panabières, C. & Pantel, K. Technologies for detection of circulating tumor cells: facts and vision. *Lab Chip* **14,** 57–62 (2013).
16. Willipinski-Stapelfeldt, B. *et al.* Changes in cytoskeletal protein composition indicative of an epithelial-mesenchymal transition in human micrometastatic and primary breast carcinoma cells. *Clin. Cancer Res.* **11,** 8006–8014 (2005).
17. Bednarz-Knoll, N., Alix-Panabières, C. & Pantel, K. Plasticity of disseminating cancer cells in patients with epithelial malignancies. *Cancer Metastasis Rev* **31,** 673–687 (2012).

18. Nagrath, S. *et al.* Isolation of rare circulating tumour cells in cancer patients by microchip technology. *Nature Publishing Group* **450,** 1235–1239 (2007).
19. Lin, H. K. *et al.* Portable Filter-Based Microdevice for Detection and Characterization of Circulating Tumor Cells. *Clin. Cancer Res.* **16,** 5011–5018 (2010).
20. Dobrovolskaia, M. A. & McNeil, S. E. Immunological properties of engineered nanomaterials. *Nat Nanotechnol* **2,** 469–478 (2007).
21. Xia, X.-R., Monteiro-Riviere, N. A. & Riviere, J. E. An index for characterization of nanomaterials in biological systems. 1–5 (2010). doi:10.1038/nnano.2010.164
22. Wang, S. *et al.* Three-Dimensional Nanostructured Substrates toward Efficient Capture of Circulating Tumor Cells. *Angew. Chem. Int. Ed.* **48,** 8970–8973 (2009).
23. Lee, S.-K. *et al.* Nanowire Substrate-Based Laser Scanning Cytometry for Quantitation of Circulating Tumor Cells. *Nano Lett.* **12,** 2697–2704 (2012).
24. Zhang, N. *et al.* Electrospun TiO2 Nanofiber-Based Cell Capture Assay for Detecting Circulating Tumor Cells from Colorectal and Gastric Cancer Patients. *Adv. Mater.* **24,** 2756–2760 (2012).
25. Liu, Z., Robinson, J. T., Sun, X. & Dai, H. PEGylated Nanographene Oxide for Delivery of Water-Insoluble Cancer Drugs. *J. Am. Chem. Soc.* **130,** 10876–10877 (2008).
26. Mohanty, N. & Berry, V. Graphene-Based Single-Bacterium Resolution Biodevice and DNA Transistor: Interfacing Graphene Derivatives with Nanoscale and Microscale Biocomponents. *Nano Lett.* **8,** 4469–4476 (2008).
27. Ramanathan, T. *et al.* Functionalized graphene sheets for polymer nanocomposites. *Nat Nanotechnol* **3,** 327–331 (2008).
28. Dreyer, D. R., Park, S., Bielawski, C. W. & Ruoff, R. S. The chemistry of graphene oxide. *Chem. Soc. Rev.* **39,** 228–240 (2010).
29. Sun, X. *et al.* Nano-graphene oxide for cellular imaging and drug delivery. *Nano Res.* **1,** 203–212 (2008).
30. Eda, G., Fanchini, G. & Chhowalla, M. Large-area ultrathin films of reduced graphene oxide as a transparent and flexible electronic material. *Nat Nanotechnol* **3,** 270–274 (2008).
31. Li, X. *et al.* Highly conducting graphene sheets and Langmuir–Blodgett films. *Nat Nanotechnol* **3,** 538–542 (2008).
32. Wang, H., Wang, X., Li, X. & Dai, H. Chemical self-assembly of graphene sheets. *Nano Res.* **2,** 336–342 (2009).
33. Sieuwerts, A. M. *et al.* Anti-epithelial cell adhesion molecule antibodies and the detection of circulating normal-like breast tumor cells. *J. Natl. Cancer Inst.* **101,** 61–66 (2009).
34. Salic, A. & Mitchison, T. J. A chemical method for fast and sensitive detection of DNA synthesis in vivo. *PNAS* **105,** 2415–2420 (2008).
35. Lustberg, M., Jatana, K. R., Zborowski, M. & Chalmers, J. J. in *Minimal Residual Disease and Circulating Tumor Cells in Breast Cancer* **195,** 97–110 (Springer Berlin Heidelberg, 2012).
36. Stott, S. L., Hsu, C. H., Tsukrov, D. I. & Yu, M. Isolation of circulating tumor cells using a microvortex-generating herringbone-chip. in (2010). doi:10.1073/pnas.1012539107/-/DCSupplemental
37. Mego, M. *et al.* Characterization of metastatic breast cancer patients with nondetectable circulating tumor cells. *Int. J. Cancer* **129,** 417–423 (2011).

38. Alix-Panabières, C., Schwarzenbach, H. & Pantel, K. Circulating Tumor Cells and Circulating Tumor DNA. *Annu. Rev. Med.* **63,** 199–215 (2012).
39. Ozkumur, E. *et al.* Inertial focusing for tumor antigen-dependent and -independent sorting of rare circulating tumor cells. *Sci Transl Med* **5,** 179ra47–179ra47 (2013).
40. Matthew G Krebs MBChB, P. *et al.* Analysis of Circulating Tumor Cells in Patients with Non-small Cell Lung Cancer Using Epithelial Marker-Dependent and -Independent Approaches. *JTO Acquisition* **7,** 306–315 (2012).
41. Curigliano, G. *et al.* Should liver metastases of breast cancer be biopsied to improve treatment choice? *Ann. Oncol.* **22,** 2227–2233 (2011).
42. Amir, E. *et al.* Tissue confirmation of disease recurrence in breast cancer patients: Pooled analysis of multi-centre, multi-disciplinary prospective studies. *Cancer Treatment Reviews* **38,** 708–714 (2012).
43. Fehm, T. *et al.* HER2 status of circulating tumor cells in patients with metastatic breast cancer: a prospective, multicenter trial. *Breast Cancer Res Treat* **124,** 403–412 (2010).
44. Riethdorf, S. *et al.* Detection and HER2 Expression of Circulating Tumor Cells: Prospective Monitoring in Breast Cancer Patients Treated in the Neoadjuvant GeparQuattro Trial. *Clin. Cancer Res.* **16,** 2634–2645 (2010).
45. Pestrin, M. *et al.* Final results of a multicenter phase II clinical trial evaluating the activity of single-agent lapatinib in patients with HER2-negative metastatic breast cancer and HER2-positive circulating tumor cells. A proof-of-concept study. *Breast Cancer Res Treat* **134,** 283–289 (2012).
46. Benson, J. R. & Jatoi, I. The global breast cancer burden. *Future Oncol* **8,** 697–702 (2012).
47. Janni, W. J. *et al.* Pooled Analysis of the Prognostic Relevance of Circulating Tumor Cells in Primary Breast Cancer. *Clin. Cancer Res.* **22,** 2583–2593 (2016).
48. Giuliano, M. *et al.* Circulating tumor cells as prognostic and predictive markers in metastatic breast cancer patients receiving first-line systemic treatment. *Breast Cancer Res* **13,** R67 (2011).
49. Franken, B. *et al.* Circulating tumor cells, disease recurrence and survival in newly diagnosed breast cancer. *Breast Cancer Res* **14,** R133 (2012).
50. Budd, G. T. *et al.* Circulating tumor cells versus imaging--predicting overall survival in metastatic breast cancer. *Clin. Cancer Res.* **12,** 6403–6409 (2006).
51. Alix-Panabières, C. & Pantel, K. Challenges in circulating tumour cell research. *Nature Publishing Group* **14,** 623–631 (2014).
52. Powell, A. A. *et al.* Single cell profiling of circulating tumor cells: transcriptional heterogeneity and diversity from breast cancer cell lines. *PLoS ONE* **7,** e33788 (2012).
53. Aktas, B. *et al.* Comparison of the HER2, estrogen and progesterone receptor expression profile of primary tumor, metastases and circulating tumor cells in metastatic breast cancer patients. *BMC Cancer* **16,** 522 (2016).
54. Paoletti, C. *et al.* Development of circulating tumor cell-endocrine therapy index in patients with hormone receptor-positive breast cancer. *Clin. Cancer Res.* **21,** 2487–2498 (2015).
55. Liu, S. *et al.* Breast cancer stem cells transition between epithelial and mesenchymal states reflective of their normal counterparts. *Stem Cell Reports* **2,** 78–91 (2014).
56. Kalluri, R. & Weinberg, R. A. The basics of epithelial-mesenchymal transition. *J. Clin. Invest.* **119,** 1420–1428 (2009).

57. Aktas, B. *et al.* Stem cell and epithelial-mesenchymal transition markers are frequently overexpressed in circulating tumor cells of metastatic breast cancer patients. *Breast Cancer Res* **11,** R46 (2009).
58. Yu, M. *et al.* Circulating breast tumor cells exhibit dynamic changes in epithelial and mesenchymal composition. *Science* **339,** 580–584 (2013).
59. Vona, G., Sabile, A., Louha, M., Sitruk, V. & Romana, S. Isolation by size of epithelial tumor cells: a new method for the immunomorphological and molecular characterization of circulating tumor cells. *The American journal of ...* (2000). doi:10.1016/S0002-9440(10)64706-2
60. Gertler, R. *et al.* Detection of circulating tumor cells in blood using an optimized density gradient centrifugation. *Recent Results Cancer Res.* **162,** 149–155 (2003).
61. Allard, W. J. *et al.* Tumor cells circulate in the peripheral blood of all major carcinomas but not in healthy subjects or patients with nonmalignant diseases. *Clin. Cancer Res.* **10,** 6897–6904 (2004).
62. Riethdorf, S. *et al.* Detection of circulating tumor cells in peripheral blood of patients with metastatic breast cancer: a validation study of the CellSearch system. *Clin. Cancer Res.* **13,** 920–928 (2007).
63. Yoon, H. J., Kozminsky, M. & Nagrath, S. Emerging Role of Nanomaterials in Circulating Tumor Cell Isolation and Analysis. *ACS Nano* **8,** 1995–2017 (2014).
64. Yoon, H. J. *et al.* Sensitive capture of circulating tumour cells by functionalized graphene oxide nanosheets. *Nat Nanotechnol* **8,** 735–741 (2013).
65. Korkaya, H. & Wicha, M. S. HER2 and breast cancer stem cells: more than meets the eye. *Cancer Research* **73,** 3489–3493 (2013).
66. Ithimakin, S. *et al.* HER2 drives luminal breast cancer stem cells in the absence of HER2 amplification: implications for efficacy of adjuvant trastuzumab. *Cancer Research* **73,** 1635–1646 (2013).
67. Polioudaki, H. *et al.* Variable expression levels of keratin and vimentin reveal differential EMT status of circulating tumor cells and correlation with clinical characteristics and outcome of patients with metastatic breast cancer. *BMC Cancer* **15,** 399 (2015).
68. Joosse, S. A. *et al.* Changes in keratin expression during metastatic progression of breast cancer: impact on the detection of circulating tumor cells. *Clin. Cancer Res.* **18,** 993–1003 (2012).
69. Dent, R. *et al.* Triple-negative breast cancer: clinical features and patterns of recurrence. *Clin. Cancer Res.* **13,** 4429–4434 (2007).
70. MD, F. O.-C. M. B. *et al.* Clinical validity of circulating tumour cells in patients with metastatic breast cancer: a pooled analysis of individual patient data. *Lancet Oncology* **15,** 406–414 (2014).
71. Pestrin, M. *et al.* Correlation of HER2 status between primary tumors and corresponding circulating tumor cells in advanced breast cancer patients. *Breast Cancer Res Treat* **118,** 523–530 (2009).
72. Zidan, J. *et al.* Comparison of HER-2 overexpression in primary breast cancer and metastatic sites and its effect on biological targeting therapy of metastatic disease. *British Journal of Cancer* **93,** 552–556 (2005).
73. Jordan, N. V. *et al.* HER2 expression identifies dynamic functional states within circulating breast cancer cells. *Nature Publishing Group* **537,** 102–106 (2016).

74. Korkaya, H., Paulson, A., Iovino, F. & Wicha, M. S. HER2 regulates the mammary stem/progenitor cell population driving tumorigenesis and invasion. *Oncogene* **27,** 6120–6130 (2008).
75. Magnifico, A. *et al.* Tumor-initiating cells of HER2-positive carcinoma cell lines express the highest oncoprotein levels and are sensitive to trastuzumab. *Clin. Cancer Res.* **15,** 2010–2021 (2009).
76. Wülfing, P. *et al.* HER2-positive circulating tumor cells indicate poor clinical outcome in stage I to III breast cancer patients. *Clin. Cancer Res.* **12,** 1715–1720 (2006).
77. Kalluri, R. EMT: when epithelial cells decide to become mesenchymal-like cells. *J. Clin. Invest.* **119,** 1417–1419 (2009).
78. Armstrong, A. J. *et al.* Circulating tumor cells from patients with advanced prostate and breast cancer display both epithelial and mesenchymal markers. *Mol. Cancer Res.* **9,** 997–1007 (2011).
79. Kallergi, G. *et al.* Epithelial to mesenchymal transition markers expressed in circulating tumour cells of early and metastatic breast cancer patients. *Breast Cancer Res* **13,** R59 (2011).
80. Kang, Y. & Pantel, K. Tumor cell dissemination: emerging biological insights from animal models and cancer patients. *Cancer Cell* **23,** 573–581 (2013).
81. Tam, W. L. & Weinberg, R. A. The epigenetics of epithelial-mesenchymal plasticity in cancer. *Nat. Med.* **19,** 1438–1449 (2013).
82. Baccelli, I. *et al.* Identification of a population of blood circulating tumor cells from breast cancer patients that initiates metastasis in a xenograft assay. *Nat Biotechnol* **31,** 539–544 (2013).
83. Mohme, M., Riethdorf, S. & Pantel, K. Circulating and disseminated tumour cells - mechanisms of immune surveillance and escape. *Nat Rev Clin Oncol* **14,** 155–167 (2017).
84. Krajewski, S. *et al.* Reduced expression of proapoptotic gene BAX is associated with poor response rates to combination chemotherapy and shorter survival in women with metastatic breast adenocarcinoma. *Cancer Research* **55,** 4471–4478 (1995).
85. Basu, A. & Haldar, S. The relationship between BcI2, Bax and p53: consequences for cell cycle progression and cell death. *Molecular human reproduction* (1998).
86. Duda, D. G. *et al.* Malignant cells facilitate lung metastasis by bringing their own soil. *PNAS* **107,** 21677–21682 (2010).
87. Ting, D. T. *et al.* Single-cell RNA sequencing identifies extracellular matrix gene expression by pancreatic circulating tumor cells. *Cell Rep* **8,** 1905–1918 (2014).
88. Yoon, H. J., Shanker, A., Wang, Y. & Kozminsky, M. Tunable Thermal-Sensitive Polymer–Graphene Oxide Composite for Efficient Capture and Release of Viable Circulating Tumor Cells. *Advanced ...* (2016). doi:10.1002/adma.201600658
89. Reátegui, E. *et al.* Tunable nanostructured coating for the capture and selective release of viable circulating tumor cells. *Adv. Mater. Weinheim* **27,** 1593–1599 (2015).
90. Shen, Q. *et al.* Specific Capture and Release of Circulating Tumor Cells Using Aptamer-Modified Nanosubstrates. *Advanced ...* (2013). doi:10.1002/adma.201300082
91. Li, W. *et al.* Biodegradable nano-films for capture and non-invasive release of circulating tumor cells. *Biomaterials* **65,** 93–102 (2015).
92. Zheng, S. *et al.* 3D microfilter device for viable circulating tumor cell (CTC) enrichment from blood. *Biomed Microdevices* **13,** 203–213 (2011).

93. Gascoyne, P. R. C., Noshari, J., Anderson, T. J. & Becker, F. F. Isolation of rare cells from cell mixtures by dielectrophoresis. *Electrophoresis* **30,** 1388–1398 (2009).
94. Moon, H.-S. *et al.* Continuous separation of breast cancer cells from blood samples using multi-orifice flow fractionation (MOFF) and dielectrophoresis (DEP). *Lab Chip* **11,** 1118–1125 (2011).
95. Hoshino, K. *et al.* Microchip-based immunomagnetic detection of circulating tumor cells. *Lab Chip* **11,** 3449–3457 (2011).
96. Kang, J. H. *et al.* A combined micromagnetic-microfluidic device for rapid capture and culture of rare circulating tumor cells. *Lab Chip* **12,** 2175–2181 (2012).
97. Petersson, F., Aberg, L., Swärd-Nilsson, A.-M. & Laurell, T. Free flow acoustophoresis: microfluidic-based mode of particle and cell separation. *Anal. Chem.* **79,** 5117–5123 (2007).
98. Dochow, S. *et al.* Tumour cell identification by means of Raman spectroscopy in combination with optical traps and microfluidic environments. *Lab Chip* **11,** 1484–1490 (2011).
99. Wang, X. *et al.* Enhanced cell sorting and manipulation with combined optical tweezer and microfluidic chip technologies. *Lab Chip* **11,** 3656–3662 (2011).
100. Shah, A. M. *et al.* Biopolymer system for cell recovery from microfluidic cell capture devices. *Anal. Chem.* **84,** 3682–3688 (2012).
101. Chaffer, C. L. & Weinberg, R. A. A perspective on cancer cell metastasis. *Science* **331,** 1559–1564 (2011).
102. Pecot, C. V. *et al.* A novel platform for detection of CK+ and CK- CTCs. *Cancer Discov* **1,** 580–586 (2011).
103. Zhou, J., Giridhar, P. V., Kasper, S. & Papautsky, I. Modulation of aspect ratio for complete separation in an inertial microfluidic channel. *Lab Chip* **13,** 1919–1929 (2013).
104. Hou, H. W. *et al.* Isolation and retrieval of circulating tumor cells using centrifugal forces. *Sci Rep* **3,** 1259 (2013).
105. Sun, J. *et al.* Double spiral microchannel for label-free tumor cell separation and enrichment. *Lab Chip* **12,** 3952–3960 (2012).
106. Russom, A. *et al.* Differential inertial focusing of particles in curved low-aspect-ratio microchannels. *New J Phys* **11,** 75025 (2009).
107. Kuntaegowdanahalli, S. S., Bhagat, A. A. S., Kumar, G. & Papautsky, I. Inertial microfluidics for continuous particle separation in spiral microchannels. *Lab Chip* **9,** 2973–2980 (2009).
108. Di Carlo, D., Irimia, D., Tompkins, R. G. & Toner, M. Continuous inertial focusing, ordering, and separation of particles in microchannels. *PNAS* **104,** 18892–18897 (2007).
109. Di Carlo, D. Inertial microfluidics. *Lab Chip* **9,** 3038–3046 (2009).
110. Vona, G. *et al.* Isolation by Size of Epithelial Tumor Cells. *The American Journal of Pathology* **156,** 57–63 (2000).
111. Yu, M., Stott, S., Toner, M., Maheswaran, S. & Haber, D. A. Circulating tumor cells: approaches to isolation and characterization. *J. Cell Biol.* **192,** 373–382 (2011).
112. Martel, J. M. & Toner, M. Inertial focusing dynamics in spiral microchannels. *Phys Fluids (1994)* **24,** 32001 (2012).
113. Wu, L., Guan, G., Hou, H. W., Bhagat, A. A. S. & Han, J. Separation of leukocytes from blood using spiral channel with trapezoid cross-section. *Anal. Chem.* **84,** 9324–9331 (2012).

114. Martel, J. M. & Toner, M. Particle Focusing in Curved Microfluidic Channels. *Sci Rep* **3,** (2013).
115. Boyum, A. Separation of blood leucocytes, granulocytes and lymphocytes. *Tissue Antigens* **4,** 269–274 (1974).
116. Geng, Z., Ju, Y., Wang, Q., Wang, W. & Li, Z. Multi-component continuous separation chip composed of micropillar arrays in a split-level spiral channel. *RSC Advances* **3,** 14798–14806 (2013).
117. Segre, G. & Silberberg, A. Radial particle displacements in Poiseuille flow of suspensions. *Nature* **189,** 209–210 (1961).
118. Matas, J.-P., Glezer, V., Guazzelli, E. & Morris, J. F. Trains of particles in finite-Reynolds-number pipe flow. *Phys. Fluids* **16,** 4192 (2004).
119. Matas, J. P., Morris, J. F. & Guazzelli, E. Inertial migration of rigid spherical particles in Poiseuille flow. *... of Fluid Mechanics* (2004).
120. Guan, G. *et al.* Spiral microchannel with rectangular and trapezoidal cross-sections for size based particle separation. *Sci Rep* **3,** 1475 (2013).
121. Zhou, J. & Papautsky, I. Fundamentals of inertial focusing in microchannels. *Lab Chip* **13,** 1121–1132 (2013).
122. Asmolov, E. S. The inertial lift on a spherical particle in a plane Poiseuille flow at large channel Reynolds number. *Journal of Fluid Mechanics* (1999).
123. Bhagat, A. A. S., Kuntaegowdanahalli, S. S. & Papautsky, I. Continuous particle separation in spiral microchannels using Dean flows and differential migration. *Lab Chip* **8,** 1906–1914 (2008).
124. Gervais, T., El-Ali, J., Günther, A. & Jensen, K. F. Flow-induced deformation of shallow microfluidic channels. *Lab Chip* **6,** 500–507 (2006).
125. Hanahan, D. & Weinberg, R. A. Hallmarks of cancer: the next generation. *Cell* **144,** 646–674 (2011).
126. Alix-Panabières, C. & Pantel, K. Circulating tumor cells: liquid biopsy of cancer. *Clinical Chemistry* **59,** 110–118 (2013).
127. Allan, A. L. & Keeney, M. Circulating tumor cell analysis: technical and statistical considerations for application to the clinic. *J Oncol* **2010,** 426218–10 (2010).
128. Fischer, J. C., Niederacher, D. & Topp, S. A. Diagnostic leukapheresis enables reliable detection of circulating tumor cells of nonmetastatic cancer patients. in (2013). doi:10.1073/pnas.1313594110/-/DCSupplemental
129. Eifler, R. L. *et al.* Enrichment of circulating tumor cells from a large blood volume using leukapheresis and elutriation: proof of concept. *Cytometry B Clin Cytom* **80,** 100–111 (2011).
130. Saucedo-Zeni, N. *et al.* A novel method for the in vivo isolation of circulating tumor cells from peripheral blood of cancer patients using a functionalized and structured medical wire. *Int. J. Oncol.* **41,** 1241–1250 (2012).
131. Gorges, T. M. *et al.* Enumeration and Molecular Characterization of Tumor Cells in Lung Cancer Patients Using a Novel In Vivo Device for Capturing Circulating Tumor Cells. *Clin. Cancer Res.* **22,** 2197–2206 (2016).
132. Zhang, L. *et al.* The identification and characterization of breast cancer CTCs competent for brain metastasis. *Sci Transl Med* **5,** 180ra48–180ra48 (2013).
133. Kolonin, M. G., Evans, K. W., Mani, S. A. & Gomer, R. H. Alternative origins of stroma in normal organs and disease. *Stem Cell Res* **8,** 312–323 (2012).

134. Yang, L. *et al.* Optimization of an enrichment process for circulating tumor cells from the blood of head and neck cancer patients through depletion of normal cells. *Biotechnol. Bioeng.* **102,** 521–534 (2009).
135. Ramirez, J.-M. *et al.* Prognostic relevance of viable circulating tumor cells detected by EPISPOT in metastatic breast cancer patients. *Clinical Chemistry* **60,** 214–221 (2014).
136. Pantel, K. *et al.* Circulating Epithelial Cells in Patients with Benign Colon Diseases. *Clinical Chemistry* **58,** 936–940 (2012).
137. Yu, M. *et al.* Ex vivo culture of circulating breast tumor cells for individualized testing of drug susceptibility. *Science* **345,** 216–220 (2014).
138. Karthaus, W. R. *et al.* Identification of multipotent luminal progenitor cells in human prostate organoid cultures. *Cell* **159,** 163–175 (2014).
139. Gao, D. *et al.* Organoid cultures derived from patients with advanced prostate cancer. *Cell* **159,** 176–187 (2014).
140. Hodgkinson, C. L. *et al.* Tumorigenicity and genetic profiling of circulating tumor cells in small-cell lung cancer. *Nat. Med.* **20,** 897–903 (2014).